Cronfa - Swansea University Open Access Repository

_____

This is an author produced version of a paper published in :
International Journal for Numerical Methods in Engineering

Cronfa URL for this paper:

_____

Paper:

_____

Improved Hybrid Displacement Function (IHDF) element scheme for analysis of Mindlin-Reissner plate with edge effect

Yan Shang[1, 5], Song Cen[1, 3, 4, *, †], Zhi Li[1], Chen-Feng Li[2]

[1] *Department of Engineering Mechanics, School of Aerospace Engineering, Tsinghua University, Beijing 100084, China*

[2] *Zienkiewicz Centre for Computational Engineering, College of Engineering, Swansea University, Swansea SA2 8PP, UK*

[3] *High Performance Computing Center, School of Aerospace Engineering, Tsinghua University, Beijing 100084, China*

[4] *Key Laboratory of Applied Mechanics, School of Aerospace Engineering, Tsinghua University, Beijing 100084, China*

[5] *State Key Laboratory of Mechanics and Control of Mechanical Structures, College of Aerospace Engineering, Nanjing University of Aeronautics and Astronautics, Nanjing 210016, China*

SUMMARY

For a Mindlin-Reissner plate subjected to transverse loadings, the distributions of the rotations and some resultant forces may vary very sharply within a narrow district near certain boundaries. This edge effect is indeed a great challenge for conventional finite element analysis. Recently, an effective hybrid displacement function (HDF) finite element method was successfully developed for solving such difficulty [1, 2]. Although good performances can be obtained in most cases, the distribution continuity of some resulting resultants is destroyed when coarse meshes are employed. Moreover, an additional local coordinate system must be used for avoiding singular problem in matrix inversion, which makes the derivations more complicated. Based on a modified complementary energy functional containing Lagrangian multipliers, an improved HDF (IHDF) element scheme is proposed in this work. And two new special IHDF elements, named by IHDF-P4-Free and IHDF-P4-SS1, are constructed for modeling plate behaviors near free and soft simply-supported (SS1) boundaries, respectively. The present modeling scheme not only greatly improves the precision of the numerical results, but also avoids usage of the additional local Coordinate system. The numerical tests demonstrate that the new IHDF element scheme is an effective way for solving the challenging edge effect problem in Mindlin-Reissner plates.

KEY WORDS: finite element; improved hybrid displacement function (IHDF) element scheme; Mindlin-Reissner plate; edge effect; Lagrangian multiplier

---

∗Correspondence to: Song Cen, Department of Engineering Mechanics, School of Aerospace Engineering, Tsinghua University, Beijing 100084, China.
†E-mail: censong@tsinghua.edu.cn

1. INTRODUCTION

When solving the Mindlin-Reissner plate bending problem, how to effectively capture the edge effect is a great challenge for theoretical and numerical analyses. The edge effect (or the boundary layer effect) is the phenomenon that the rotations and some resultant forces may vary very sharply within a narrow district (boundary layer) near free or soft simply-supported (SS1) boundaries. Babuška and Li [3] proved that such phenomenon indeed exists in 3D solutions. Rao *et al.* [4] also drew the same conclusions. Therefore, the existence of the edge effect reflects the real physical law. During past years, many scholars have analyzed this problem through semi-analytical methods, including the segmentation method [5, 6], the finite strip method [7], the asymptotic expansion method [8, 9], and so on [10-12]. But most of these semi-analytical methods can only handle the plates with rectangular shape. On the other hand, the finite element method (FEM) is generally recognized as the most efficient and convenient tool for analysis of plate/shell structures. However, the edge effect is also an obstacle for the FEM and few element models can easily deal with it. In order to obtain acceptable results in the boundary layers, a very refined mesh or an adaptive mesh refinement technique must be employed [13, 14]. Unfortunately, since the range of boundary layer is about the order of plate's thickness, the convergence rate will be very low while the computational cost is greatly increased. Therefore, such treatment is still uneconomical and unacceptable for practice applications. In addition, some other numerical methods, such as the *p*-Ritz method [15], have also been proposed for solving this problem. But they cannot perfectly overcome above difficulties, either.

In fact, for some real engineering applications, the edge effect may have great influences on the products, which means it cannot be ignored or even is of great interest. For instance, when designing a very large floating structure (VLFS), exact prediction for the resultants near the free boundaries is crucial [16]. Furthermore, similar phenomena also exist in folded plate structures [17] and composited plate structures [18, 19]. Therefore, how to efficiently handle such problems remains as an open and important topic.

Recently, Shang *et al.* [1] proposed a special finite element scheme based on the Hybrid Displacement Function (HDF) method, which is a simple version of Hybrid-Trefftz method [20-24], to solve the edge effect of the Mindlin-Reissner plate. Two special 4-node quadrilateral elements, HDF-P4-Free and HDF-P4-SS1, are successfully developed for modeling the boundary

2

layers, while the other regions are modeled by the conventional HDF plate element HDF-P4-11β [2]. During the construction procedures, the analytical solutions of two displacement functions, F and f [24, 25], are employed to determine the trial functions for the resultant fields within the special elements, in which f is related to the edge effect. Thus, they possess the ability to simulate the very steep gradients of resultants in the boundary layers. Furthermore, related zero-value resultant boundary conditions at free/SS1 edges are used as constraints to modify the assumed resultant fields, so that these boundary conditions can be exactly satisfied at element nodes. However, although this approach shows its efficiency and validity in solving the edge effect problem, it still experiences some obvious shortages. For example, a local Cartesian coordinate system must be used to avoid singular problem in matrix inversion when imposing related constraints on the resultant fields, which makes the derivations more complicated. In addition, when a relatively coarse mesh is used, improper discontinuity for the distribution of certain shear force may appear at interface where the special element HDF-P4-Free/HDF-P4-SS1 and the conventional element HDF-P4-11β connect.

To overcome above deficiencies, an improved scheme is proposed in this paper. Two new special elements, named by IHDF-P4-Free and IHDF-P4-SS1, are developed for simulating the plate behaviors in boundary layers of free and soft simply supported (SS1) boundaries, respectively. Different with the previous HDF method, these two IHDF elements are derived from a modified complementary energy functional containing the Lagrangian multipliers. Then, the constraints of related zero-value resultant boundary conditions at free/SS1 edges are imposed by the Lagrangian multiplier method. Therefore, the assumed resultant fields derived from the analytical solutions of the displacement functions F and f can be directly applied as the final trial functions, which means those complicated modifications and derivations brought by the additional local Coordinate system in developing HDF-P4-Free/HDF-P4-SS1 [1] can be avoided.

The content of this work is organized as follows: In Section 2, the detailed formulations of the new IHDF elements are presented. In Section 3, some numerical benchmark tests are operated to assess the validities of the present scheme. In these tests, these two IHDF elements will be allocated along free/SS1 edges for modeling the boundary layers, while the other regions are still modeled by HDF-P4-11β [2], as the original scheme [1] does. For comprehensive comparison, the results obtained by the original approach [1] are also provided. Finally, some conclusions are

drawn in Section 4. The present scheme effectively solves the edge effect problem. Compared with the original scheme [1], its derivations are more straightforward, and the resulting distributions of resultants are more smoothed.

2. THE IMPROVED HYBRID DISPLACEMENT FUNCTION (IHDF) ELEMENT METHOD

2.1. General formulations

As mentioned above, the derivations of the present IHDF elements are based on a modified complementary energy functional of Mindlin-Reissner plate:

$$\Pi_{MC}^{e} = \iint_{A^e} \frac{1}{2} \mathbf{R}^{\mathrm{T}} \mathbf{C} \mathbf{R} \mathrm{d}x \mathrm{d}y + \int_{S^e} \bar{\mathbf{R}}^{\mathrm{T}} \bar{\mathbf{d}} \mathrm{d}s + \int_{12} \boldsymbol{\lambda}^{\mathrm{T}} \bar{\mathbf{R}}_{cons} \mathrm{d}s \tag{1}$$

in which $\mathbf{R}$ is the element resultant vector and assumed as:

$$\mathbf{R} = \begin{Bmatrix} M_x \\ M_y \\ M_{xy} \\ T_x \\ T_y \end{Bmatrix} = \mathbf{S}\boldsymbol{\beta} + \mathbf{R}^*, \tag{2}$$

where $\mathbf{S}$ is the trial function matrix; $\boldsymbol{\beta}$ is the unknown coefficient vector; and $\mathbf{R}^*$ is the particular solution vector related to a distributed transverse loading q; $\mathbf{C}$ is the flexibility matrix of Mindlin-Reissner plate:

$$\mathbf{C} = \begin{bmatrix} \dfrac{1}{D(1-\mu^2)} & \dfrac{-\mu}{D(1-\mu^2)} & 0 & 0 & 0 \\[3mm] \dfrac{-\mu}{D(1-\mu^2)} & \dfrac{1}{D(1-\mu^2)} & 0 & 0 & 0 \\[3mm] 0 & 0 & \dfrac{2}{D(1-\mu)} & 0 & 0 \\[3mm] 0 & 0 & 0 & \dfrac{1}{C} & 0 \\[3mm] 0 & 0 & 0 & 0 & \dfrac{1}{C} \end{bmatrix}; \tag{3}$$

in which D and C are the bending and shear stiffness of the plate:

$$D = \frac{Eh^3}{12(1-\mu^2)}, \quad C = \frac{5}{6}Gh; \tag{4}$$

μ is Poisson's ratio; E, Young's modulus; $G = E/[2(1+\mu)]$, the shear modulus; h, the plate thickness; $\bar{\mathbf{R}}$ is the resultant vector along the boundary, and can be obtained by:

4

$$\bar{\mathbf{R}} = \mathbf{LR}, \text{ with } \mathbf{L} = \begin{bmatrix} l^2 & m^2 & 2lm & 0 & 0 \\ -lm & lm & l^2 - m^2 & 0 & 0 \\ 0 & 0 & 0 & -l & -m \end{bmatrix}, \tag{5}$$

where l and m denote the direction cosines of outer normal of the boundary; $\bar{\mathbf{d}}$ is the element's boundary displacement vector and can be interpolated by the element's nodal displacement vector $\mathbf{q}^e$:

$$\bar{\mathbf{d}} = \bar{\mathbf{N}}\big|_\Gamma \mathbf{q}^e ; \tag{6}$$

in which $\bar{\mathbf{N}}\big|_\Gamma$ is the interpolation matrix and will be discussed in details in Section 2.2. The last term in Equation (1) provides certain constraints on the assumed resultant fields, in which $\bar{\mathbf{R}}_{cons}$ represents the related resultant boundary conditions at free/SS1 edges; and $\boldsymbol{\lambda}$ is the Lagrangian multiplier vector. $\bar{\mathbf{R}}_{cons}$ can be expressed by:

$$\bar{\mathbf{R}}_{cons} = \mathbf{L}_{cons}\mathbf{R} = \mathbf{L}_{cons}\mathbf{S}\boldsymbol{\beta} + \mathbf{L}_{cons}\mathbf{R}^* . \tag{7}$$

For different constraints, $\bar{\mathbf{R}}_{cons}$ and $\mathbf{L}_{cons}$ will have different expressions. These will also be discussed in Section 2.2.

By substituting Equations (2-7) into Equation (1), the modified functional Π_{MC}^e can be written as:

$$\Pi_{MC}^e = \frac{1}{2}\boldsymbol{\beta}^\mathrm{T}\mathbf{M}\boldsymbol{\beta} + \frac{1}{2}\boldsymbol{\beta}^\mathrm{T}\mathbf{M}^* + \frac{1}{2}\mathbf{M}^{*\mathrm{T}}\boldsymbol{\beta} + \frac{1}{2}\mathbf{Q} + \boldsymbol{\beta}^\mathrm{T}\mathbf{H}\mathbf{q}^e + \mathbf{V}\mathbf{q}^e + \boldsymbol{\lambda}^\mathrm{T}\boldsymbol{\Gamma}_1\boldsymbol{\beta} + \boldsymbol{\lambda}^\mathrm{T}\boldsymbol{\Gamma}_2 , \tag{8}$$

with

$$\mathbf{M} = \iint_{A^e} \mathbf{S}^\mathrm{T}\mathbf{C}\mathbf{S}\,\mathrm{d}x\mathrm{d}y , \tag{9}$$

$$\mathbf{M}^* = \iint_{A^e} \mathbf{S}^\mathrm{T}\mathbf{C}\mathbf{R}^*\,\mathrm{d}x\mathrm{d}y , \tag{10}$$

$$\mathbf{H} = \int_{S^e} \mathbf{S}^\mathrm{T}\mathbf{L}^\mathrm{T}\,\bar{\mathbf{N}}\big|_\Gamma\,\mathrm{d}s , \tag{11}$$

$$\mathbf{Q} = \iint_{A^e} \mathbf{R}^{*\mathrm{T}}\mathbf{C}\mathbf{R}^*\,\mathrm{d}x\mathrm{d}y , \tag{12}$$

$$\mathbf{V} = \int_{S^e} \mathbf{R}^{*\mathrm{T}}\mathbf{L}^\mathrm{T}\,\bar{\mathbf{N}}\big|_\Gamma\,\mathrm{d}s , \tag{13}$$

$$\boldsymbol{\Gamma}_1 = \int_{12} \mathbf{L}_{cons}\mathbf{S}\,\mathrm{d}s , \tag{14}$$

$$\boldsymbol{\Gamma}_2 = \int_{12} \mathbf{L}_{cons} \mathbf{R}^* \mathrm{d}s \,, \tag{15}$$

where 12 denotes the free/SS1 boundary edge of a special element. Then, applying the stationary condition of functional Π^e_{MC} with respect to the variables $\boldsymbol{\lambda}$ and $\boldsymbol{\beta}$ yields

$$\frac{\partial \Pi^e_{MC}}{\partial \boldsymbol{\lambda}} = \boldsymbol{\Gamma}_1 \boldsymbol{\beta} + \boldsymbol{\Gamma}_2 = \mathbf{0} \,, \tag{16}$$

$$\frac{\partial \Pi^e_{MC}}{\partial \boldsymbol{\beta}} = \mathbf{M}\boldsymbol{\beta} + \mathbf{M}^* + \mathbf{H}\mathbf{q}^e + \boldsymbol{\Gamma}_1^{\mathrm{T}}\boldsymbol{\lambda} = \mathbf{0} \,. \tag{17}$$

From above two equations, we can obtain

$$\boldsymbol{\lambda} = -\mathbf{H}^\lambda \mathbf{q}^e + \mathbf{V}^\lambda \,, \tag{18}$$

with

$$\mathbf{H}^\lambda = \left(\boldsymbol{\Gamma}_1 \mathbf{M}^{-1} \boldsymbol{\Gamma}_1^{\mathrm{T}} \right)^{-1} \boldsymbol{\Gamma}_1 \mathbf{M}^{-1} \mathbf{H} \,, \tag{19}$$

$$\mathbf{V}^\lambda = \left(\boldsymbol{\Gamma}_1 \mathbf{M}^{-1} \boldsymbol{\Gamma}_1^{\mathrm{T}} \right)^{-1} \left(\boldsymbol{\Gamma}_2 - \boldsymbol{\Gamma}_1 \mathbf{M}^{-1} \mathbf{M}^* \right) \,. \tag{20}$$

Next, by substituting Equation (18) into Equation (17), $\boldsymbol{\beta}$ can also be expressed by $\mathbf{q}^e$:

$$\boldsymbol{\beta} = -\mathbf{M}^{-1} \left(\hat{\mathbf{H}}\mathbf{q}^e + \hat{\mathbf{M}}^* \right) \,, \tag{21}$$

with

$$\hat{\mathbf{H}} = \mathbf{H} - \boldsymbol{\Gamma}_1^{\mathrm{T}}\mathbf{H}^\lambda \,, \tag{22}$$

$$\hat{\mathbf{M}}^* = \mathbf{M}^* + \boldsymbol{\Gamma}_1^{\mathrm{T}}\mathbf{V}^\lambda \,. \tag{23}$$

Finally, by substituting Equations (18) and (21) into Equation (8) and applying the stationary condition of functional Π^e_{MC} with respect to $\mathbf{q}^e$, the final equations to be solved are obtained:

$$\mathbf{K}^e \mathbf{q}^e = \mathbf{P}^e_q \,, \tag{24}$$

in which $\mathbf{K}^e$ is the element stiffness matrix:

$$\mathbf{K}^e = -\hat{\mathbf{H}}^{\mathrm{T}}\mathbf{M}^{-1}\hat{\mathbf{H}} + \hat{\mathbf{H}}^{\mathrm{T}}\mathbf{M}^{-1}\mathbf{H} + \mathbf{H}^{\mathrm{T}}\mathbf{M}^{-1}\hat{\mathbf{H}} - \mathbf{H}^{\lambda^{\mathrm{T}}}\boldsymbol{\Gamma}_1\mathbf{M}^{-1}\hat{\mathbf{H}} - \hat{\mathbf{H}}^{\mathrm{T}}\mathbf{M}^{-1}\boldsymbol{\Gamma}_1^{\mathrm{T}}\mathbf{H}^\lambda \,, \tag{25}$$

and $\mathbf{P}^e_q$ is the element equivalent load vector caused by the distributed transverse loading q:

$$\mathbf{P}^e_q = \hat{\mathbf{H}}^{\mathrm{T}}\mathbf{M}^{-1}\hat{\mathbf{M}}^* - \hat{\mathbf{H}}^{\mathrm{T}}\mathbf{M}^{-1}\mathbf{M}^* - \mathbf{H}^{\mathrm{T}}\mathbf{M}^{-1}\hat{\mathbf{M}}^* + \mathbf{V}^{\mathrm{T}} - \hat{\mathbf{H}}^{\mathrm{T}}\mathbf{M}^{-1}\boldsymbol{\Gamma}_1^{\mathrm{T}}\mathbf{V}^\lambda + \mathbf{H}^{\lambda^{\mathrm{T}}}\boldsymbol{\Gamma}_1\mathbf{M}^{-1}\hat{\mathbf{M}}^* - \mathbf{H}^{\lambda^{\mathrm{T}}}\boldsymbol{\Gamma}_2 \,. \tag{26}$$

After $\mathbf{q}^e$ in Equation (24) is solved, $\boldsymbol{\beta}$ can be obtained by Equation (21). Thus, the resultants at arbitrarily point within an element can be derived using Equation (2).

2.2. Formulations of new elements

As defined in Figure 1, the quadrilateral element IHDF-P4-Free/IHDF-P4-SS1 is represented by its mid-surface 1234, in which edge 12 is a segment of the free/SS1 boundary. Its nodal displacement (DOF) vector is

$$\mathbf{q}^e = \begin{bmatrix} w_1 & \psi_{x1} & \psi_{y1} & w_2 & \psi_{x2} & \psi_{y2} & w_3 & \psi_{x3} & \psi_{y3} & w_4 & \psi_{x4} & \psi_{y4} \end{bmatrix}^{\mathrm{T}}. \qquad (27)$$

2.2.1 The displacement functions F and f

As discussed in [1, 2], Hu [25] proposed that the displacement components of Mindlin-Reissner plate can be derived from two displacement functions:

$$\psi_x = \frac{\partial F}{\partial x} + \frac{\partial f}{\partial y}, \quad \psi_y = \frac{\partial F}{\partial y} - \frac{\partial f}{\partial x}, \quad w = F - \frac{D}{C}\nabla^2 F, \qquad (28)$$

in which F and f should satisfy

$$D\nabla^2\nabla^2 F = q, \qquad (29)$$

$$\frac{1}{2}(1-\mu)D\nabla^2 f - Cf = 0. \qquad (30)$$

Similar works were also presented in form of the Trefftz functions [21-24]. Then, by substituting Equation (28) into related governing equations, all the strain and stress components of a Mindlin-Reissner plate can be obtained.

2.2.2 The trial functions for resultant fields of new elements

Same as the original HDF method [1], the trial functions for resultant fields of new IHDF elements are also derived from the displacement functions F and f. Thus, Equation (2) can be specifically rewritten as

$$\mathbf{R} = \mathbf{R}(F, f) = \mathbf{S}(F, f)\boldsymbol{\beta} + \mathbf{R}^*; \qquad (31)$$

with

$$\mathbf{S}(F, f) = \begin{bmatrix} \mathbf{R}_1^0 & \mathbf{R}_2^0 & \mathbf{R}_3^0 & \mathbf{R}_4^0 & \mathbf{R}_5^0 & \mathbf{R}_6^0 & \mathbf{R}_7^0 & \mathbf{R}_8^0 & \mathbf{R}_9^0 & \mathbf{R}_{10}^0 & \mathbf{R}_{11}^0 & \mathbf{R}_1^f & \mathbf{R}_2^f \end{bmatrix}, (32)$$

$$\boldsymbol{\beta} = \begin{bmatrix} \beta_1 & \beta_2 & \beta_3 & \beta_4 & \cdots & \beta_{13} \end{bmatrix}^{\mathrm{T}}. \qquad (33)$$

Since the analytical solutions of displacement functions and the corresponding resulting resultant solutions have already been proposed in [1], the detailed expressions of Equation (32) are directly

7

listed in Appendix A.

2.2.3 The boundary displacement modes of new elements

To determine the new hybrid element's boundary displacement modes, the locking-free Timoshenko's beam is employed, as the original HDF method [1, 2] does. Furthermore, the normal rotation of each edge is assumed as a linear variation. Related contents are also available in references [1, 2]. Thus for simplicity, the detailed components of $\bar{\mathbf{N}}\big|_{\Gamma}$ in Equation (6) are directly presented in Appendix B.

2.2.4 Related constraints on the resultant fields of new elements

For the free edge 12, as shown in Figure 1, the boundary resultant field should satisfy the following conditions:

$$\bar{\mathbf{R}}_{free} = \left\{ \begin{array}{c} \bar{M}_n \\ \bar{M}_{ns} \\ -\bar{T}_n \end{array} \right\}_{free} = \mathbf{0} . \tag{34}$$

Thus, $\bar{\mathbf{R}}_{cons}$ and $\mathbf{L}_{cons}$ in Equation (7) can be written as:

$$\bar{\mathbf{R}}_{cons} = \bar{\mathbf{R}}_{free} , \tag{35}$$

$$\mathbf{L}_{cons} = \mathbf{L}_{cons}^{free} = \begin{bmatrix} l_x^{*2} & l_y^{*2} & 2l_x^* l_y^* & 0 & 0 \\ -l_x^* l_y^* & l_x^* l_y^* & l_x^{*2} - l_y^{*2} & 0 & 0 \\ 0 & 0 & 0 & -l_x^* & -l_y^* \end{bmatrix} , \tag{36}$$

where l_x^* and l_y^* denote the direction cosines of outer normal of the free edge 12.

Then, by substituting Equations (35) and (36) into those equations in previous sections, the final formulations of the element IHDF-P4-Free can be obtained. This element will be specially used for modeling the boundary layers near free edges.

For the SS1 edge 12, the related resultant boundary conditions are:

$$\bar{\mathbf{R}}_{SS1} = \left\{ \begin{array}{c} \bar{M}_n \\ \bar{M}_{ns} \end{array} \right\}_{SS1} = \mathbf{0} . \tag{37}$$

Correspondingly, the specific expressions of $\bar{\mathbf{R}}_{cons}$ and $\mathbf{L}_{cons}$ in Equation (7) are:

$$\bar{\mathbf{R}}_{cons} = \bar{\mathbf{R}}_{SS1}, \tag{38}$$

$$\mathbf{L}_{cons} = \mathbf{L}_{cons}^{SS1} = \begin{bmatrix} l_x^{*2} & l_y^{*2} & 2l_x^* l_y^* & 0 & 0 \\ -l_x^* l_y^* & l_x^* l_y^* & l_x^{*2} - l_y^{*2} & 0 & 0 \end{bmatrix}, \tag{39}$$

where l_x^* and l_y^* denote the direction cosines of outer normal of the SS1 edge 12. Similarly, substitution of Equations (38) and (39) into equations in previous sections yields the final formulations of the element IHDF-P4-SS1. This element will be employed to simulate the behaviors in boundary layers near SS1 edges.

In fact, Equation (7) can also be used to handle constrained problems of other types. Related works will be presented in our future work.

3. NUMERICAL TESTS

Several numerical tests are investigated to assess the present scheme's validity. In these tests, the new elements IHDF-P4-Free and IHDF-P4-SS1 are allocated along the free and SS1 edges, respectively, to capture the plate behaviors in the boundary layers, while HDF-P4-11β [2] are used for modeling other domains. For comprehensive comparison, results obtained by both the present and original schemes [1] are provided.

Remarks: In this section, "F" means the free edge; "S*" means soft simply-supported (SS1) edge and "S" means hard simply-supported edge (SS2).

3.1. *The soft simply-supported (SS1) thick square plate*

Figure 2 depicts a quarter of the SS1 thick square plate subjected to a uniformly distributed transverse loading, with Poisson's ratio μ=0.3. For simplicity, it is denoted as $S^* S^* S^* S^*$ plate. Figure 2(a) shows the regular mesh commonly used for most quadrilateral elements. When solving thin $S^* S^* S^* S^*$ plate, many Mindlin-Reissner plate elements can provide satisfactory results of central displacement/stress, in which HDF-P4-11β [2] seems to be the most outstanding one. However, when handling the thick $S^* S^* S^* S^*$ case, their performances will more or less deteriorate. The reason may be related to the existence of the edge effect, whose domain of influence is about the order of plate thickness. Here, to verify the influences of the edge effect on the computation convergence of elements, the boundary layers will be designedly modeled by the special element

IHDF-P4-SS1. That is to say, element IHDF-P4-SS1 is allocated along the SS1 edges, and the other regions are still modeled by HDF-P4-11β. Note that, since there are two SS1 edges connect at the corners of the plate, the peculiar mesh shown in Figure 2(b) is employed, in which the square grid near the corner splits into two degenerated triangles. As IHDF-P4-SS1 possesses the significant advantage of the HDF elements, i.e. insensitive to severe mesh distortion, its performance in such distorted mesh can still be guaranteed.

For the plate with span-thickness ratio a/h=10, the convergence plots of normalized central deflections and bending moments are given by Figures 3 and 4. For comparison, the results obtained by the original scheme [1] and other well-known elements, including ARS-Q12 [26], Q4BL [27], S4R [28], AC-MQ4 [29], and PQI [30], are also given. Table I also lists the results calculated by the presented method and the original schemes with and without the influence of the edge effect [1, 2]. Furthermore, for the cases with larger span-thickness ratios a/h=100, 1000 and 10000, the convergence tests are performed, and the normalized central deflections are provided in Tables II to IV with the results proposed by Santos *et al*. [31]. Note that the order of the Gaussian integration in the new elements should be adjusted by following the rules proposed in [1]. It can be seen that the present method, in which the influences of edge effect are particularly considered, converges more rapidly to the reference Mindlin-Reissner plate solutions [31].

This test shows that the existences of the boundary layers may have significant influences on the convergence rate, especially for thick plate cases. Therefore engineers and scholars should pay enough attention to the edge effect problem.

3.2. The square plate with two opposite edges hard simply-supported

As shown in Figure 5, a square plate with two opposite edges hard simply-supported is subjected to a uniformly distributed loading q. The other two edges are free or soft simply-supported. For simplicity, they are denoted as SFSF case and SS^*SS^* case, respectively. Owing to symmetry, only a quarter is modeled. And Poisson's ratio μ=0.3. Two different span-thickness ratio cases, a/h=50 and 100, are considered. For the case a/h=50, Kant and his coauthors [5, 6] have derived the semi-analytical solutions by the segmentation method. And for the case a/h=100, results obtained by using a refined 100×100 mesh are adopted as the reference solutions.

To effectively capture the behaviors in the boundary layers, the following typical mesh shown in Figure 5 is employed: the new special elements will be allocated along the special free/SS1 edges, while the other regions are still modeled by the conventional element HDF-P4-11β [2]. As described in the Section 4.3 in [1], the width of the boundary layer is approximately of the order of plate's thickness. Thus, the characteristic sizes of the special elements should be restrained. For comparison, the results obtained by the original scheme [1] and Abaqus elements [28] are also provided here.

3.2.1. The SFSF case

In this case, the element IHDF-P4-Free will be used for modeling the boundary layers near the free edges.

For the case a/h=50, Table V lists the results of displacements and resultants calculated at some specified positions. It can be seen that, both the present and original schemes can give satisfactory results, performing much better than the Abaqus elements S4 and S4R [28]. Figures 6 and 8 respectively give the distributions of the twisting moment M_{xy} and shear force T_y, obtained in coarse mesh 4×4 and fine mesh 32×32, along the edge AB. The corresponding contour plots are given in Figures 7 and 9. Figures 10 and 11 respectively depict the distribution of the shear force T_x along the symmetric edge DC and the contour plot.

It can be seen that, if the Abaqus element S4 was employed to solve the edge effect problem, only poor results can be obtained, neither capturing the very steep gradients nor satisfying the related resultant boundary conditions, see the red boxes over Abaqus results in these figures. When predicting the distributions of M_{xy} and T_x, the peak values wrongly occur at the free edges. In fact, these values at the free edges should be zero. Even though the results can be improved by refining the mesh, the related resultant boundary conditions still cannot be satisfied. On the contrary, the present IHDF and original HDF schemes can provide excellent performances, even when only the coarse mesh 4×4 is used.

It should be emphasized that in Figures 10 and 11, when using the original HDF scheme [1], the results of shear force T_x show certain discontinuities at the conjunctive areas between the special and conventional elements. In contrast, the results obtained by the new IHDF scheme are much more smoothed, especially in the coarse mesh. Furthermore, with the refinement of the mesh, the

results of both new and old schemes will agree well with the reference solutions, as shown in Figure 12.

For the case a/h=100, resultant distributions and corresponding contour plots calculated in coarse mesh 8×8 and fine mesh 32×32 are shown in Figures 13 to 18. Same conclusions with the previous case a/h=50 can be obtained.

3.2.2. The SS*SS* case

In this case, the element IHDF-P4-SS1 will be allocated along the SS1 edges.

For the case a/h=50, results of some displacements and resultants are listed in Table VI. Figures 19 to 22 give the distributions of the twisting moment M_{xy} and shear force T_y along the edge AB and the corresponding contour plots. The distribution along the symmetric edge DC and the contour plot of shear force T_x are respectively shown in Figures 23 and 24. It can be seen that, although the peak value of the shear force T_x at the boundary exhibits some oscillations, the results will finally converge to the reference solutions once the mesh is refined (see Figure 25). The results of the case a/h=100 are also provided in Figures 26-31. From this test, it can be concluded again that, the present IHDF scheme can efficiently simulate the behaviors in the boundary layers even in a coarse mesh, while the Abaqus elements fail [28].

3.2.3. Computation efficiency test

To compare the computation efficiencies of the new and previous schemes, the mean computation time of the plate with span-thickness ratio a/h=50 are provided in Table VII. Besides, the case that all elements are the conventional HDF elements is considered. It can be seen that, the schemes with the edge effect will not obviously bring extra computational costs, while excellent results can be obtained even when only a coarse mesh is used.

A standard front method solver is used and the program is executed by a personal computer with an 'Intel Core i7-3770' (Intel Corp., Mountain View, CA, USA) CPU and 4 GB of memory.

3.3. The 60° skew plate with two opposite edges hard simply-supported

As shown in Figure 32, a 60° skew plate with two opposite edges hard simply-supported (SS2), is subjected to a uniformly transverse load q. The other two edges are both free, or both soft

simply-supported (SS1). For simplicity, they are respectively denoted as the SFSF case and the SS*SS* case. The plate's thickness h=0.1, span a=5 and Poisson's ratio $\mu = 0.3$.

Two typical meshes, the regular mesh (a) and distorted mesh (b), are also illustrated in Figure 32. The boundary layers near free/SS1 edges will be modeled by the special IHDF elements. In this benchmark, the elements are also rhombic due to the shape of the plate. Thus, it is to assess the abilities of the present IHDF elements in oblique meshes.

In Figures 33 to 36, the distributions of twist moment M_{xy}, shear forces T_x and T_y along the supported edge AB for the SFSF case and SS*SS* case, which are calculated by the regular mesh (a) and the distorted mesh (b), are respectively presented. The results obtained by using a very fine mesh 200×200 are taken as the reference solutions. It is well-known that, the obtuse corner B is a singular point, where stress concentrations take place [32]. In Figures 37 to 40, the resultant distributions along the path EF are also provided. It can be observed that the results of IHDF scheme are in good agreement with the reference solutions in the regions far away from the obtuse corner B, no matter the regular or the distorted mesh is employed.

3.4. The 30° Morley skew plate

As shown in Figure 41, a 30° skew plate [33] with all edges soft simply-supported (SS1) is subjected to a uniformly transverse load q. The span-thickness ratio a/h= 100, Young modulus E = 10.92 and Poisson's ratio $\mu = 0.3$. Along the SS1 edges, special element IHDF-P4-SS1 are allocated for modeling the boundary layers, while the other regions are modeled by element HDF-P4-11β. Note that there are two SS1 edges connect at the plate vertex, one quadrilateral corner element will be divided into two degenerated triangular IHDF elements. Since the shapes of the IHDF and HDF elements are quite free, such distortion will not deteriorate the performance of the present scheme.

In Table VIII, the dimensionless central deflections and principal bending moments are listed for comparing the capabilities of the proposed IHDF formulations with other finite elements [29, 31, 34, 35]. It can be seen that the present method converges very rapidly and agrees with the reference 3D solution [36] much better than others.

Figures 42 and 43 depict the distributions of dimensionless resultants along the path AB and EF, respectively. The results obtained in refine mesh 200×200 are also presented as the reference

solutions. This test proves again that the IHDF scheme can provide satisfactory resultant distributions in the regions far away from the singular obtuse corners, efficiently modeling the behaviors in the boundary layers.

3.5. The Circular plate

As shown in Figure 44, a circular plate is subjected to a uniform transverse load q, with all edges soft simply-supported (SS1). Owing to the symmetry, only a quarter is modeled. The radius is $R= 5$, Young modulus $E = 10.92$ and Poisson's ratio $\mu = 0.3$. Two different thicknesses $h = 0.1$ and 1 are considered.

Tables IX and X give the normalized central deflections and bending moments calculated by different element models [26, 29, 34, 35, 37]. It can be seen that the results obtained by the presented IHDF scheme and the conventional HDF plate element HDF-P4-11β [2] both converge rapidly into the reference solutions [38, 39].

4. CONCLUSIONS

Due to the shortage of effective method, the edge effect problem of Mindlin-Reissner plate is often ignored. However, the existences of boundary layers may have significant effects on the convergences and bring about great difficulties for exactly capturing the resultant distributions. In this work, an improved version based on the original HDF scheme [1] for analysis of the edge effect problem of Mindlin-Reissner plate is presented. According to the new scheme, two new special elements, IHDF-P4-Free and IHDF-P4-SS1, are constructed for modeling the boundary layers near free and SS1 edges, respectively. Different with the models proposed in Ref. [1], the constructions of these new elements are based on a modified complementary energy functional including Lagrangian multipliers. Through this way, the influences of related resultant boundary conditions at the free/SS1 edge on the resultant field are considered in a weak form. Thus, the resultant solutions derived from the analytical solutions of displacement functions F and f can be directly employed as the final resultant trial functions within the element without further modification. Besides, the boundary displacement modes of the elements are also determined by the locking-free Timoshenko's beam, as the treatments given by Refs. [1] and [2]. Similar to the original scheme, the new IHDF elements are allocated along the plate boundaries for modeling the

14

boundary layers, while other regions are still modeled by element HDF-P4-11β [2].

Numerical tests prove that this present scheme can also effectively solve the edge effect problem, exactly capturing the behavior in the boundary layers and providing satisfactory results for both displacements and resultants. Moreover, compared with the previous HDF scheme [1], the new scheme exhibits two distinct advantages: (i) the distributions of shear forces in a coarse mesh calculated by the new scheme are much more smoothed; and (ii) the usage of the additional local Cartesian coordinate system in HDF scheme [1] for imposing boundary constraints is avoided. Therefore, the formulations of the present IHDF elements are more straightforward and much simpler.

APPENDIX A

The solution of the displacement function F in Equation (28) can be divided into the general part F^0 and the particular part F^*:

$$D\nabla^2\nabla^2 F^0 = 0 , \tag{A1}$$

$$D\nabla^2\nabla^2 F^* = q . \tag{A2}$$

The analytical solutions of F^0 in polynomial form and the resulting resultant solutions have already obtained in [1]. Here, they are only listed in Table AI. For a uniformly distributed transverse loading q, F^* can be written as

$$F^* = \frac{q}{48D}\left(x^4 + y^4\right). \tag{A3}$$

Correspondingly, the resultants are

$$\mathbf{R}^* = \begin{Bmatrix} M_x^* \\ M_y^* \\ M_{xy}^* \\ T_x^* \\ T_y^* \end{Bmatrix} = \begin{Bmatrix} -\dfrac{q}{4}\left(x^2 + \mu y^2\right) \\ -\dfrac{q}{4}\left(y^2 + \mu x^2\right) \\ 0 \\ -\dfrac{q}{2}x \\ -\dfrac{q}{2}y \end{Bmatrix}. \tag{A4}$$

For an element along the free or SS1 edge, as shown in Figure 1, edge 12 is a segment of the special boundary. Two solutions of the displacement function f in Equation (29) are given by [1]:

$$f_1 = -\frac{1}{D} e^{mx+ny-a_0} , \tag{A5}$$

$$f_2 = -\frac{1}{D}(nx-my)e^{mx+ny-a_0} , \tag{A6}$$

with

$$m = \frac{\sqrt{10}}{h}\frac{y_2-y_1}{l_{12}} , \quad n = \frac{\sqrt{10}}{h}\frac{x_1-x_2}{l_{12}} , \tag{A7}$$

$$a_0 = mx_1 + ny_1 = mx_2 + ny_2 . \tag{A8}$$

h is the plate's thickness; (x_1, y_1), (x_2, y_2) are the Cartesian coordinates of nodes 1 and 2; and l_{12} is the length of edge 12. Figure A1 plots the distributions of these two solutions over a square domain, and Table AII lists the resulting resultant solutions.

APPENDIX B

For the new elements, the boundary displacement modes are determined by the locking-free Timoshenko's beam [1, 2], as shown in Figure B1. $\left.\bar{\mathbf{N}}\right|_\Gamma$ in Equation (5) is a 3×12 matrix. For simplicity, its detailed components are directly proposed.

For the edge ij ($i = \overline{1,2,3,4}$; $j = \overline{2,3,4,1}$), the following labels are defined:

$$\text{Lab}1 = 3\times(i-1)+1, \quad \text{Lab}2 = 3\times(j-1)+1 . \tag{B1}$$

Then, the non-zero components of $\left.\bar{\mathbf{N}}\right|_\Gamma$ are:

$$\left.\bar{\mathbf{N}}\right|_\Gamma(1,\text{lab}1+1) = -\frac{y_{ij}}{l_{ij}}(1-s) , \quad \left.\bar{\mathbf{N}}\right|_\Gamma(1,\text{lab}1+2) = \frac{x_{ij}}{l_{ij}}(1-s) ,$$

$$\left.\bar{\mathbf{N}}\right|_\Gamma(1,\text{lab}2+1) = -\frac{y_{ij}}{l_{ij}}s , \quad \left.\bar{\mathbf{N}}\right|_\Gamma(1,\text{lab}2+2) = \frac{x_{ij}}{l_{ij}}s ,$$

$$\left.\bar{\mathbf{N}}\right|_\Gamma(2,\text{lab}1) = -\frac{6}{l_{ij}}(1-2\delta_{ij})Z_2 , \quad \left.\bar{\mathbf{N}}\right|_\Gamma(2,\text{lab}1+1) = -\frac{x_{ij}}{l_{ij}}\Big[1-s-3(1-2\delta_{ij})Z_2\Big] ,$$

$$\left.\bar{\mathbf{N}}\right|_\Gamma(2,\text{lab}1+2) = -\frac{y_{ij}}{l_{ij}}\Big[1-s-3(1-2\delta_{ij})Z_2\Big] , \quad \left.\bar{\mathbf{N}}\right|_\Gamma(2,\text{lab}2) = \frac{6}{l_{ij}}(1-2\delta_{ij})Z_2 ,$$

$$\left.\bar{\mathbf{N}}\right|_\Gamma(2,\text{lab}2+1) = -\frac{x_{ij}}{l_{ij}}\Big[s-3(1-2\delta_{ij})Z_2\Big] , \quad \left.\bar{\mathbf{N}}\right|_\Gamma(2,\text{lab}2+2) = -\frac{y_{ij}}{l_{ij}}\Big[s-3(1-2\delta_{ij})Z_2\Big] ,$$

$$\left.\bar{\mathbf{N}}\right|_\Gamma(3,\text{lab}1) = 1-s+(1-2\delta_{ij})Z_3 , \quad \left.\bar{\mathbf{N}}\right|_\Gamma(3,\text{lab}1+1) = -\frac{x_{ij}}{2}\Big[Z_2+(1-2\delta_{ij})Z_3\Big] ,$$

$$\left.\bar{\mathbf{N}}\right|_{\Gamma}(3,\mathrm{lab}1+2)=-\frac{y_{ij}}{2}\left[Z_2+\left(1-2\delta_{ij}\right)Z_3\right],\quad \left.\bar{\mathbf{N}}\right|_{\Gamma}(3,\mathrm{lab}2)=s-\left(1-2\delta_{ij}\right)Z_3\,,$$

$$\left.\bar{\mathbf{N}}\right|_{\Gamma}(3,\mathrm{lab}2+1)=\frac{x_{ij}}{2}\left[Z_2-\left(1-2\delta_{ij}\right)Z_3\right],\quad \left.\bar{\mathbf{N}}\right|_{\Gamma}(3,\mathrm{lab}2+2)=\frac{y_{ij}}{2}\left[Z_2-\left(1-2\delta_{ij}\right)Z_3\right],$$

(B2)

with

$$Z_2=s(1-s),\quad Z_3=s(1-s)(1-2s),\quad \delta_{ij}=6\lambda_{ij}\big/\left(1+12\lambda_{ij}\right),\quad \lambda_{ij}=D\big/Cl_{ij}^2\,,\qquad\text{(B3)}$$

where D and C are given in Equation (30); $s=\dfrac{1+\xi}{2}$, $\xi\left(-1\le\xi\le1\right)$ is the one-dimension isoparametric coordinate along the edge ij; $l_{ij}^2=x_{ij}^2+y_{ij}^2$ with $x_{ij}=x_i-x_j$, $y_{ij}=y_i-y_j$.

ACKNOWLEDGEMENTS

REFERENCES

[1] Shang Y, Cen S, Li CF, Huang JB. An effective hybrid displacement function element method for solving the edge effect of Mindlin-Reissner plate. *International Journal for Numerical Methods in Engineering* 2015; **102**(8): 1449-1487.

[2] Cen S, Shang Y, Li CF, Li HG. Hybrid displacement function element method: a simple hybrid-Trefftz stress element method for analysis of Mindlin-Reissner plate. *International Journal for Numerical Methods in Engineering* 2014; **98**(3): 203-234.

[3] Babuška I, Li I. The problem of plate modeling: Theoretical and computational results. *Computer Methods in Applied Mechanics and Engineering* 1992; **100**(2): 249-273.

[4] Rao NVR, Ozakca M, Hinton E. A study of boundary-layers in plates using Mindlin-Reissner and 3-D elements. *International Journal for Numerical Methods in Engineering* 1992; **33**(6):1305-1320.

[5] Kant T, Hinton E. Mindlin plate analysis by segmentation method. *Journal of Engineering Mechanics* 1983; **109**(2):537-556.

[6] Kant T, Gadgil MG. Analysis of orthotropic plates based on three theories by segmentation method. *Mechanics of Advanced Materials and Structures* 2002; **9**(3):189-239.

[7] Hinton E, Selman A, Alkhamis M. Boundary-layers in uniform and variable thickness plates with rectangular and curved planforms using the finite strip method. *Communications in Numerical Methods in Engineering* 1995; **11**(7):597-606.

[8] Arnold DN, Falk RS. The boundary layer for the Reissner-Mindlin plate model. *SIAM Journal on Mathematical Analysis* 1990; **21**(2):281-312.

[9] Arnold DN, Falk RS. Asymptotic analysis of the boundary layer for the Reissner-Mindlin plate model. *SIAM*

Journal on Mathematical Analysis 1996; **27**(2): 486-514.

[10] Nosier A, Yavari A, Sarkani S. Study of edge-zone equation of Mindlin-Reissner plate theory. *Journal of Engineering Mechanics* 2000; **126**(6): 647-651.

[11] Naumenko K, Altenbach J, Altenbach H, Naumenko V. Closed and approximate analytical solutions for rectangular Mindlin plates. *Acta Mechanica* 2001; **147**(1-4): 153-172.

[12] Brank B. On boundary layer in the Mindlin plate model: Levy plates. *Thin-walled Structures* 2008; **46**(5): 451-465.

[13] Mukherjee S, Krishnamoorthy CS. Adaptive FE analysis of plates by shear-flexible quadrilateral Reissner-Mindlin elements. *Finite Elements in Analysis and Design* 1996; **22**(4): 329-366.

[14] Selman A, Hinton E, Bicanic N. Adaptive mesh refinement for localised phenomena. *Computers & Structures* 1997; **63**(3):475-495.

[15] Wang CM, Wang YC, Reddy JN, Thevendran V. Improved computation of stress resultants in the *p*-Ritz method. *Journal of Structural Engineering-ASCE* 2002; **128**(2):249-257.

[16] Wang CM, Xiang Y, Utsunomiya T, Watanabe E. Evaluation of modal stress resultants in freely vibrating plates. *International Journal of Solids and Structures* 2001; **38**(36-37):6525-6558.

[17] Maunder EAW, Izzuddin BA. A hybrid equilibrium element for folded plate and shell structures. *International Journal for Numerical Methods in Engineering* 2013; **95**(6): 451-477.

[18] Vidal P, Polit O, D'Ottavio M, Valot E. Assessment of the refined sinus plate finite element: Free edge effect and Meyer-Piening sandwich test. *Finite Elements in Analysis and Design* 2014; **92**(0): 60-71.

[19] Nosier A, Yavari A, Sarkani S. A study of the edge-zone equation of Mindlin-Reissner plate theory in bending of laminated rectangular plates. *Acta Mechanica* 2001; **146**(3-4): 227-238.

[20] Jirousek J. Guex L. The hybrid-Trefftz finite element model and its application to plate bending. *International Journal for Numerical Methods in Engineering* 1986; **23**: 651-693.

[21] Jirousek J, Wróblewski A, Szybinski B. A new 12 DOF quadrilateral element for analysis of thick and thin plates. *International Journal for Numerical Methods in Engineering* 1995; **38**: 2619-2638.

[22] Teixeira de Freitas JA. Formulation of elastostatic hybrid-Trefftz stress elements. *Computer Methods in Applied Mechanics and Engineering* 1998; **153**: 127-151.

[23] Petrolito J. Hybrid-Trefftz quadrilateral elements for thick plate analysis. *Computer Methods in Applied Mechanics and Engineering* 1990; **78**(3): 331-351.

[24] Jirousek J, Wróblewski A, Qin QH, He XQ. A family of quadrilateral hybrid-Trefftz p-elements for thick plate analysis. *Computer Methods in Applied Mechanics and Engineering* 1995; **127**: 315-344.

[25] Hu HC. *Variational principle of Theory of Elasticity with Applications.*Science press, Gordon and Breach, Science publisher: Beijing 1984.

[26] Soh AK, Cen S, Long ZF, Long YQ. A new twelve DOF quadrilateral element for analysis of thick and thin plates. *European Journal of Mechanics A-Solids* 2001; **20**(2): 299-326.

[27] Zienkiewicz OC, Xu ZN, Zeng LF, Samuelsson A, Wiberga NE. Linked interpolation for Ressiner-Mindlin plate element: part I-a simple quadrilateral. *International Journal for Numerical Methods in Engineering* 1993; **36**(18): 3043-3056.

[28] Abaqus 6.9. *HTML Documentation*. Dassault Systèmes Simulia Corp.: Providence, RI, USA, 2009.

[29] Cen S, Long YQ, Yao ZH, Chiew SP. Application of the quadrilateral area co-ordinate method: A new element for Mindlin-Reissner plate. *International Journal for Numerical Methods in Engineering* 2006; **66**(1): 1-45.

[30] Ibrahimbegovic A. Plate quadrilateral finite elements with incompatible modes. *Communications in Applied Numerical Methods* 1992; **8**(8): 497-504.

[31] Santos HAFA, Evans JA, Hughes TJR. Generalization of the twist-Kirchhoff theory of plate elements to arbitrary quadrilaterals and assessment of convergence. *Computer Methods in Applied Mechanics and Engineering* 2012; **209**:101-14.

[32] Haggblad B, Bathe KJ. Specifications of boundary-conditions for Reissner-Mindlin plate bending finite elements. *International Journal for Numerical Methods in Engineering* 1990; **30**(5): 981-1011.

[33] Morley LSD. Skew Plates and Structures. *International Series of Monographs in Aeronautics and Astronautics*. Macmillan: New York 1963.

[34] Bathe KJ, Dvorkin EN. A four-node plate bending element based on Mindlin-Reissner plate theory and a mixed interpolation. *International Journal for Numerical Methods in Engineering* 1985; **21**(2): 367-383.

[35] Katili I. A new discrete Kirchhoff-Mindlin element based on Mindlin-Reissner plate theory and assumed shear strain fields—Part II: An extended DKQ element for thick-plate bending analysis. *International Journal for Numerical Methods in Engineering* 1993; **36**(11): 1885-1908.

[36] Babuška I, Scapolla T. Benchmark computation and performance evaluation for a rhombic plate bending problem. *International Journal for Numerical Methods in Engineering* 1989; 28(1):155-179.

[37] Hu B, Wang Z, Xu YC. Combined hybrid method applied in the Reissner-Mindlin plate model. *Finite Elements in Analysis and Design* 2010; **46**: 428-437.

[38] Ayad R, Rigolot A. An improved four-node hybrid-mixed element based upon Mindlin's plate theory. *International Journal for Numerical Methods in Engineering* 2002; **55**: 705-731.

[39] Shang Y, Cen S, Li CF, et al. Two generalized conforming quadrilateral Mindlin-Reissner plate elements based on the displacement function. *Finite Elements in Analysis and Design* 2015, **99**: 24-38.

Table I. The normalized central deflections and moments of $S^*S^*S^*S^*$ square plate, with *a/h*=10

Mesh	2×2	4×4	8×8	16×16	32×32	Reference [2]
Normalized central deflection w_c/w_{ref}						
HDF-P4-11β [2]	0.9455	0.9675	0.9899	0.9974	0.9993	
HDF-P4-SS1+HDF-P4-11β [1]	0.9855	0.9964	0.9999	0.9999	0.9998	1.0000*
IHDF-P4-SS1+HDF-P4-11β	**0.9962**	**0.9999**	**0.9995**	**0.9994**	**0.9997**	
Normalized central moment M_c/M_{ref}						
HDF-P4-11β [2]	0.9976	0.9681	0.9906	0.9976	0.9994	
HDF-P4-SS1+HDF-P4-11β [1]	0.9805	0.9934	0.9990	0.9996	0.9997	1.0000**
IHDF-P4-SS1+HDF-P4-11β	**0.9780**	**0.9954**	**0.9986**	**0.9993**	**0.9996**	

* the dimensionless reference deflection $w_{ref}/(qL^4/100D)$ is 0.4617

** the dimensionless reference moment $M_{ref}/(qL^2/10)$ is 0.5096

Table II. The normalized central deflections of $S^*S^*S^*S^*$ square plates, with a/h=100

Mesh	4×4	8×8	16×16	32×32	Reference [31]
HDF-P4-11β [2]	0.9916	0.9916	0.9922	0.9949	
Santos *et al.* [31]	0.9967	0.9930	0.9916	0.9913	1.0000*
IHDF-P4-SS1+HDF-P4-11β	**1.0000**	**1.0000**	**1.0000**	**0.9999**	

* the dimensionless reference deflection $w_{ref}/(qL^4/100D)$ is 0.40993

Table III. The normalized central deflections of $S^*S^*S^*S^*$ square plates, with a/h=1000

Mesh	4×4	8×8	16×16	32×32	Reference [31]
HDF-P4-11β [2]	0.9991	0.9991	0.9991	0.9991	
Santos *et al.* [31]	1.0046	1.0009	0.9996	0.9992	1.0000*
IHDF-P4-SS1+HDF-P4-11β	**1.0000**	**1.0000**	**1.0000**	**1.0000**	

* the dimensionless reference deflection $w_{ref}/(qL^4/100D)$ is 0.40659

Table IV. The normalized central deflections of $S^*S^*S^*S^*$ square plates, with *a/h*=10000

Mesh	4×4	8×8	16×16	32×32	Reference [31]
HDF-P4-11β [2]	0.9999	0.9999	0.9999	0.9999	
Santos [31]	1.0054	1.0017	1.0004	1.0000	1.0000*
IHDF-P4-SS1+HDF-P4-11β	**1.0000**	**1.0000**	**1.0000**	**1.0000**	

* the dimensionless reference deflection $w_{ref}/(qL^4/100D)$ is 0.40627

Table V. The dimensionless deflections and resultants at certain positions for SFSF case, a/h=50

	Mesh N×N	4×4	8×8	16×16	32×32	100×100	Kant [5,6]
$\dfrac{w_C \cdot D}{qa^4}$	S4 [28]	0.01274	0.01302	0.01309	0.01310	0.01311	
	S4R [28]	0.01274	0.01302	0.01309	0.01310	0.01311	0.0131
	HDF-P4-Free+HDF-P4-11β [1]	0.01311	0.01311	0.01311	0.01311	0.01311	
	IHDF-P4-Free+HDF-P4-11β	**0.01311**	**0.01311**	**0.01311**	**0.01311**	**0.01311**	
$\dfrac{w_D \cdot D}{qa^4}$	S4 [28]	0.01464	0.01495	0.01504	0.01506	0.01507	
	S4R [28]	0.01467	0.01496	0.01504	0.01506	0.01507	0.0150
	HDF-P4-Free+HDF-P4-11β [1]	0.01507	0.01507	0.01507	0.01507	0.01507	
	IHDF-P4-Free+HDF-P4-11β	**0.01507**	**0.01507**	**0.01507**	**0.01507**	**0.01507**	
$\dfrac{M_{xC}}{qa^2}$	S4 [28]	0.02577	0.02663	0.02680	0.02682	0.02683	
	S4R [28]	0.02622	0.02674	0.02683	0.02683	0.02683	0.0268
	HDF-P4-Free+HDF-P4-11β [1]	0.02650	0.02675	0.02681	0.02682	0.02683	
	IHDF-P4-Free+HDF-P4-11β	**0.02649**	**0.02675**	**0.02681**	**0.02683**	**0.02683**	
$\dfrac{M_{yC}}{qa^2}$	S4 [28]	0.1181	0.1214	0.1222	0.1224	0.1225	
	S4R [28]	0.1187	0.1216	0.1223	0.1224	0.1225	0.122
	HDF-P4-Free+HDF-P4-11β [1]	0.1228	0.1226	0.1225	0.1225	0.1225	
	IHDF-P4-Free+HDF-P4-11β	**0.1229**	**0.1226**	**0.1225**	**0.1225**	**0.1225**	
$\dfrac{M_{yD}}{qa^2}$	S4 [28]	0.1286	0.1308	0.1308	0.1306	0.1304	
	S4R [28]	0.1248	0.1288	0.1300	0.1304	0.1305	0.130
	HDF-P4-Free+ HDF-P4-11β [1]	0.1304	0.1304	0.1304	0.1305	0.1304	
	IHDF-P4-Free+HDF-P4-11β	**0.1305**	**0.1302**	**0.1302**	**0.1303**	**0.1304**	
$\dfrac{T_{yB}}{qa}$	S4 [28]	0.3862	0.4354	0.4525	0.4602	0.4654	
	S4R [28]	0.3866	0.4355	0.4525	0.4602	0.4654	0.463
	HDF-P4-Free+HDF-P4-11β [1]	0.4381	0.4552	0.4634	0.4656	0.4669	
	IHDF-P4-Free+HDF-P4-11β	**0.4385**	**0.4552**	**0.4634**	**0.4657**	**0.4669**	

Table VI. The dimensionless deflections and resultants at certain positions for SS*SS* case, a/h=50

Mesh N×N		4×4	8×8	16×16	32×32	100×100	Kant [5,6]
$\dfrac{w_C \cdot D}{qa^4}$	S4 [28]	0.00406	0.00409	0.00410	0.00410	0.00411	
	S4R [28]	0.00409	0.00409	0.00410	0.00410	0.00411	0.0041
	HDF-P4-SS1+HDF-P4-11β [1]	0.00410	0.00410	0.00411	0.00411	0.00411	
	IHDF-P4-SS1+HDF-P4-11β	**0.00411**	**0.00411**	**0.00411**	**0.00411**	**0.00411**	
$\dfrac{M_{xC}}{qa^2}$	S4 [28]	0.04802	0.04803	0.04808	0.04812	0.04813	
	S4R [28]	0.04658	0.04768	0.04800	0.04809	0.04813	0.0481
	HDF-P4-SS1+HDF-P4-11β [1]	0.04806	0.04809	0.04811	0.04812	0.04813	
	IHDF-P4-SS1+HDF-P4-11β	**0.04807**	**0.4809**	**0.04811**	**0.04812**	**0.04813**	
$\dfrac{M_{yC}}{qa^2}$	S4 [28]	0.04812	0.04811	0.04820	0.04825	0.04827	
	S4R [28]	0.04661	0.04776	0.04811	0.04822	0.04826	0.0482
	HDF-P4-SS1+HDF-P4-11β [1]	0.04821	0.04822	0.04825	0.04827	0.04827	
	IHDF-P4-SS1+HDF-P4-11β	**0.04822**	**0.04823**	**0.04825**	**0.04826**	**0.04827**	
$\dfrac{T_{yA}}{qa}$	S4 [28]	−0.2987	−0.7059	−1.3600	−2.2399	−3.7097	
	S4R [28]	−0.2895	−0.7004	−1.3574	−2.2391	−3.7097	−5.214
	HDF-P4-SS1+HDF-P4-11β [1]	−5.0873	−5.0741	−5.0394	−5.0738	−5.1447	
	IHDF-P4-SS1+HDF-P4-11β	**−5.3109**	**−5.2051**	**−5.1155**	**−5.0429**	**−5.0869**	
$\dfrac{T_{yB}}{qa}$	S4 [28]	0.3056	0.3104	0.3235	0.3314	0.3367	
	S4R [28]	0.3050	0.3104	0.3235	0.3314	0.3367	0.333
	HDF-P4-SS1+HDF-P4-11β [1]	0.3076	0.3154	0.3208	0.3299	0.3372	
	IHDF-P4-SS1+HDF-P4-11β	**0.3067**	**0.3154**	**0.3208**	**0.3299**	**0.3372**	
$\dfrac{T_{xD}}{qa}$	S4 [28]	0.2624	0.2988	0.3296	0.3578	0.3916	
	S4R [28]	0.2625	0.2987	0.3295	0.3578	0.3916	0.419
	HDF-P4-SS1+HDF-P4-11β [1]	0.4226	0.4095	0.3697	0.3563	0.3925	
	IHDF-P4-SS1+HDF-P4-11β	**0.4152**	**0.3906**	**0.3418**	**0.3505**	**0.3929**	

Table VII. The mean computing time (second) for the square plate with two opposite SS2 edges, a/h=50

Mesh	4×4	8×8	16×16	32×32	100×100
SFSF case					
All HDF-P4-11β	0.0624	0.2090	0.8986	5.0700	215.6402
HDF-P4-Free+HDF-P4-11β [1]	0.1030	0.2808	1.0608	5.5193	217.1378
IHDF-P4-Free +**HDF-P4-11β**	**0.1030**	**0.2714**	**1.0390**	**5.3290**	**216.7166**
SS*SS* case					
All HDF-P4-11β	0.0624	0.2184	0.9048	5.0950	215.9834
HDF-P4-SS1+HDF-P4-11β [1]	0.1030	0.2870	1.0452	5.2884	216.2018
IHDF-P4-SS1+HDF-P4-11β	**0.1030**	**0.2839**	**1.0390**	**5.2822**	**216.0458**

* 16×16 Gauss integration is used for IHDF-P4-Free and IHDF-P4-SS1

Table VIII. Central deflections and principal bending moments of 30° Morley plate ($a/h=100$)

Mesh N×N	4×4	8×8	16×16	32×32	Morley's thin plate solutions [33]	3D Solution [34]
(a) Central deflection $w_o/(qL^4/1000D)$						
MITC4 [34]	0.359	0.357	0.383	0.404		
DKMQ [35]	0.757	0.504	0.441	0.423		
AC-MQ4 [29]	0.431	0.410	0.407	0.409		
Santos *et al.* [31]	0.435	0.437	0.421	0.418		
HDF-P4-11β [2]	0.463	0.427	0.421	0.420		
IHDF-P4-SS1+HDF-P4-11β	**0.462**	**0.430**	**0.424**	**0.423**	0.408	0.423
(b) Central max principal moment $M_{max}/(qL^2/100)$						
MITC4 [34]	1.670	1.782	1.844	1.894		
DKMQ [35]	2.330	2.073	1.984	1.945		
AC-MQ4 [29]	2.157	2.121	1.990	1.933		
Santos *et al.* [31]	1.678	1.931	1.945	1.930		
HDF-P4-11β [2]	2.198	1.882	1.942	1.937		
IHDF-P4-SS1+HDF-P4-11β	**2.183**	**1.895**	**1.953**	**1.949**	1.910	
(c) Central min principal moment $M_{min}/(qL^2/100)$						
MITC4 [34]	0.921	0.999	1.046	1.076		
DKMQ [35]	1.740	1.267	1.166	1.135		
AC-MQ4 [29]	1.379	1.328	1.170	1.105		
Santos *et al.* [31]	0.477	0.767	0.970	1.109		
HDF-P4-11β [2]	1.400	1.108	1.157	1.130		
IHDF-P4-SS1+HDF-P4-11β	**1.482**	**1.114**	**1.163**	**1.140**	1.080	

Table IX. Normalized central deflections and bending moments of the circular plate, h=0.1

Number of elements	12	48	192	Reference
Normalized central deflection				
MITC4 [34]	0.980	0.995	—	
DKMQ [35]	0.990	0.998	—	
ARS-Q12 [26]	0.990	0.997	0.999	1.000*
CHRM [37]	0.967	0.992	0.998	
AC-MQ4 [29]	1.006	1.001	1.000	
HDF-P4-11β [2]	1.007	1.002	1.000	
IHDF-P4-SS1+HDF-P4-11β	**1.007**	**1.002**	**1.000**	
Normalized central moment				
MITC4 [34]	0.989	0.997	—	
DKMQ [35]	1.009	1.003	—	
ARS-Q12 [26]	1.009	1.003	1.001	1.000**
CHRM [37]	1.001	1.008	1.000	
AC-MQ4 [29]	1.021	1.006	1.001	
HDF-P4-11β [2]	1.005	1.001	1.000	
IHDF-P4-SS1+HDF-P4-11β	**1.005**	**1.001**	**1.000**	

*normalized by the reference solution 39831.5

** normalized by the reference solution 5.15625

Table X. Normalized central deflections and bending moments of the circular plate, $h=1$

Number of elements	12	48	192	Reference
Normalized central deflection				
MITC4 [34]	0.980	0.995	—	
DKMQ [35]	0.988	0.997	—	
ARS-Q12 [26]	0.988	0.997	0.999	1.000*
CHRM [37]	0.970	0.993	0.998	
AC-MQ4 [29]	0.996	0.998	1.000	
HDF-P4-11β [2]	1.005	1.001	1.000	
IHDF-P4-SS1+HDF-P4-11β	**1.005**	**1.001**	**1.000**	
Normalized central moment				
MITC4 [34]	0.987	0.997	—	
DKMQ [35]	1.014	1.005	—	
ARS-Q12 [26]	1.015	1.004	1.001	1.000**
CHRM [37]	0.993	0.998	1.000	
AC-MQ4 [29]	1.025	1.007	1.002	
HDF-P4-11β [2]	1.003	1.001	1.000	
IHDF-P4-SS1+HDF-P4-11β	**1.003**	**1.001**	**1.000**	

*normalized by the reference solution 41.5994

** normalized by the reference solution 5.15625

Table AI. Eleven items of analytical solutions of F^0 and the resulting resultant solutions

i		1	2	3	4	5	6	7
$-DF_i^0$		x^2	xy	y^2	x^3	x^2y	xy^2	y^3
$\mathbf{R}_i^0$	M_{xi}^0	2	0	2μ	$6x$	$2y$	$2\mu x$	$6\mu y$
	M_{yi}^0	2μ	0	2	$6\mu x$	$2\mu y$	$2x$	$6y$
	M_{xyi}^0	0	$1-\mu$	0	0	$2(1-\mu)x$	$2(1-\mu)y$	0
	T_{xi}^0	0	0	0	6	0	2	0
	T_{yi}^0	0	0	0	0	2	0	6

i		8	9	10	11
$-DF_i^0$		x^3y	xy^3	x^4-y^4	$6x^2y^2-x^4-y^4$
$\mathbf{R}_i^0$	M_{xi}^0	$6xy$	$6\mu xy$	$12(x^2-\mu y^2)$	$12(1-\mu)(y^2-x^2)$
	M_{yi}^0	$6\mu xy$	$6xy$	$-12(y^2-\mu x^2)$	$12(1-\mu)(x^2-y^2)$
	M_{xyi}^0	$3(1-\mu)x^2$	$3(1-\mu)y^2$	0	$24(1-\mu)xy$
	T_{xi}^0	$6y$	$6y$	$24x$	0
	T_{yi}^0	$6x$	$6x$	$-24y$	0

Table AII. Two items of analytical solutions of f and the resulting resultant solutions

j		1	2
f_j		$-\dfrac{1}{D}e^{mx+ny-a_0}$	$-\dfrac{1}{D}(nx-my)e^{mx+ny-a_0}$
$\mathbf{R}_j^f$	M_{xj}^f	$(1-\mu)mne^{mx+ny-a_0}$	$(1-\mu)\left[(nx-my)mn+n^2-m^2\right]e^{mx+ny-a_0}$
	M_{yj}^f	$-(1-\mu)mne^{mx+ny-a_0}$	$-(1-\mu)\left[(nx-my)mn+n^2-m^2\right]e^{mx+ny-a_0}$
	M_{xyj}^f	$\dfrac{1}{2}(1-\mu)(n^2-m^2)e^{mx+ny-a_0}$	$\dfrac{1}{2}(1-\mu)\left[-4mn+(nx-my)(n^2-m^2)\right]e^{mx+ny-a_0}$
	T_{xj}^f	$\dfrac{C}{D}ne^{mx+ny-a_0}$	$\dfrac{C}{D}\left[(nx-my)n-m\right]e^{mx+ny-a_0}$
	T_{yj}^f	$-\dfrac{C}{D}me^{mx+ny-a_0}$	$-\dfrac{C}{D}\left[(nx-my)m+n\right]e^{mx+ny-a_0}$
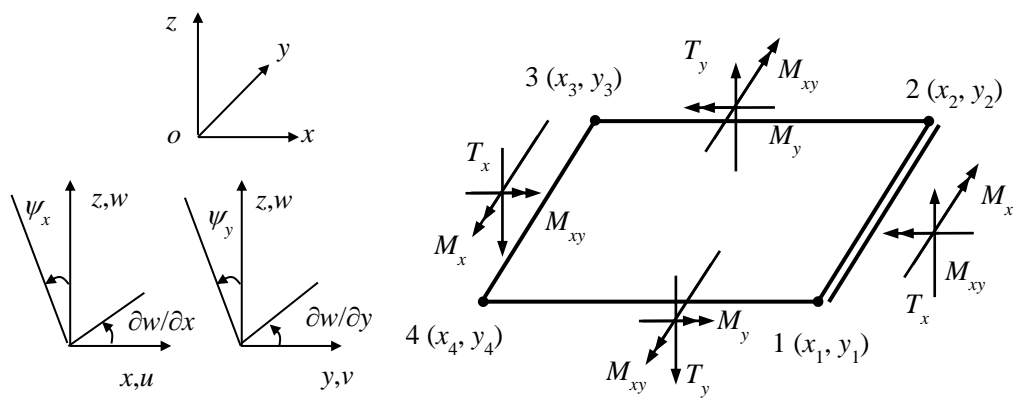
Figure 1. The definitions of the special element along the free/SS1 edge 12
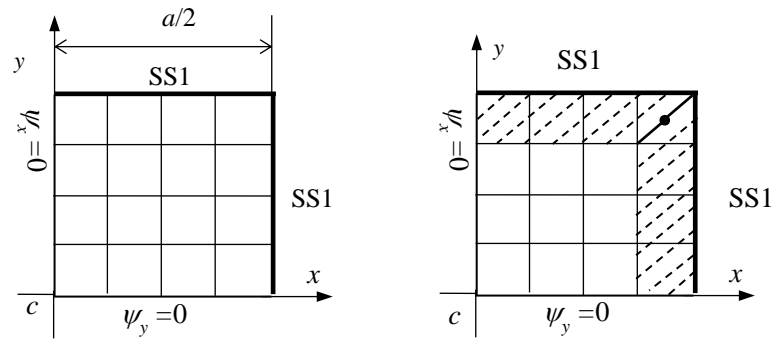
a) Regular mesh   b) Special mesh

Special element

Figure 2. A quarter of the square SS1 plate with $a/h=10$
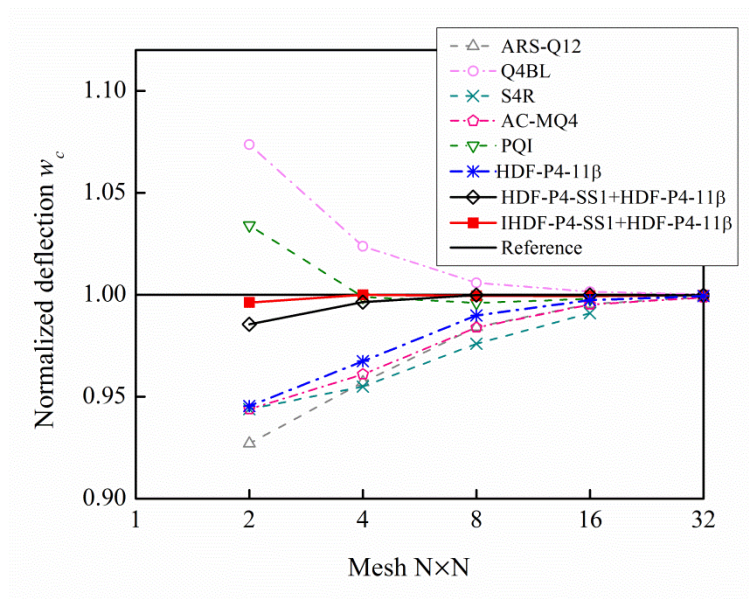
Figure 3. The convergence plot of the dimensionless central deflection of the thick $S^*S^*S^*S^*$ square plate
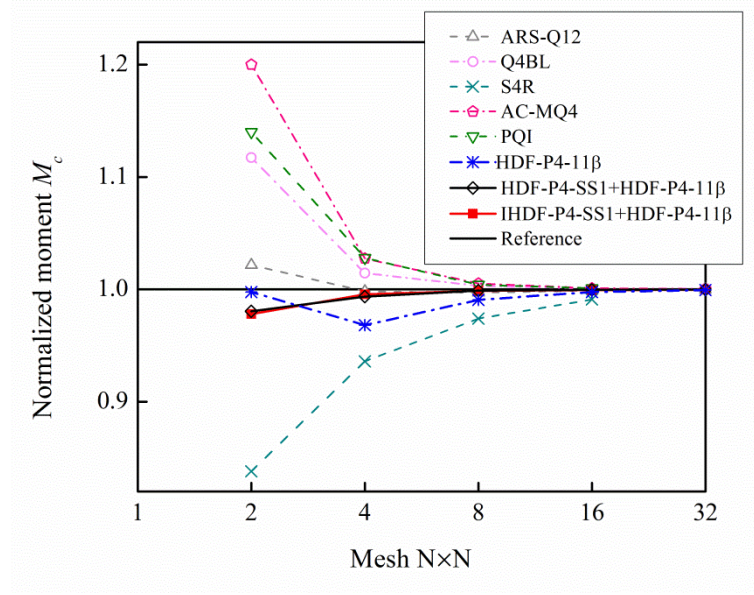
Figure 4. The convergence plot of the dimensionless central moment of the thick $S^*S^*S^*S^*$ square plate
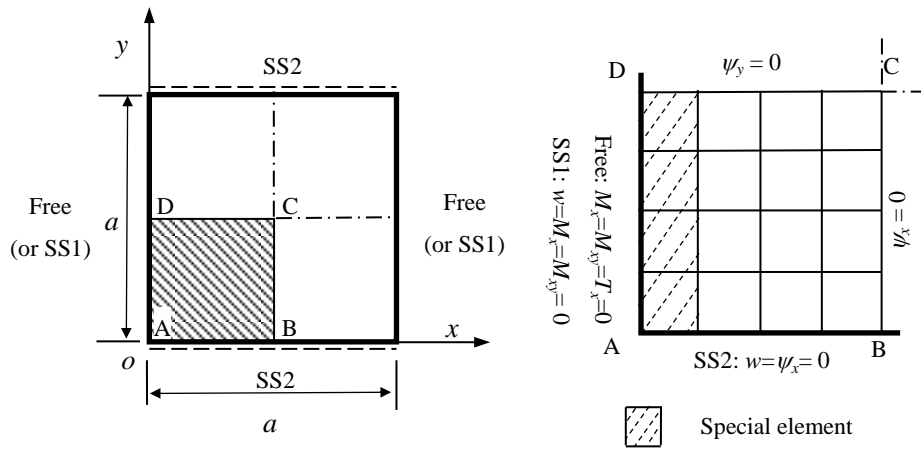
Figure 5. The square plate with two opposite edges hard simply-supported (SS2) and the typical mesh
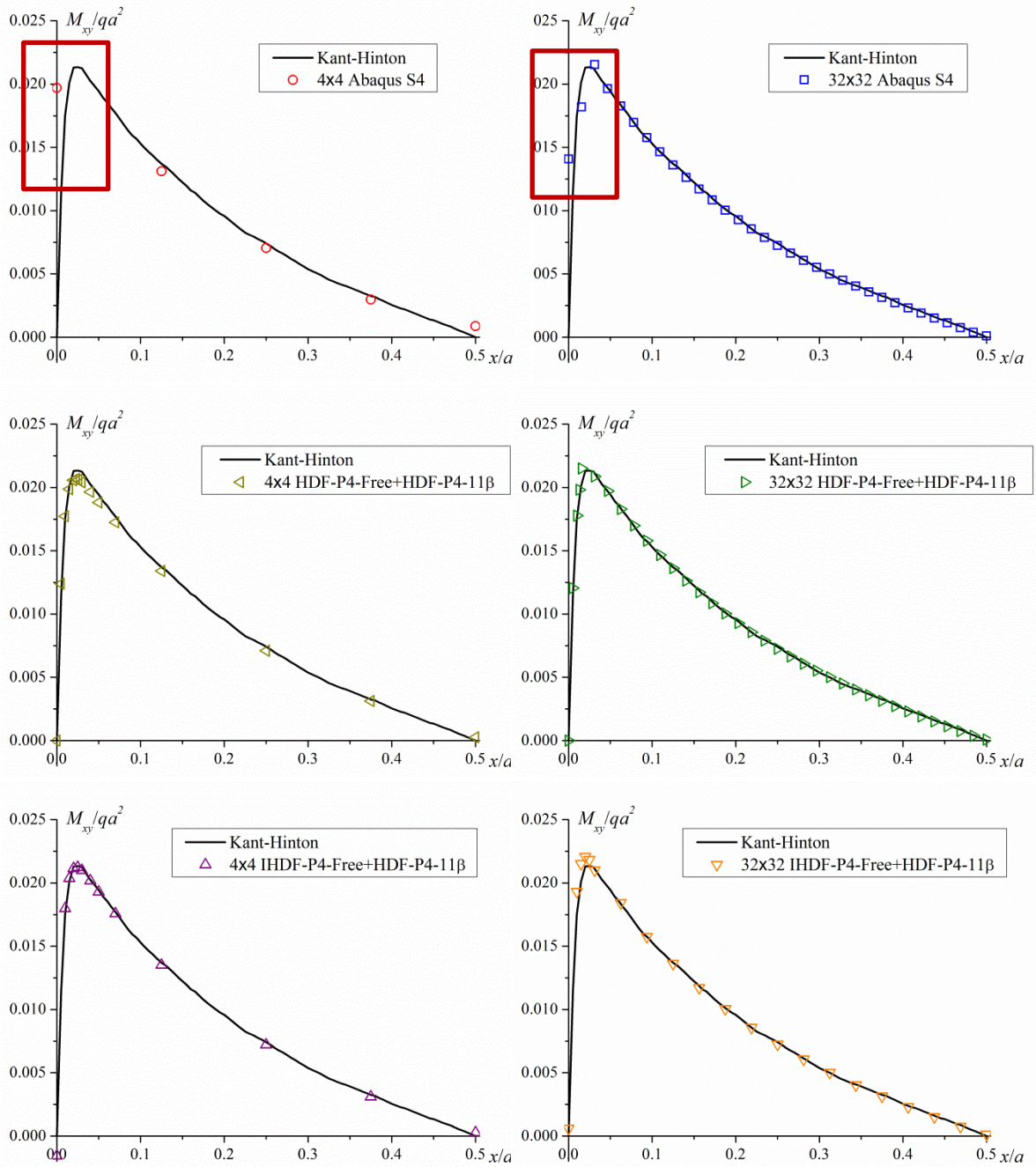
Figure 6. The distribution along the edge AB of twisting moment M_{xy}/qa^2 for SFSF case with a/h=50, calculated by Abaqus S4 (top), the old scheme (middle) and the present scheme (bottom), in coarse mesh and fine mesh

Abaqus S4:   Left-mesh 4×4   Right-mesh 32×32

HDF-P4-Free+HDF-P4-11β: Left-mesh 4×4   Right-mesh 32×32

IHDF-P4-Free+HDF-P4-11β: Left-mesh 4×4   Right-mesh 32×32
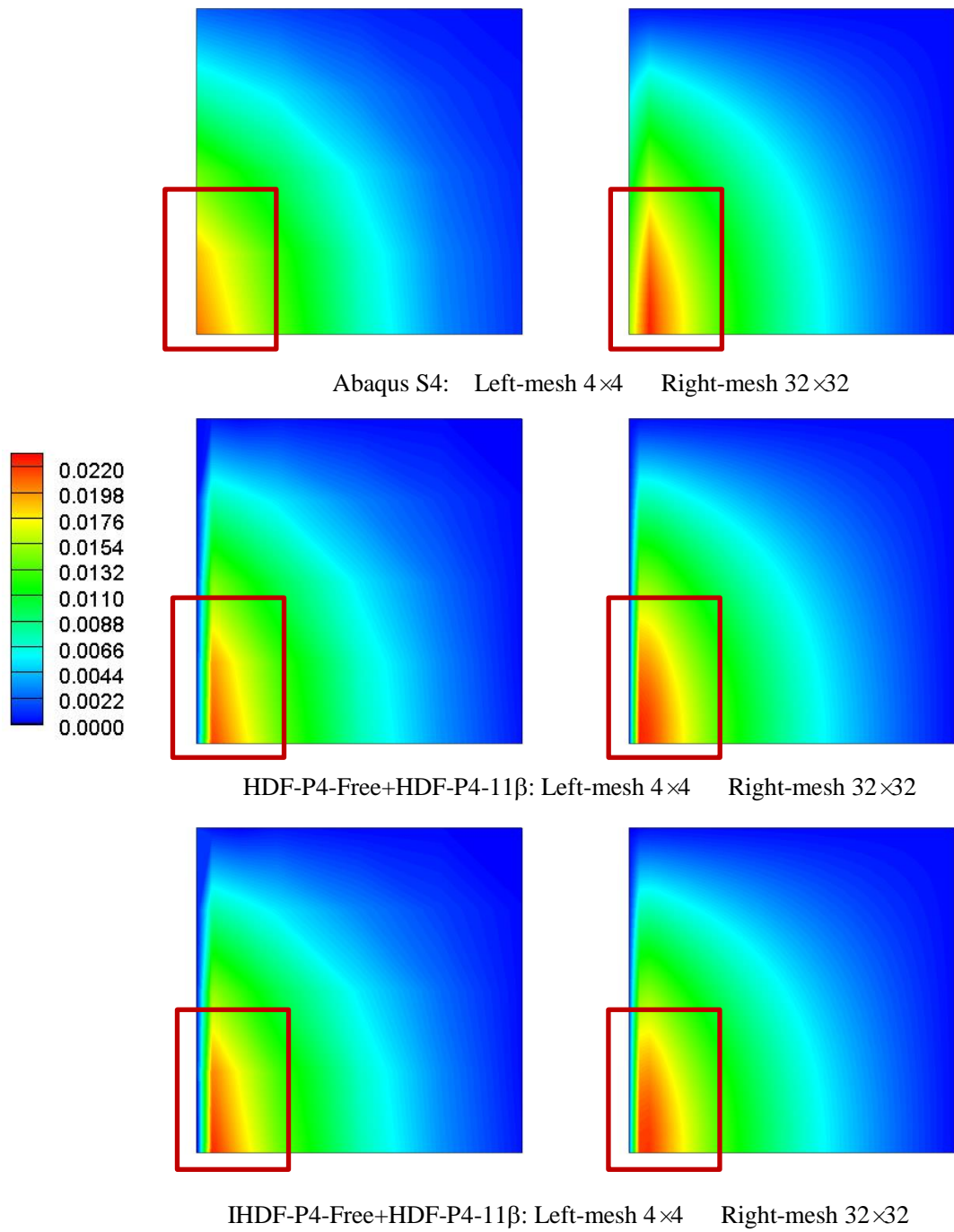
Figure 7. The contour plot of twisting moment M_{xy}/qa^2 for SFSF case with a/h=50, calculated by Abaqus S4 (top), the old scheme (middle) and the present scheme (bottom), in coarse mesh and fine mesh
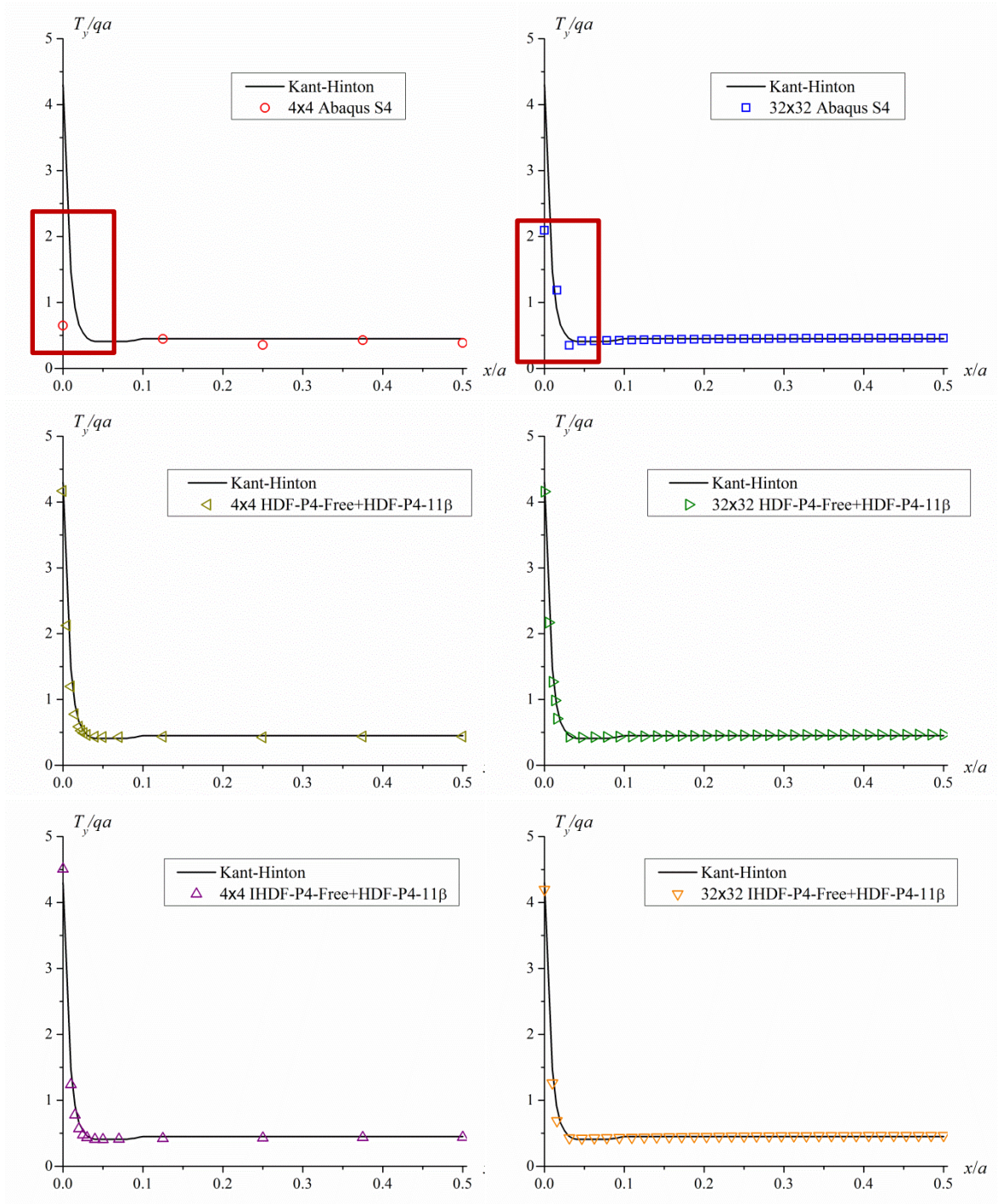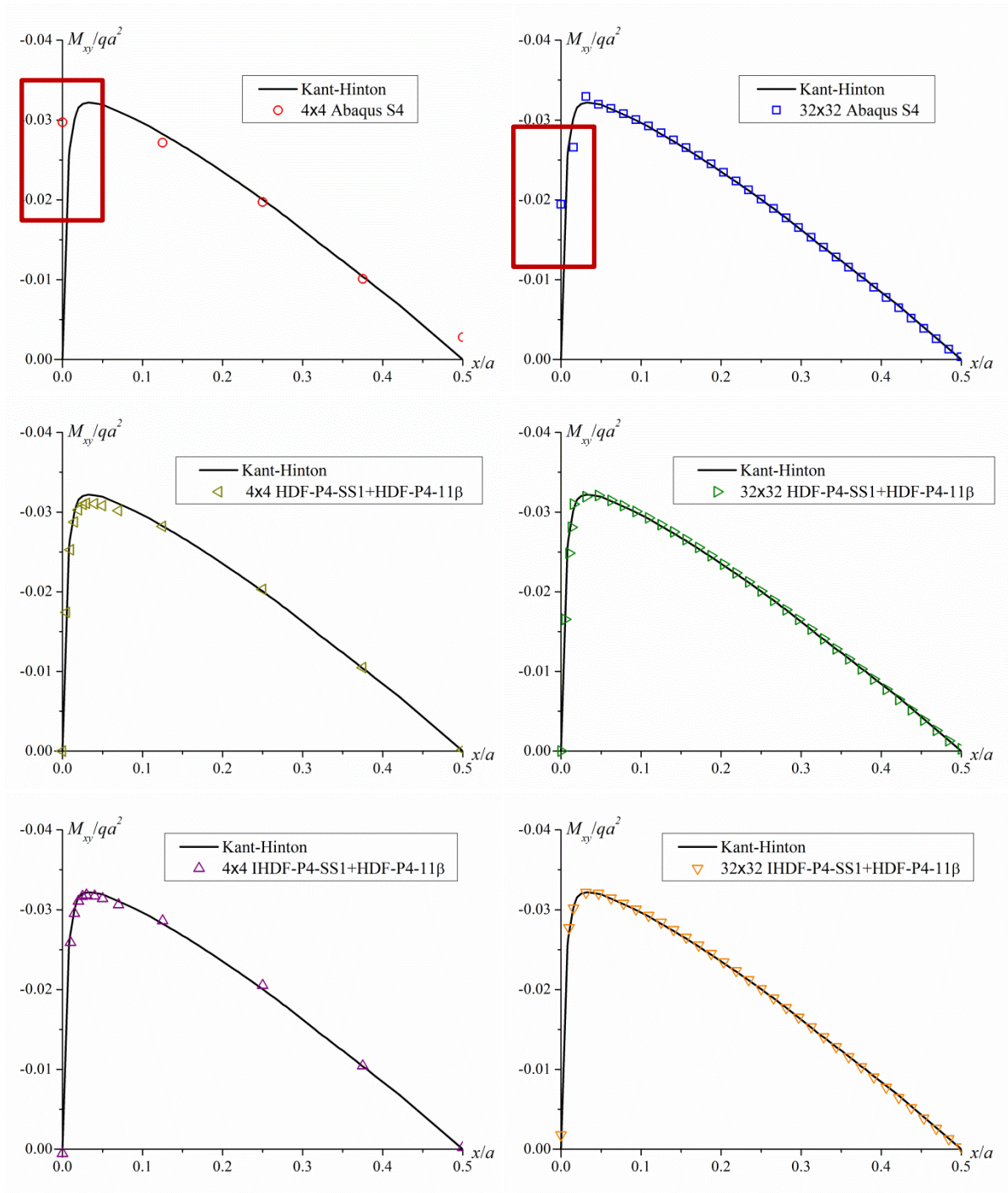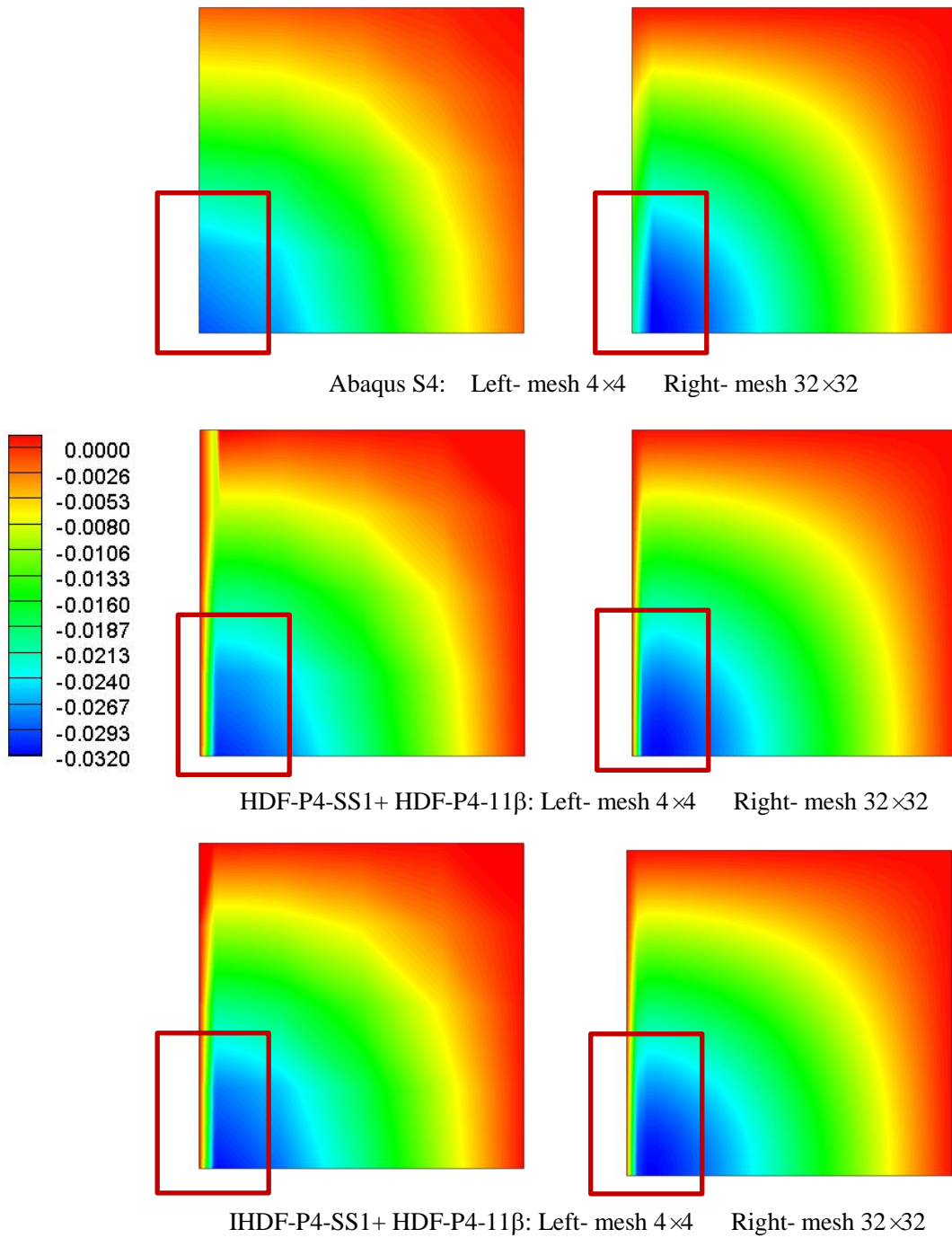
Figure 8. The distribution along the edge AB of shear force T_y/qa for SFSF case with a/h=50, calculated by Abaqus S4 (top), the old scheme (middle) and the present scheme (bottom), in coarse mesh and fine mesh
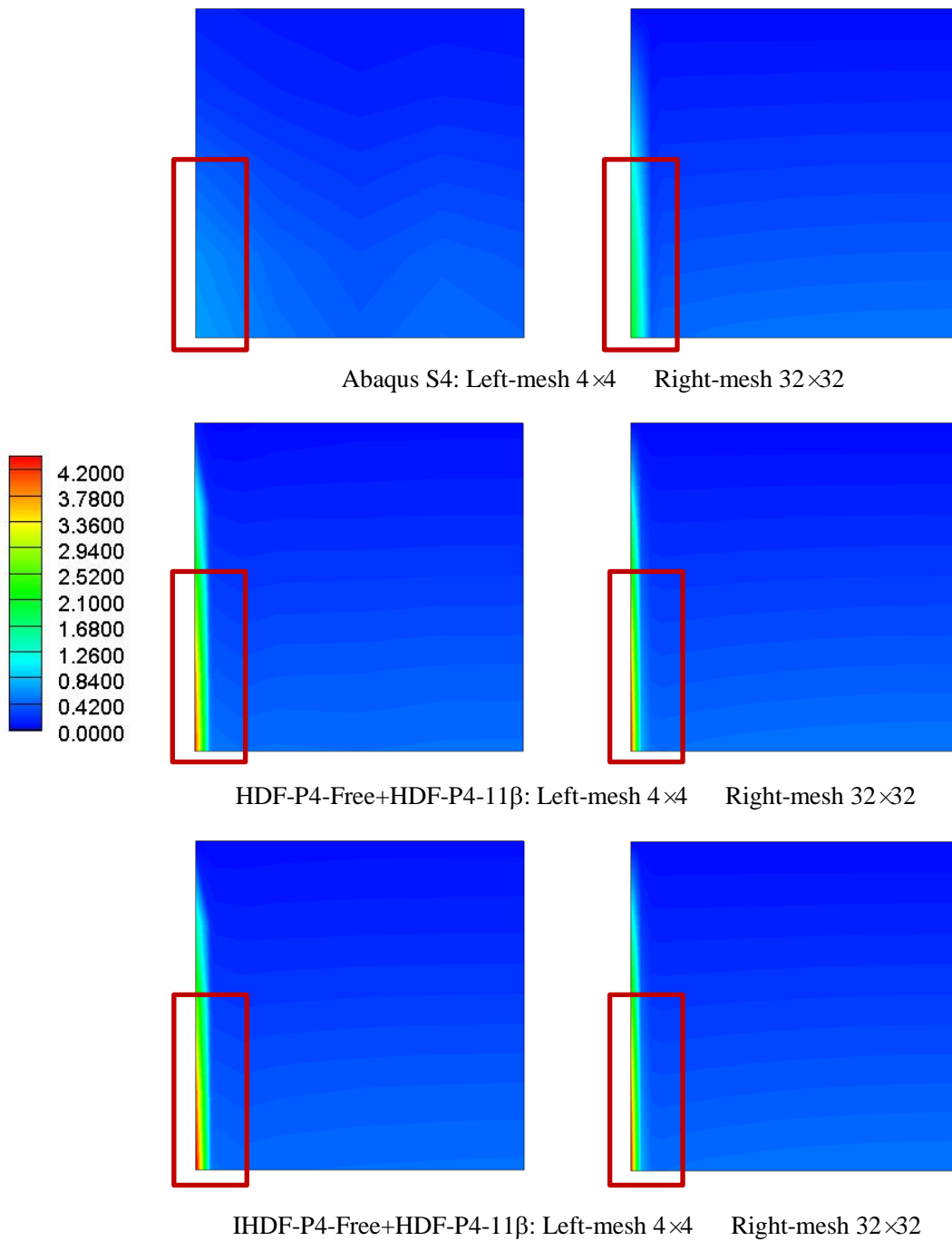
Figure 9. The contour plot of shear force T_y/qa for SFSF case with a/h=50, calculated by Abaqus S4 (top), the old scheme (middle) and the present scheme (bottom), in coarse mesh and fine mesh
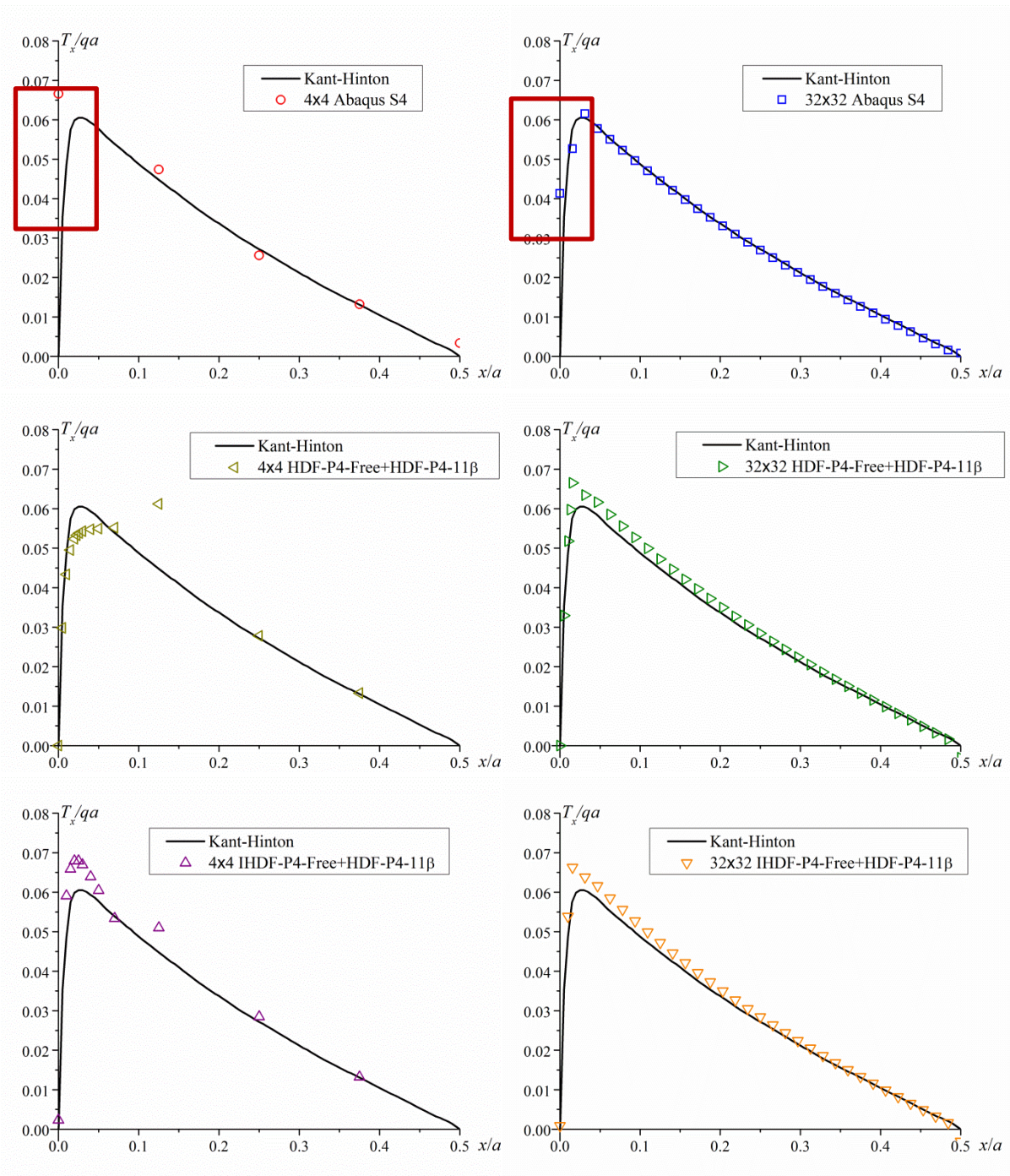
Figure 10. The distribution along the edge DC of shear force T_x/qa for SFSF case with a/h=50, calculated by Abaqus S4 (top), the old scheme (middle) and the present scheme (bottom), in coarse mesh and fine mesh

Abaqus S4: Left-mesh 4×4   Right-mesh 32×32

HDF-P4-Free+HDF-P4-11β: Left- mesh 4×4   Right- mesh 32×32

IHDF-P4-Free+HDF-P4-11β: Left- mesh 4×4   Right- mesh 32×32
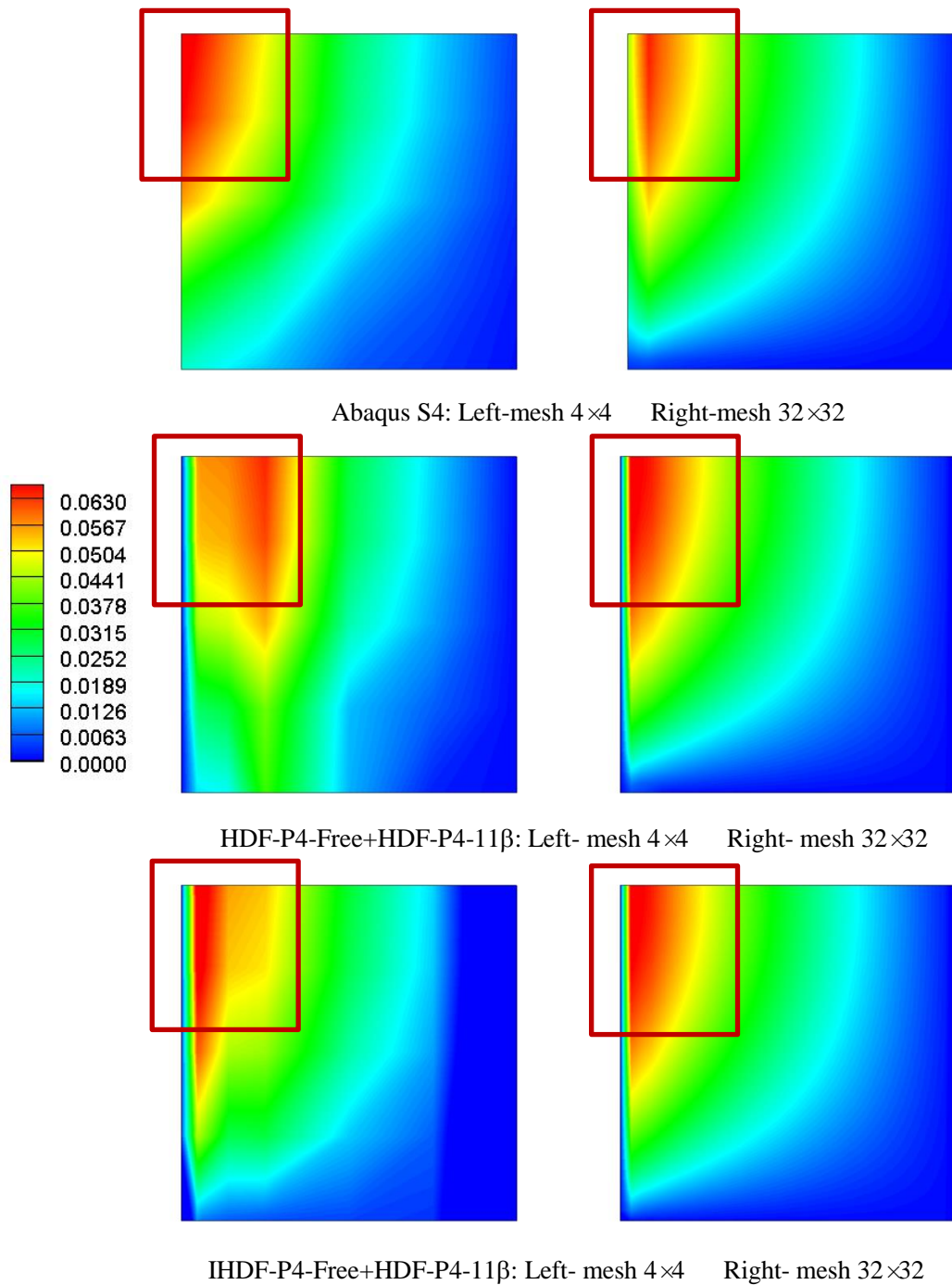
Figure 11. The contour plot of shear force T_x/qa for SFSF case with a/h=50, calculated by Abaqus S4 (top), the old scheme (middle) and the present scheme (bottom), in coarse mesh and fine mesh
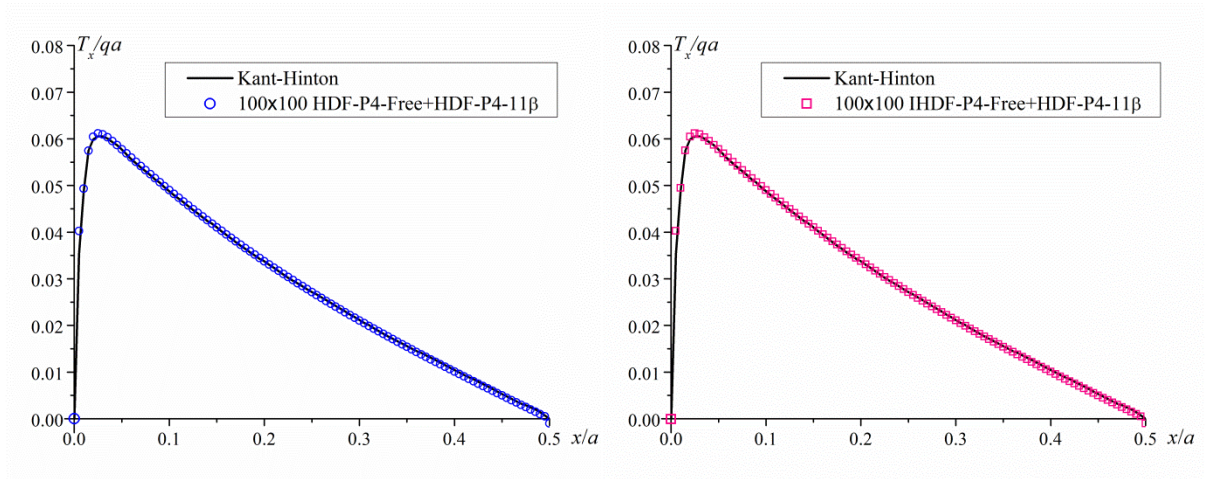
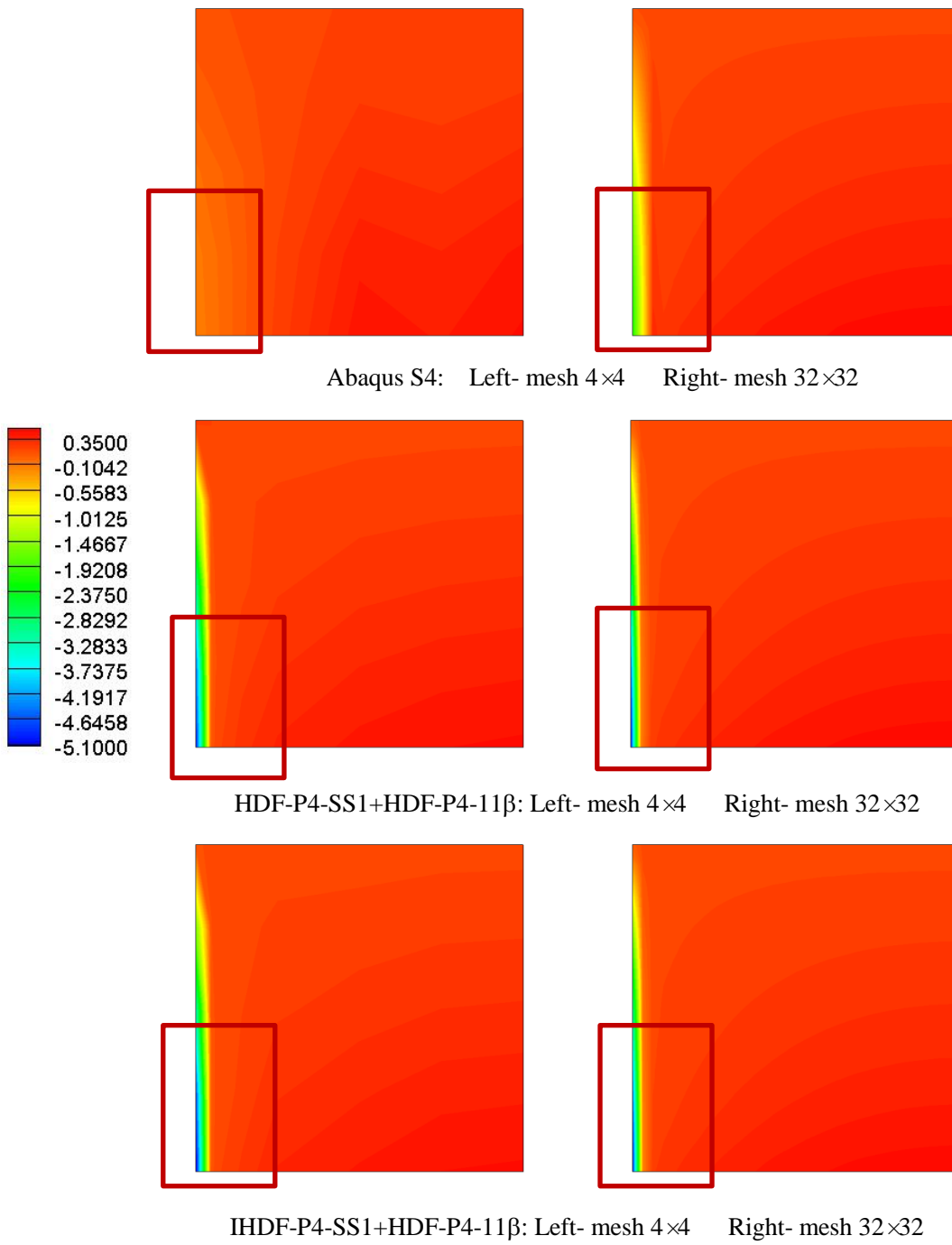Figure 12. The distribution along the edge DC of shear force T_x/qa for SFSF case with a/h=50, calculated by the old scheme (left) and the present scheme (right), in a very fine mesh
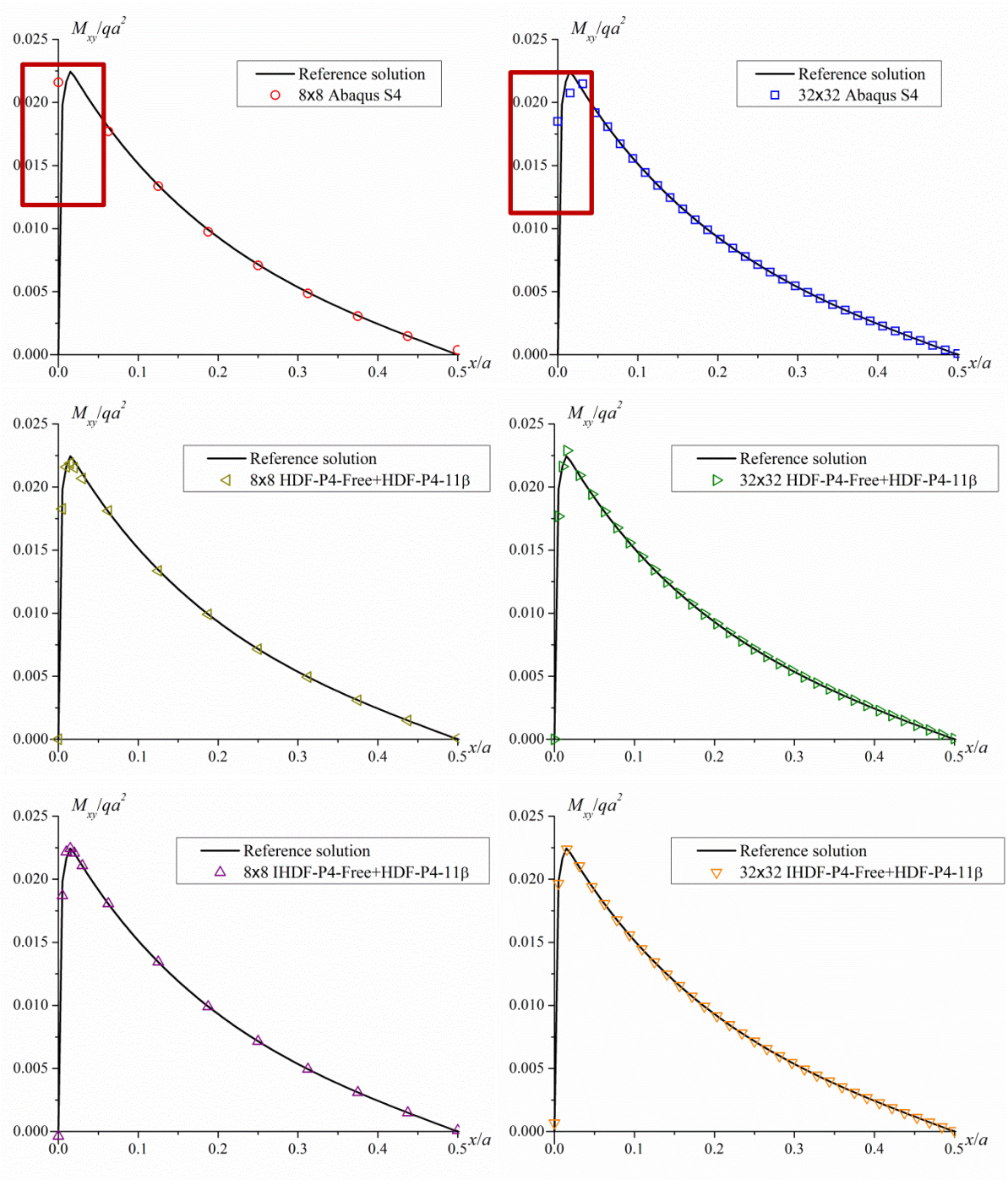
Figure 13. The distribution along the edge AB of twisting moment M_{xy}/qa^2 for SFSF case with a/h=100, calculated by Abaqus S4 (top), the old scheme (middle) and the present scheme (bottom), in coarse mesh and fine mesh

Abaqus S4:   Left-mesh 8×8   Right-mesh 32×32

HDF-P4-Free+HDF-P4-11β: Left-mesh 8×8   Right-mesh 32×32

IHDF-P4-Free+HDF-P4-11β: Left-mesh 8×8   Right-mesh 32×32
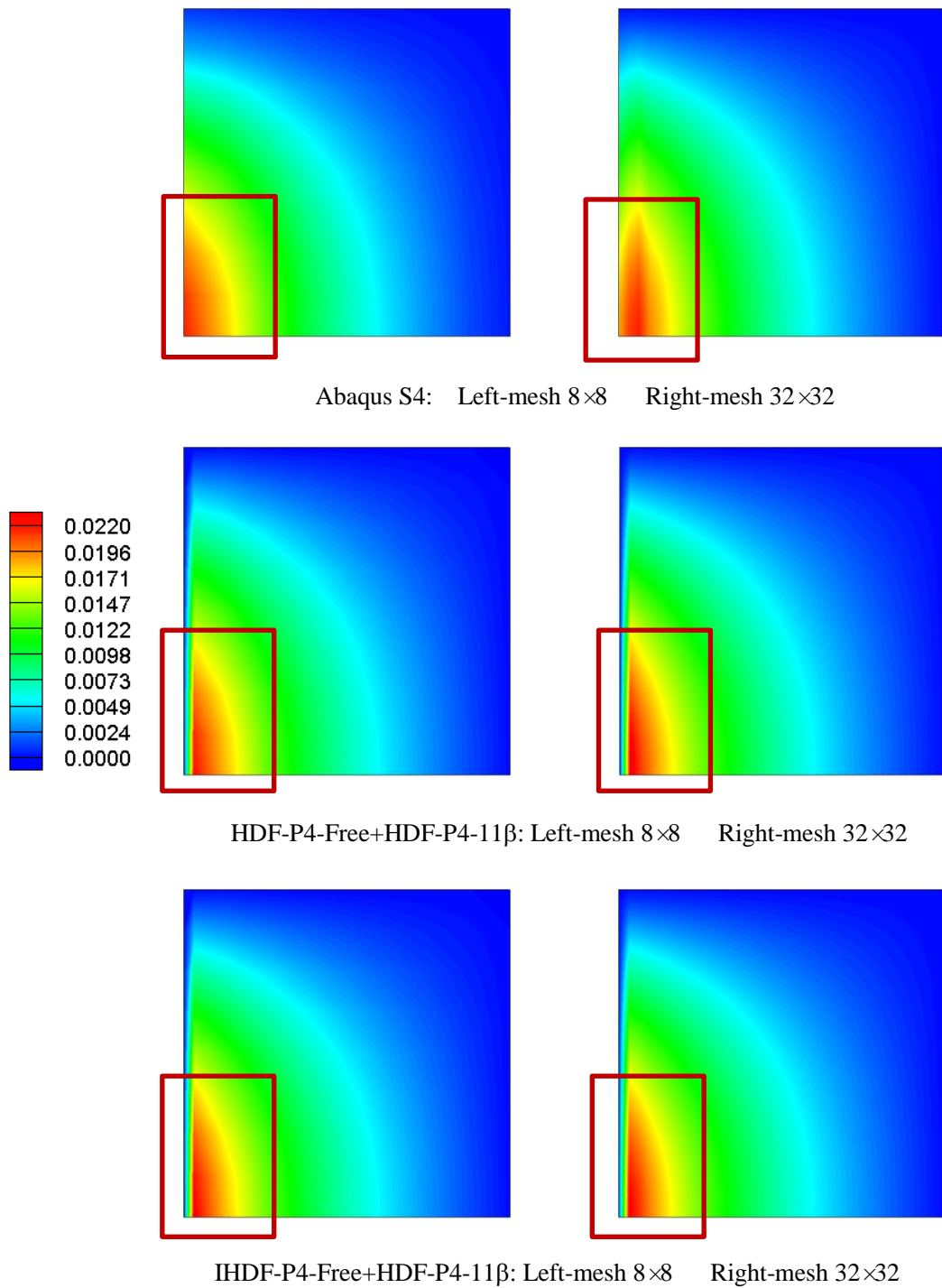
Figure 14. The contour plot of twisting moment M_{xy}/qa^2 for SFSF case with a/h=100, calculated by Abaqus S4 (top), the old scheme (middle) and the present scheme (bottom), in coarse mesh and fine mesh
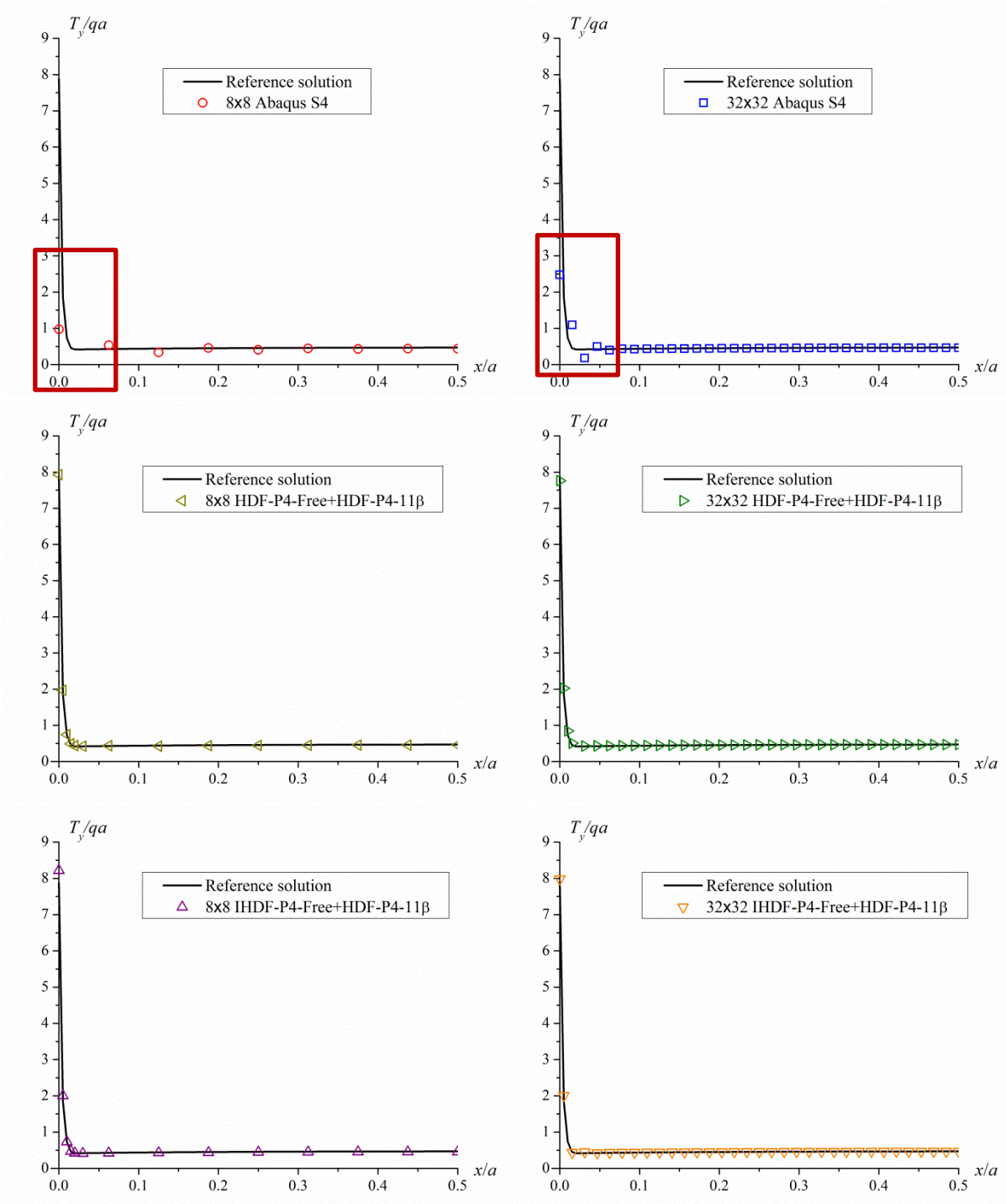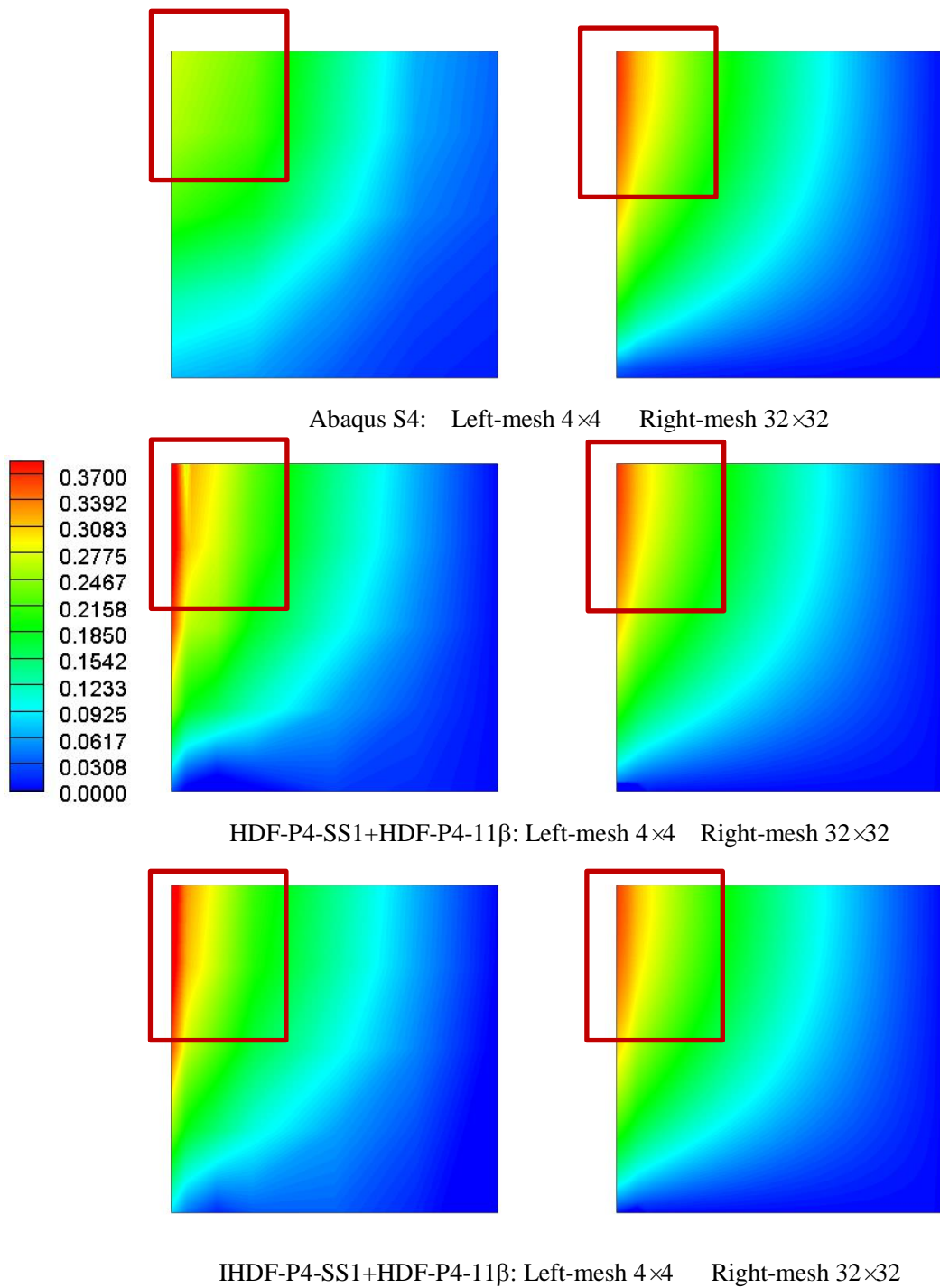
Figure 15. The distribution along the edge AB of shear force T_y/qa for SFSF case with a/h=100, calculated by Abaqus S4 (top), the old scheme (middle) and the present scheme (bottom), in coarse mesh and fine mesh

Abaqus S4: Left-mesh 8×8   Right-mesh 32×32

HDF-P4-Free+HDF-P4-11β: Left-mesh 8×8   Right-mesh 32×32

IHDF-P4-Free+HDF-P4-11β: Left-mesh 8×8   Right-mesh 32×32
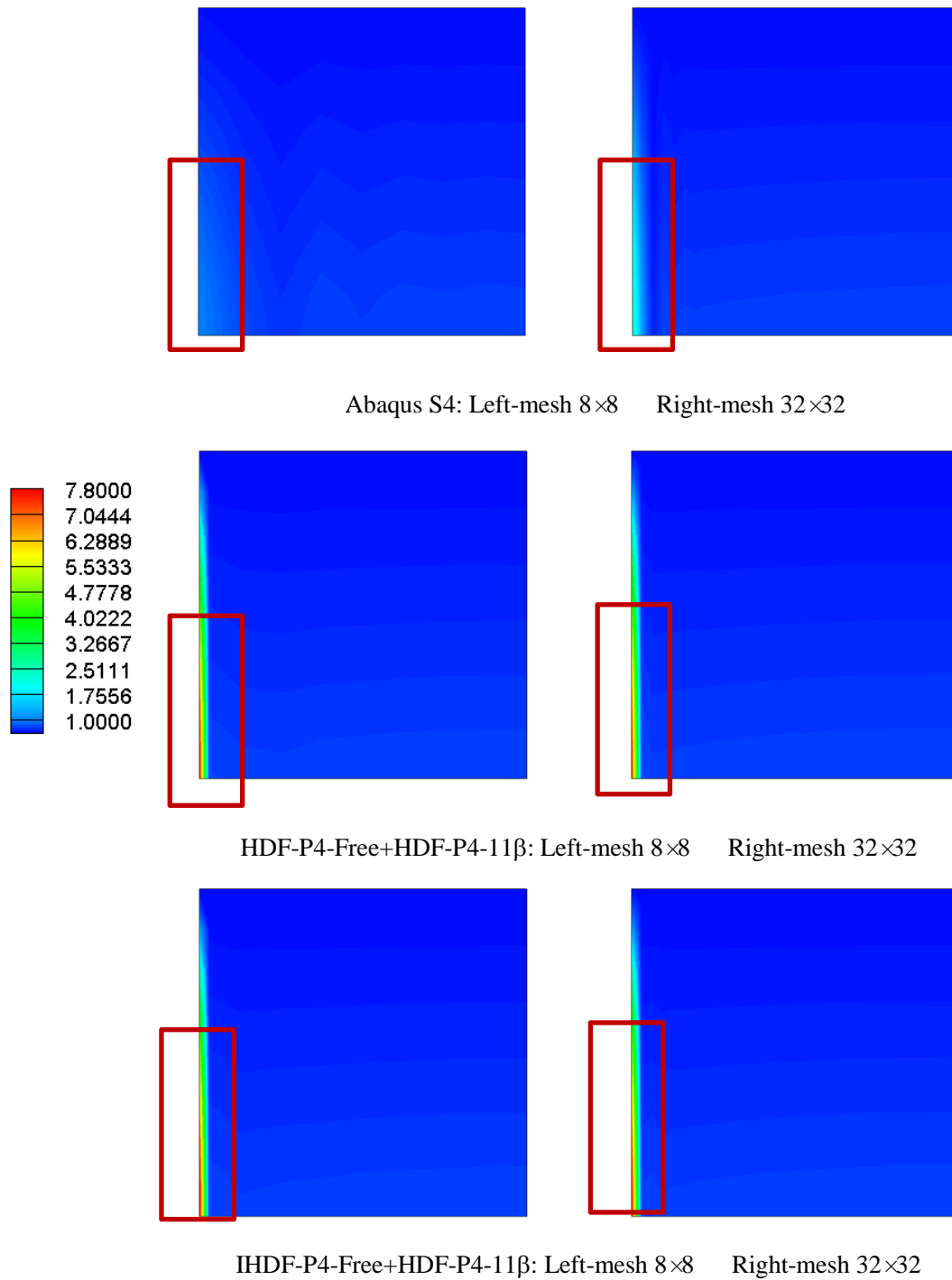
Figure 16. The contour plot of shear force T_y/qa for SFSF case with a/h=100, calculated by Abaqus S4 (top), the old scheme (middle) and the present scheme (bottom), in coarse mesh and fine mesh
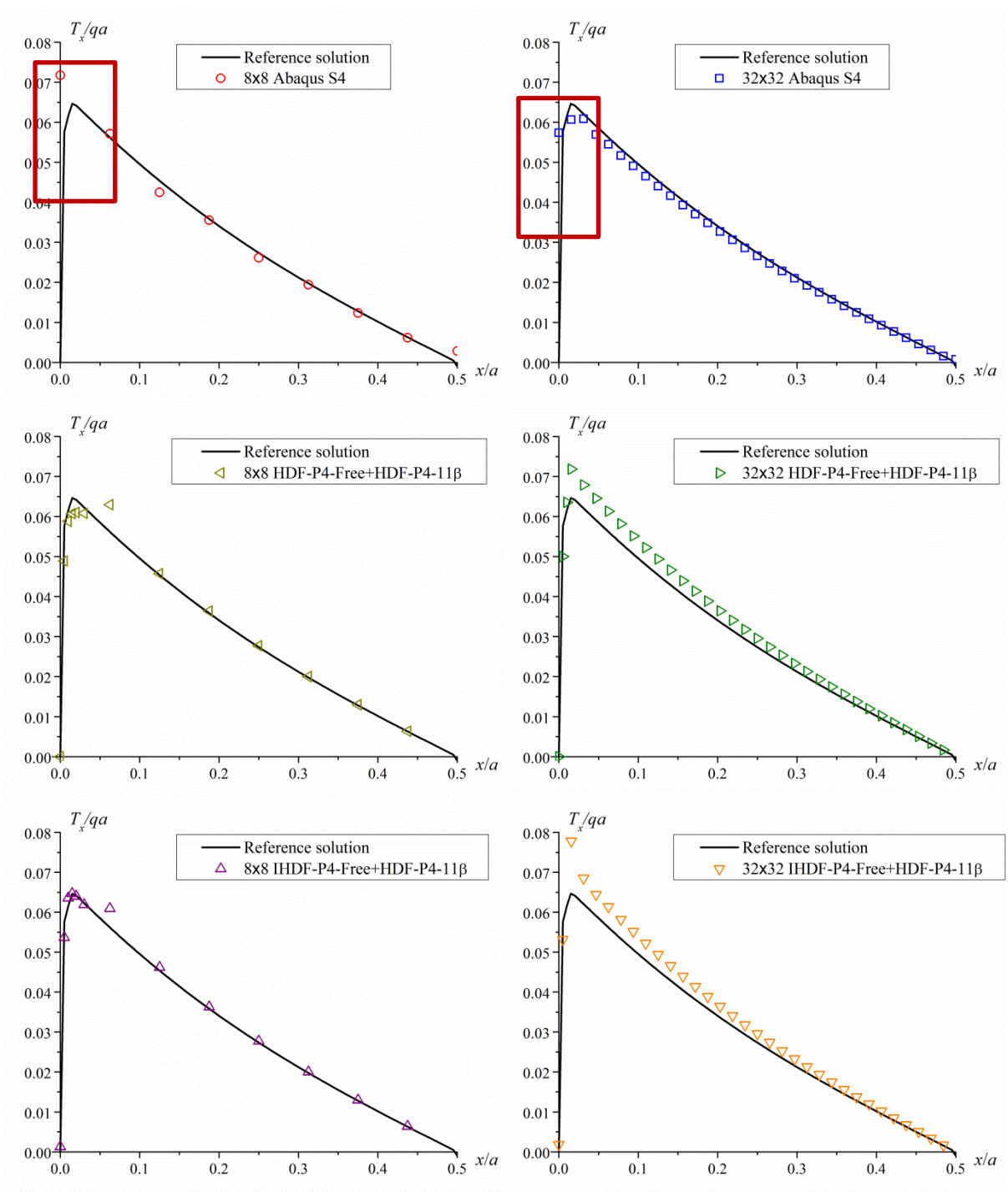
Figure 17. The distribution along the edge DC of shear force T_x/qa for SFSF case with a/h=100, calculated by Abaqus S4 (top), the old scheme (middle) and the present scheme (bottom), in coarse mesh and fine mesh
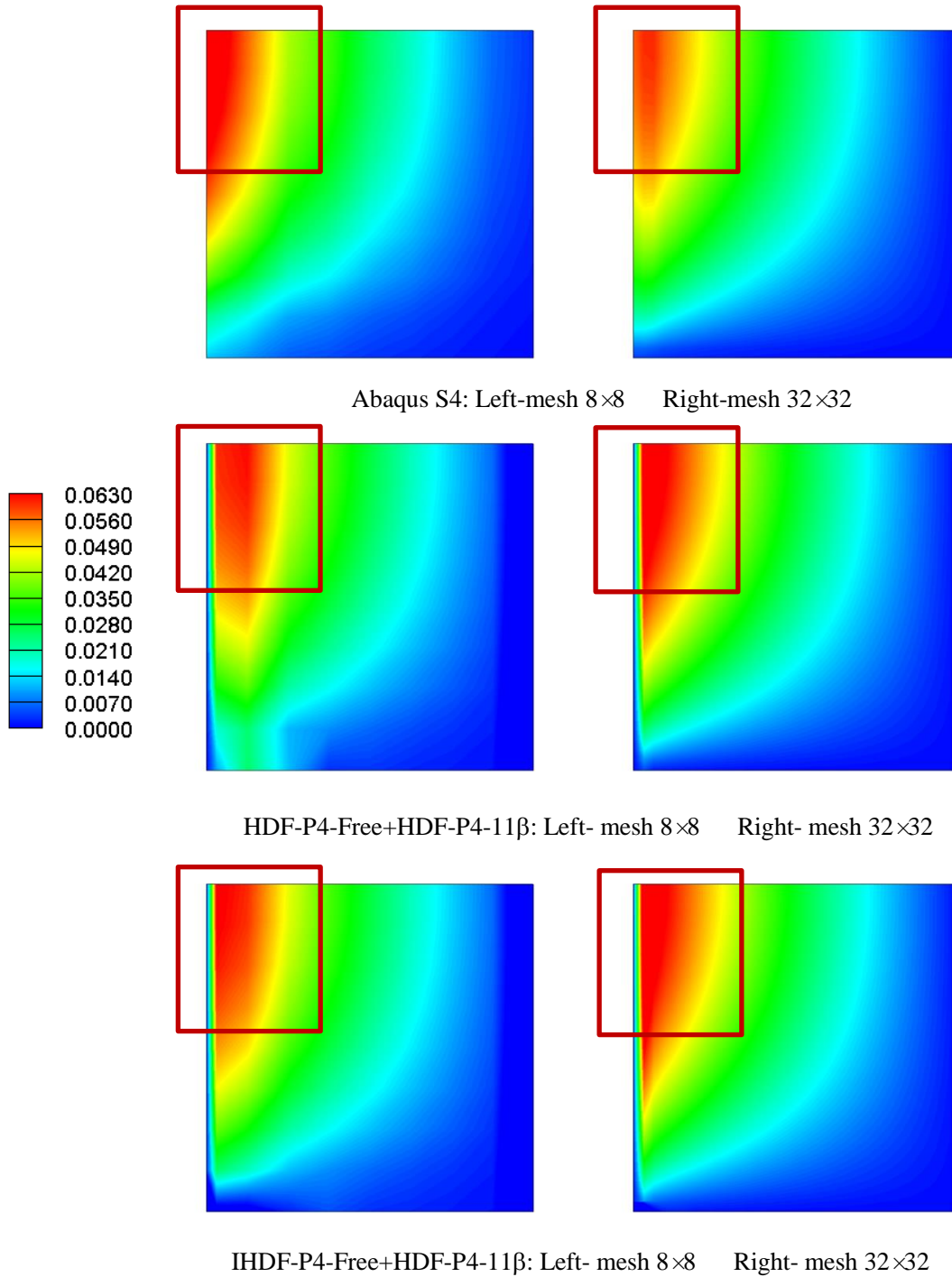
Figure 18. The contour plot of shear force T_x/qa for SFSF case with a/h=100, calculated by Abaqus S4 (top), the old scheme (middle) and the present scheme (bottom), in coarse mesh and fine mesh
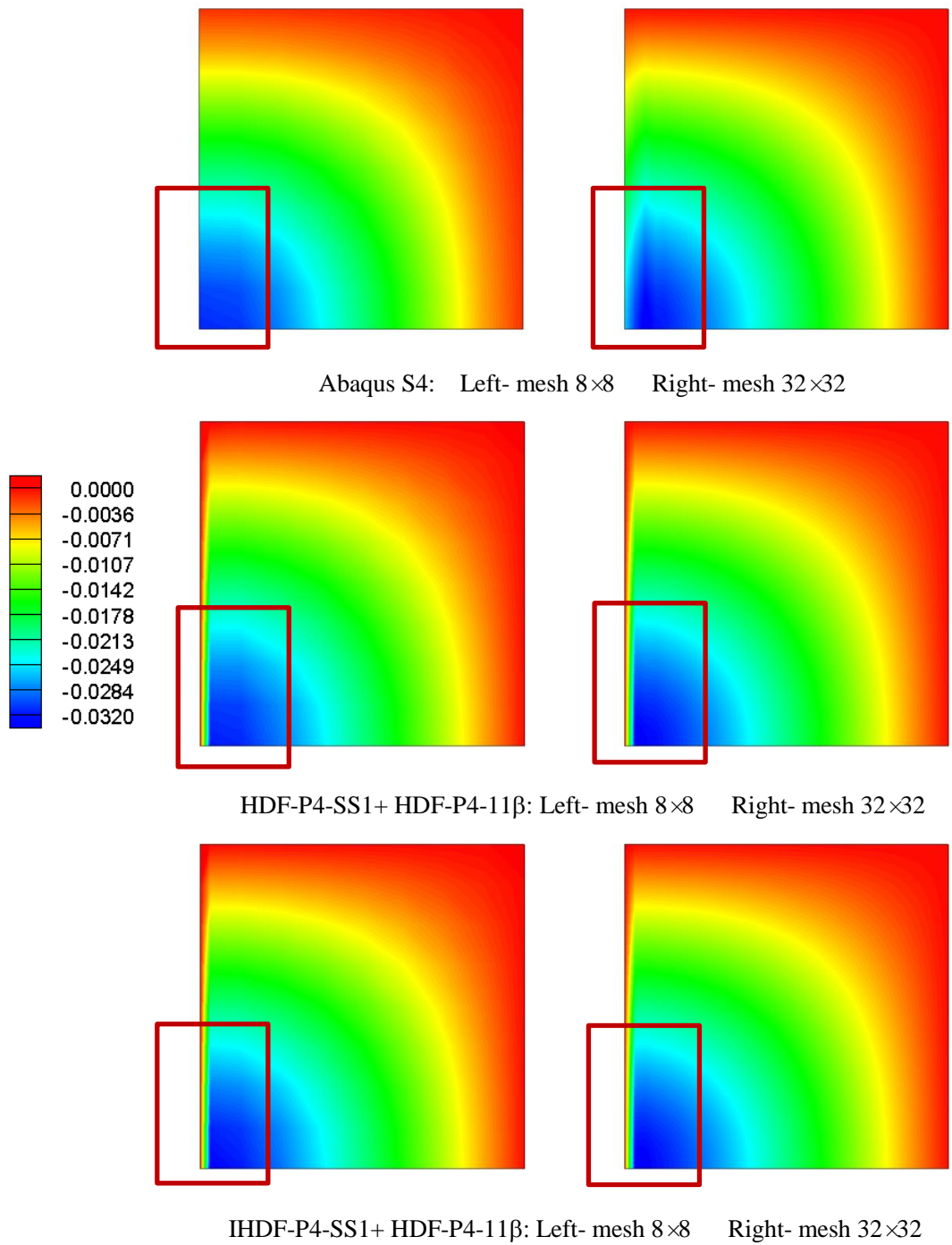
Figure 19. The distribution along the edge AB of twisting moment M_{xy}/qa^2 for SS*SS* case with a/h=50, calculated by Abaqus S4 (top), the old scheme (middle) and the present scheme (bottom), in coarse mesh and fine mesh

Abaqus S4:   Left- mesh 4×4   Right- mesh 32×32

HDF-P4-SS1+ HDF-P4-11β: Left- mesh 4×4   Right- mesh 32×32

IHDF-P4-SS1+ HDF-P4-11β: Left- mesh 4×4   Right- mesh 32×32

Figure 20. The contour plot of twisting moment M_{xy}/qa^2 for SS*SS* case with a/h=50, calculated by Abaqus S4 (top), the old scheme (middle) and the present scheme (bottom), in coarse mesh and fine mesh
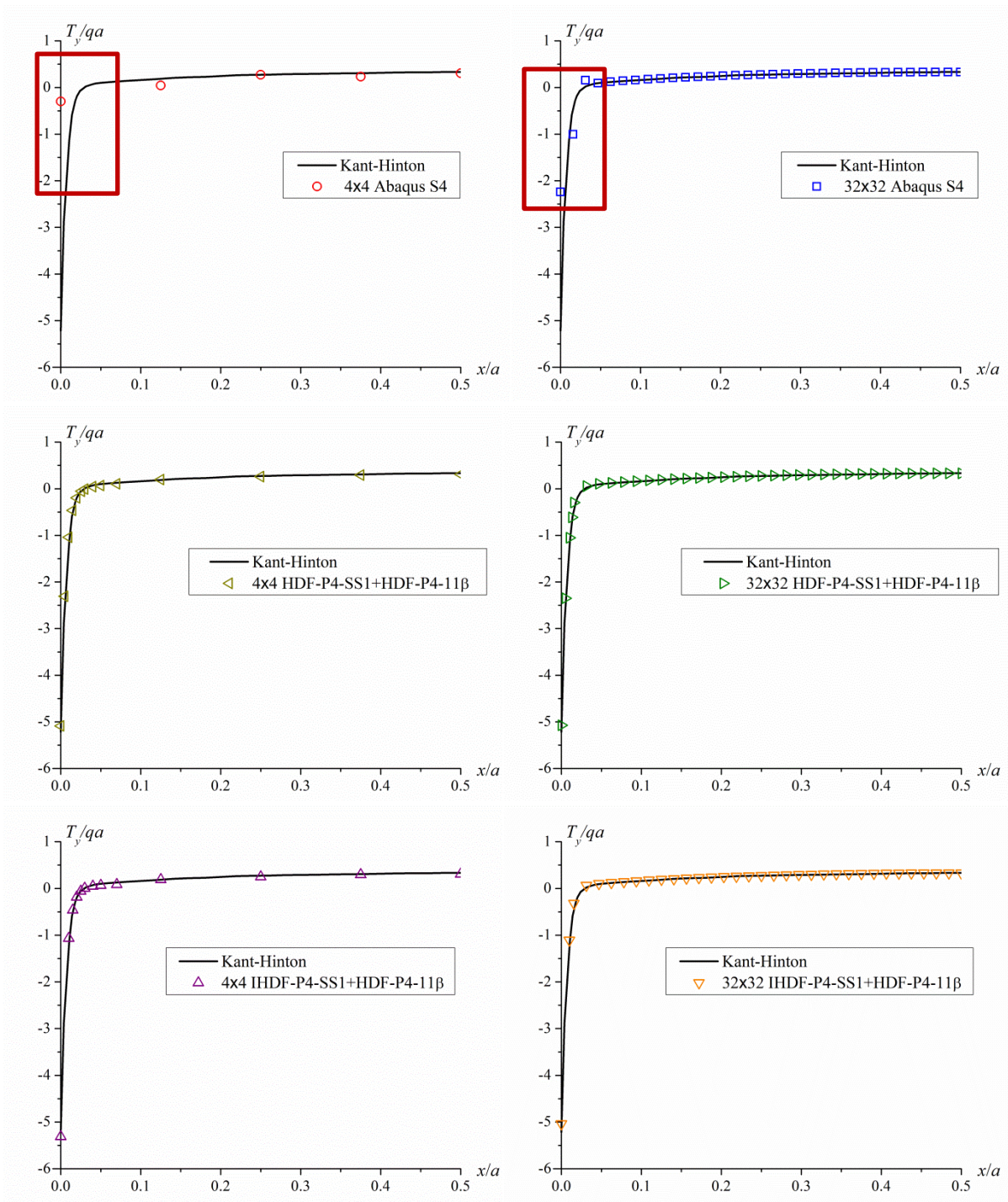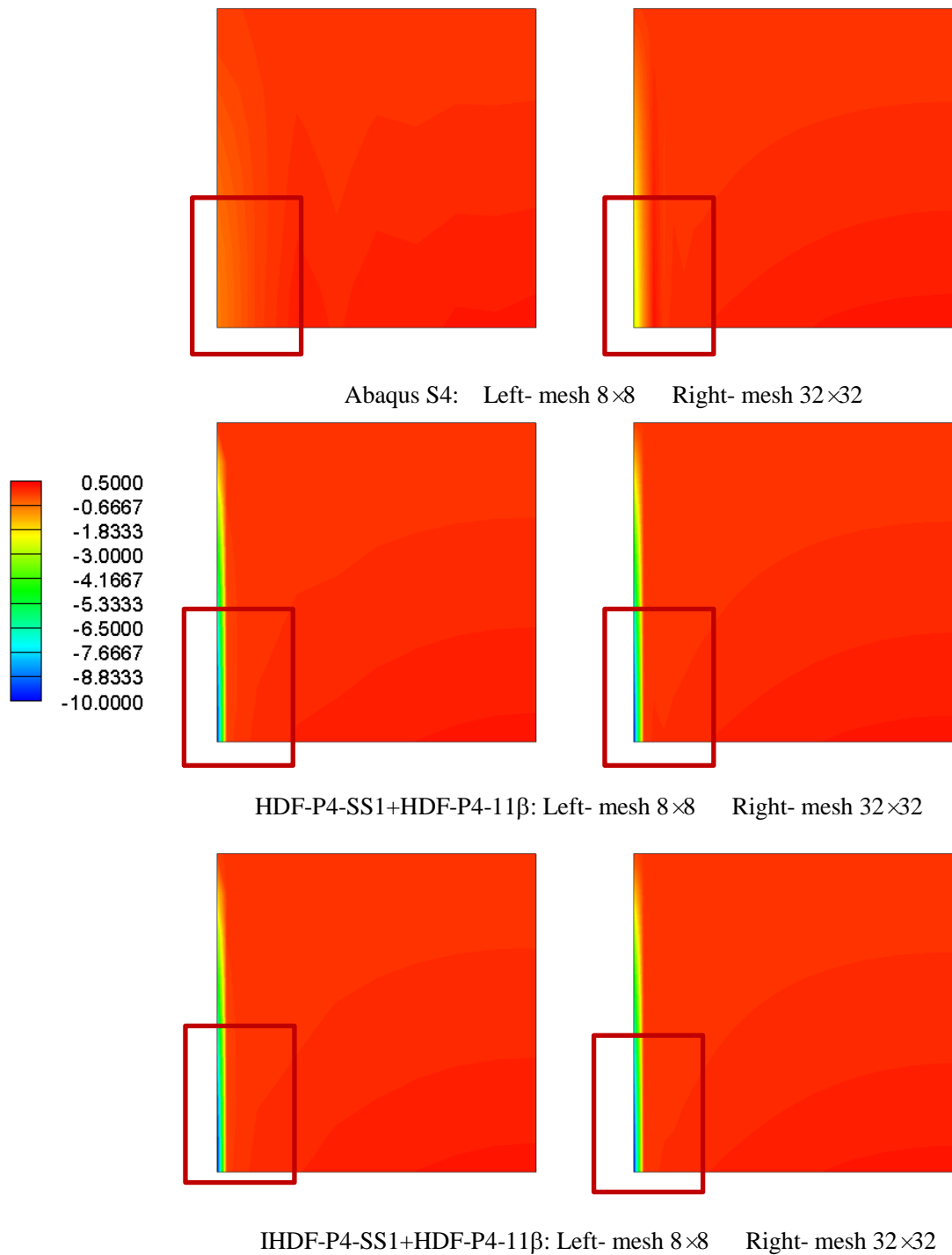
Figure 21. The distribution along the edge AB of shear force T_y/qa for SS*SS* case with a/h=50, calculated by Abaqus S4 (top), the old scheme (middle) and the present scheme (bottom), in coarse mesh and fine mesh

Color scale values:
0.3500
-0.1042
-0.5583
-1.0125
-1.4667
-1.9208
-2.3750
-2.8292
-3.2833
-3.7375
-4.1917
-4.6458
-5.1000

Abaqus S4:   Left- mesh 4×4   Right- mesh 32×32

HDF-P4-SS1+HDF-P4-11β: Left- mesh 4×4   Right- mesh 32×32

IHDF-P4-SS1+HDF-P4-11β: Left- mesh 4×4   Right- mesh 32×32

Figure 22. The contour plot of shear force T_y/qa for SS*SS* case with a/h=50, calculated by Abaqus S4 (top), the old scheme (middle) and the present scheme (bottom), in coarse mesh and fine mesh
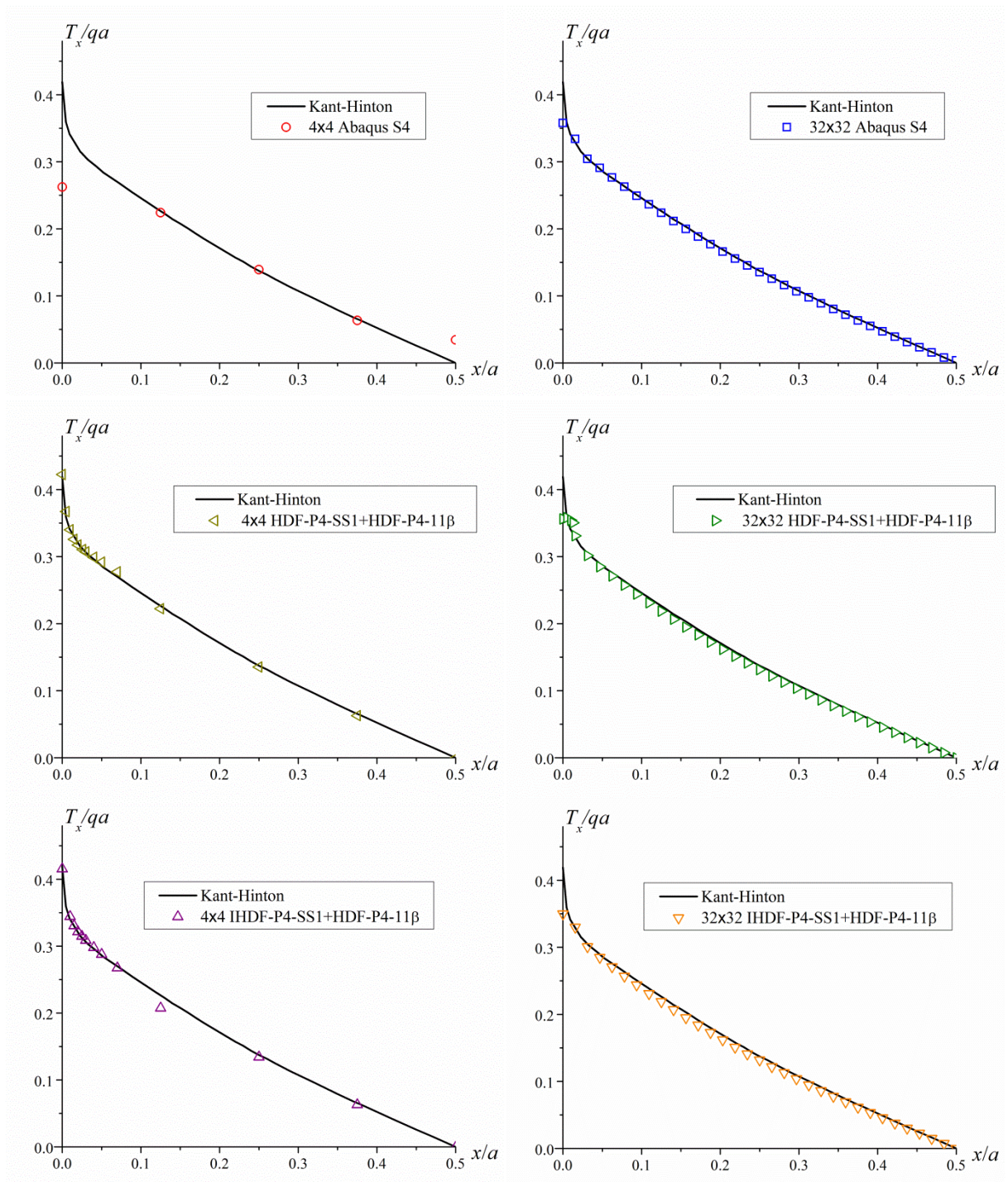
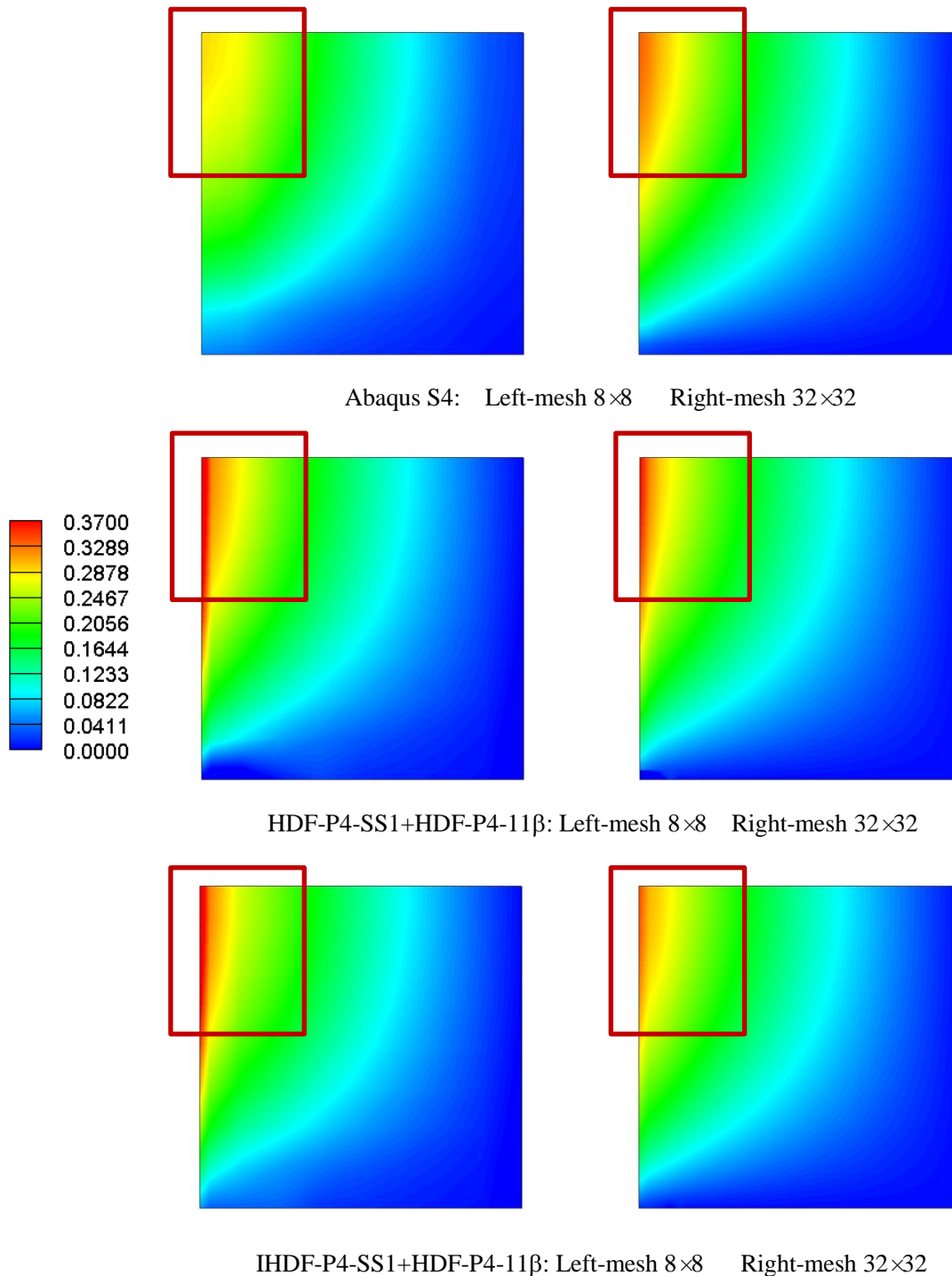Figure 23. The distribution along the edge DC of shear force T_x/qa for SS*SS* case with a/h=50, calculated by Abaqus S4 (top), the old scheme (middle) and the present scheme (bottom), in coarse mesh and fine mesh

Abaqus S4:   Left-mesh 4×4   Right-mesh 32×32

HDF-P4-SS1+HDF-P4-11β: Left-mesh 4×4   Right-mesh 32×32

IHDF-P4-SS1+HDF-P4-11β: Left-mesh 4×4   Right-mesh 32×32

Figure 24. The contour plot of shear force T_x/qa for SS*SS* case with a/h=50, calculated by Abaqus S4 (top), the old scheme (middle) and the present scheme (bottom), in coarse mesh and fine mesh
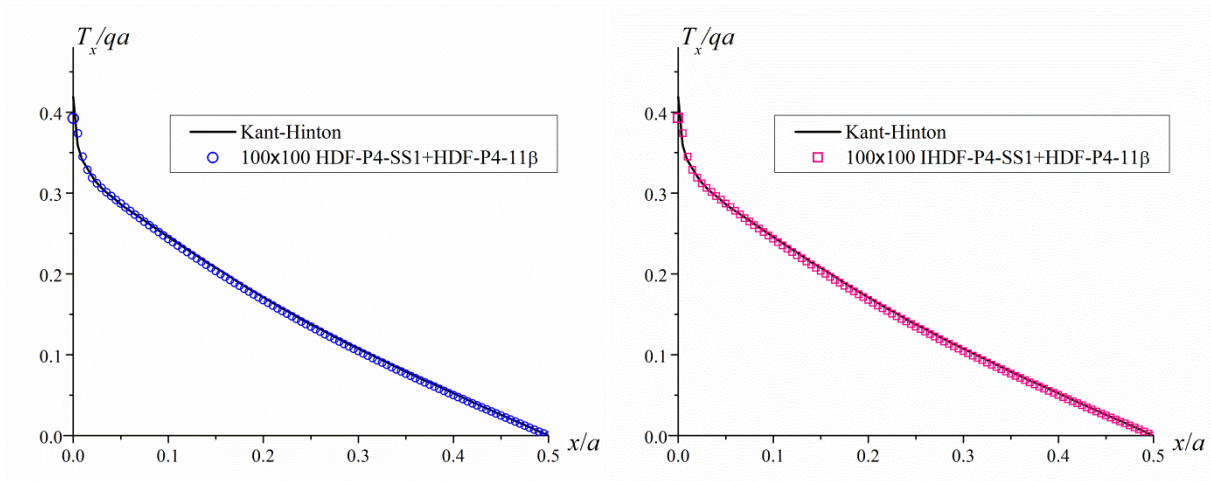
Figure 25. The distribution along the edge DC of shear force T_x/qa for SS*SS* case with a/h=50, calculated by the old scheme (left) and the present scheme (right), in a very fine mesh
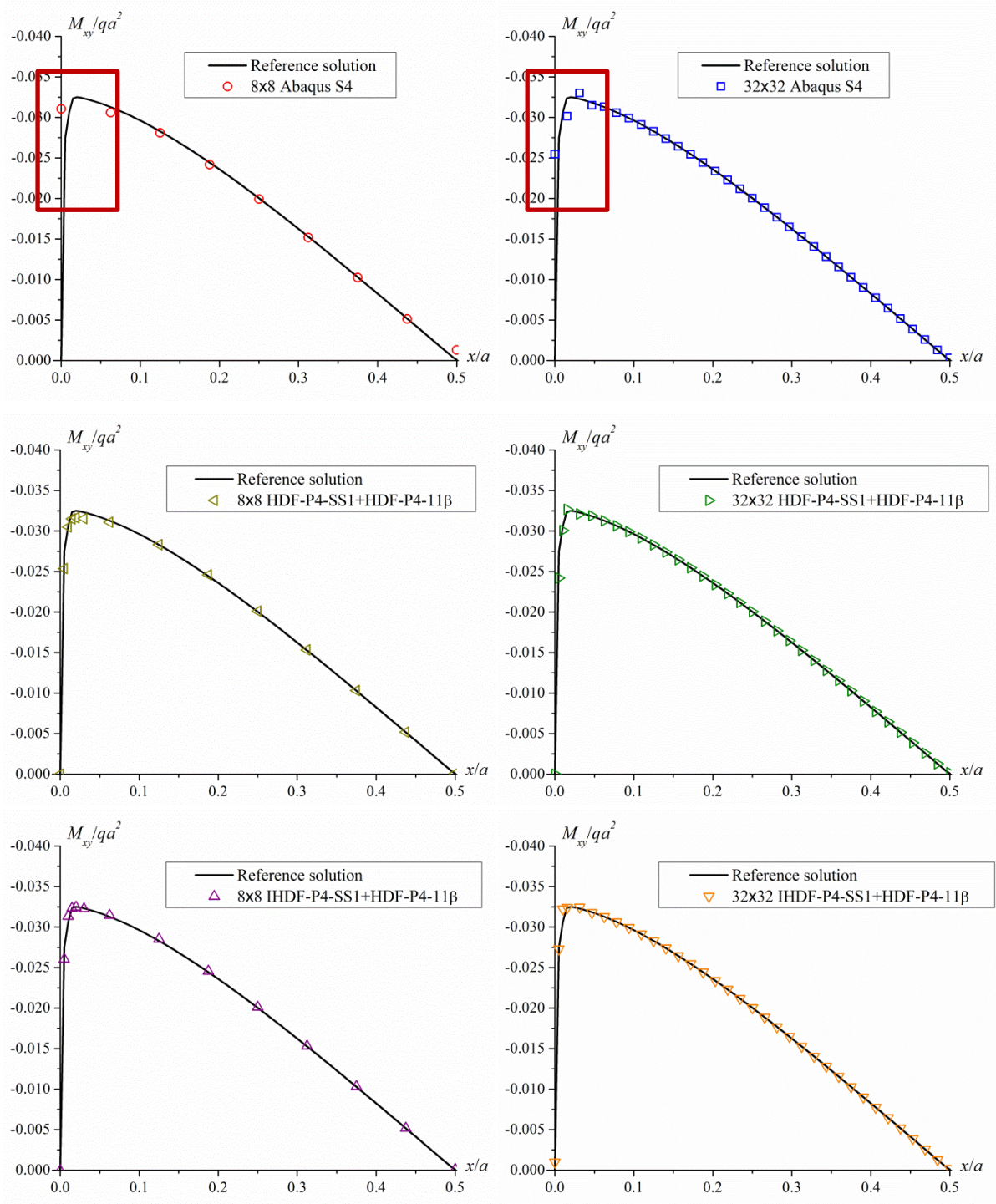
Figure 26. The distribution along the edge AB of twisting moment M_{xy}/qa^2 for SS^*SS^* case with a/h=100, calculated by Abaqus S4 (top), the old scheme (middle) and the present scheme (bottom), in coarse mesh and fine mesh

Abaqus S4:   Left- mesh 8×8   Right- mesh 32×32

HDF-P4-SS1+ HDF-P4-11β: Left- mesh 8×8   Right- mesh 32×32

IHDF-P4-SS1+ HDF-P4-11β: Left- mesh 8×8   Right- mesh 32×32

Figure 27. The contour plot of twisting moment M_{xy}/qa^2 for SS*SS* case with a/h=100, calculated by Abaqus S4 (top), the old scheme (middle) and the present scheme (bottom), in coarse mesh and fine mesh
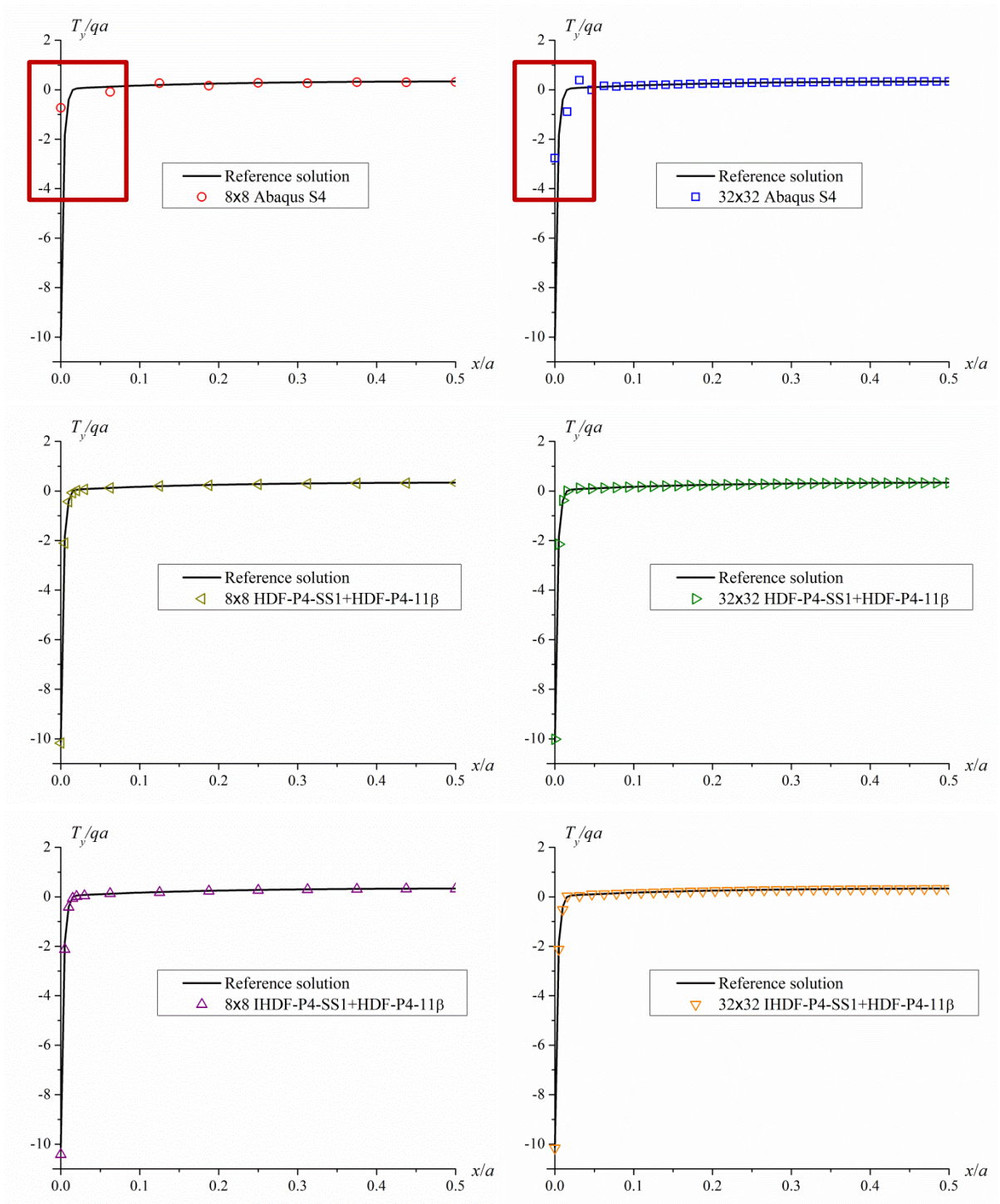
Figure 28. The distribution along the edge AB of shear force T_y/qa for SS*SS* case with a/h=100, calculated by Abaqus S4 (top), the old scheme (middle) and the present scheme (bottom), in coarse mesh and fine mesh

Abaqus S4:   Left- mesh 8×8   Right- mesh 32×32

HDF-P4-SS1+HDF-P4-11β: Left- mesh 8×8   Right- mesh 32×32

IHDF-P4-SS1+HDF-P4-11β: Left- mesh 8×8   Right- mesh 32×32

Figure 29. The contour plot of shear force T_y/qa for SS*SS* case with a/h=100, calculated by Abaqus S4 (top), the old scheme (middle) and the present scheme (bottom), in coarse mesh and fine mesh
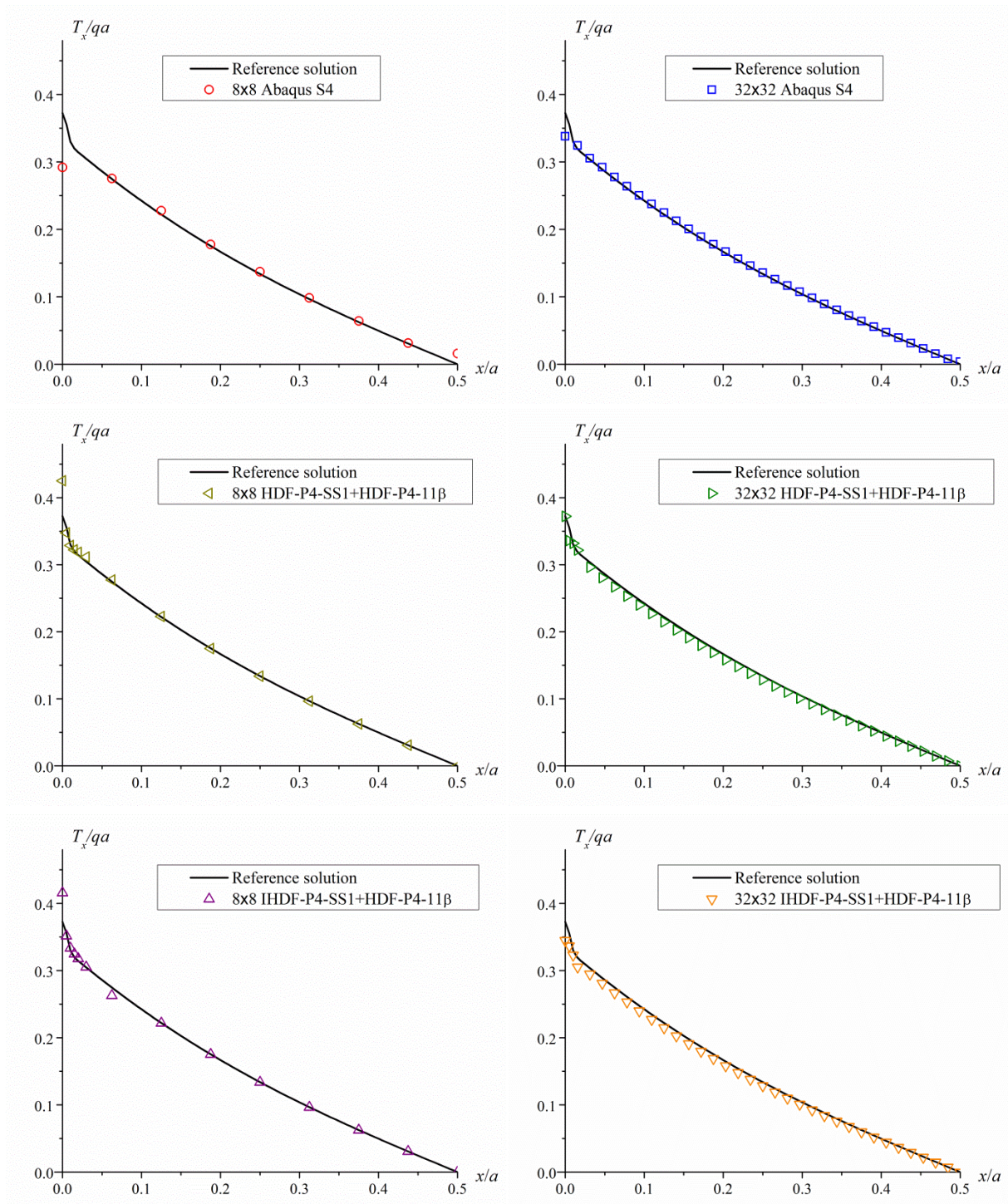
Figure 30. The distribution along the edge DC of shear force T_x/qa for SS*SS* case with a/h=100, calculated by Abaqus S4 (top), the old scheme (middle) and the present scheme (bottom), in coarse mesh and fine mesh

Abaqus S4:   Left-mesh 8×8   Right-mesh 32×32

HDF-P4-SS1+HDF-P4-11β: Left-mesh 8×8   Right-mesh 32×32

IHDF-P4-SS1+HDF-P4-11β: Left-mesh 8×8   Right-mesh 32×32

Figure 31. The contour plot of shear force T_x/qa for SS*SS* case with a/h=100, calculated by Abaqus S4 (top), the old scheme (middle) and the present scheme (bottom), in coarse mesh and fine mesh

(a) regular mesh   (b) distorted mesh

Special IHDF elements   Conventional HDF elements
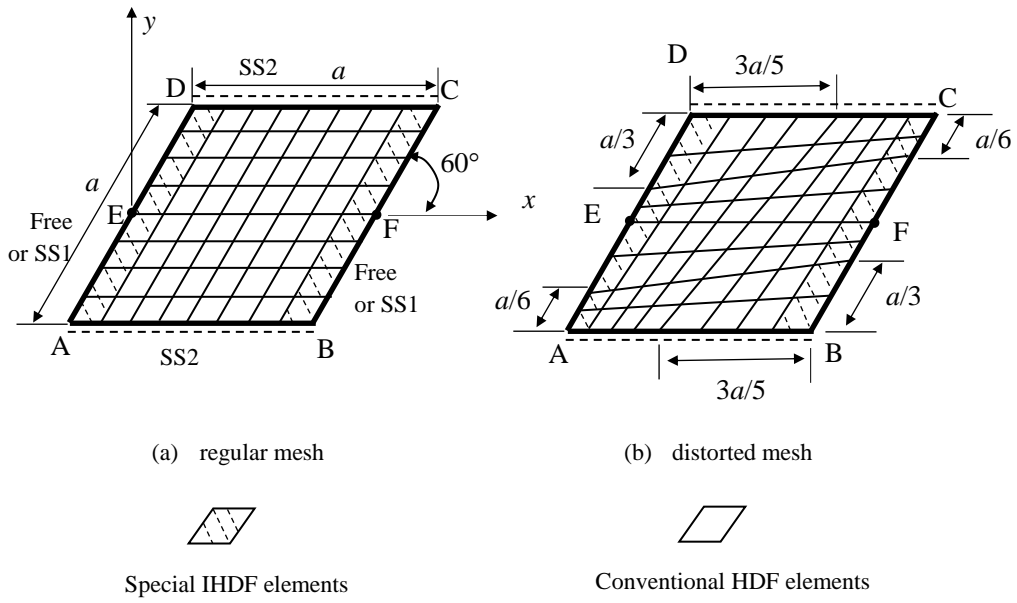
Figure 32. The 60° skew plate with two opposite edges hard simply-supported
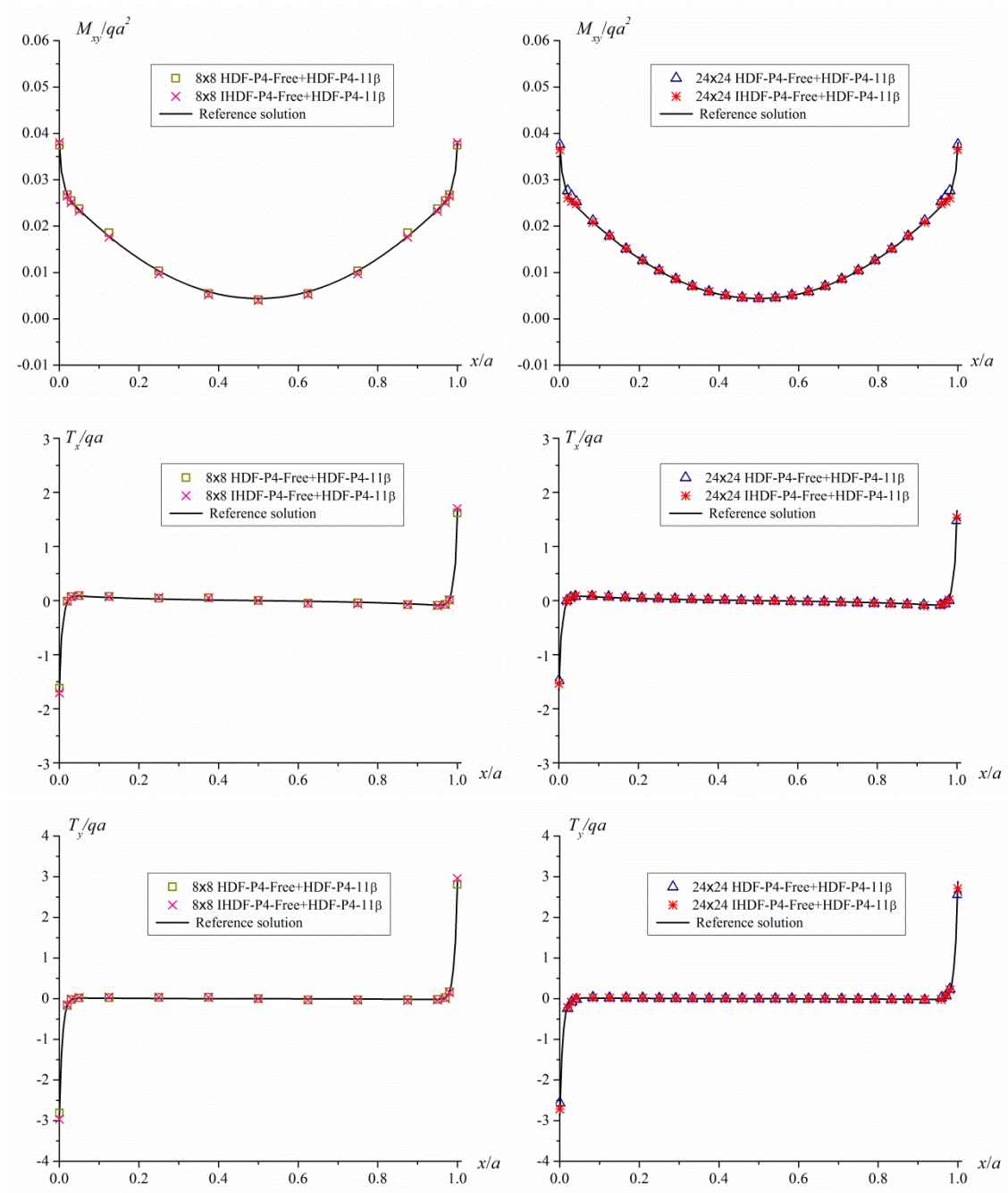and the typical meshes
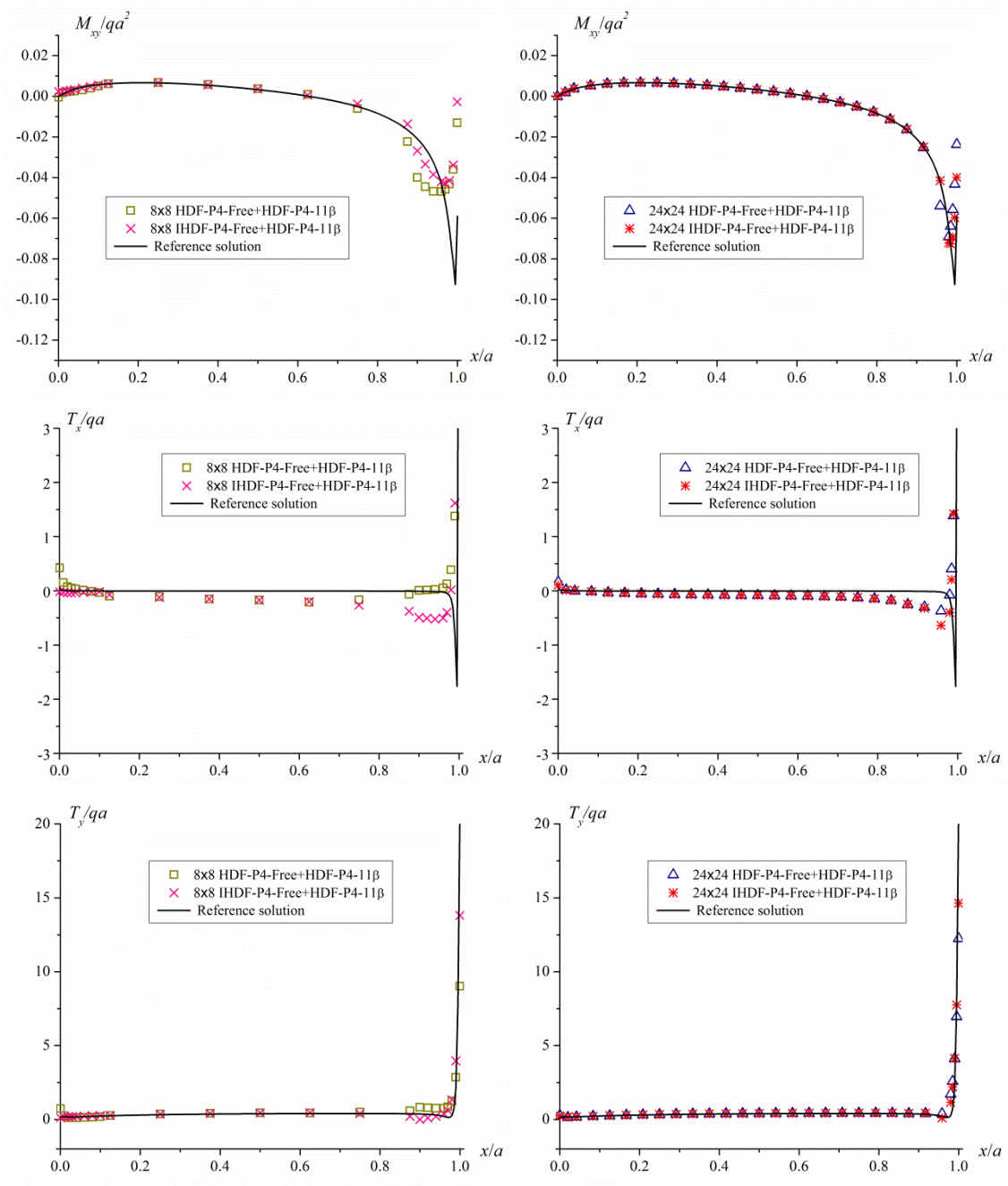
Figure 33. Distributions of twist moment M_{xy}, shear forces T_x and T_y along the path AB of the 60° skew plate in regular mesh (SFSF case)
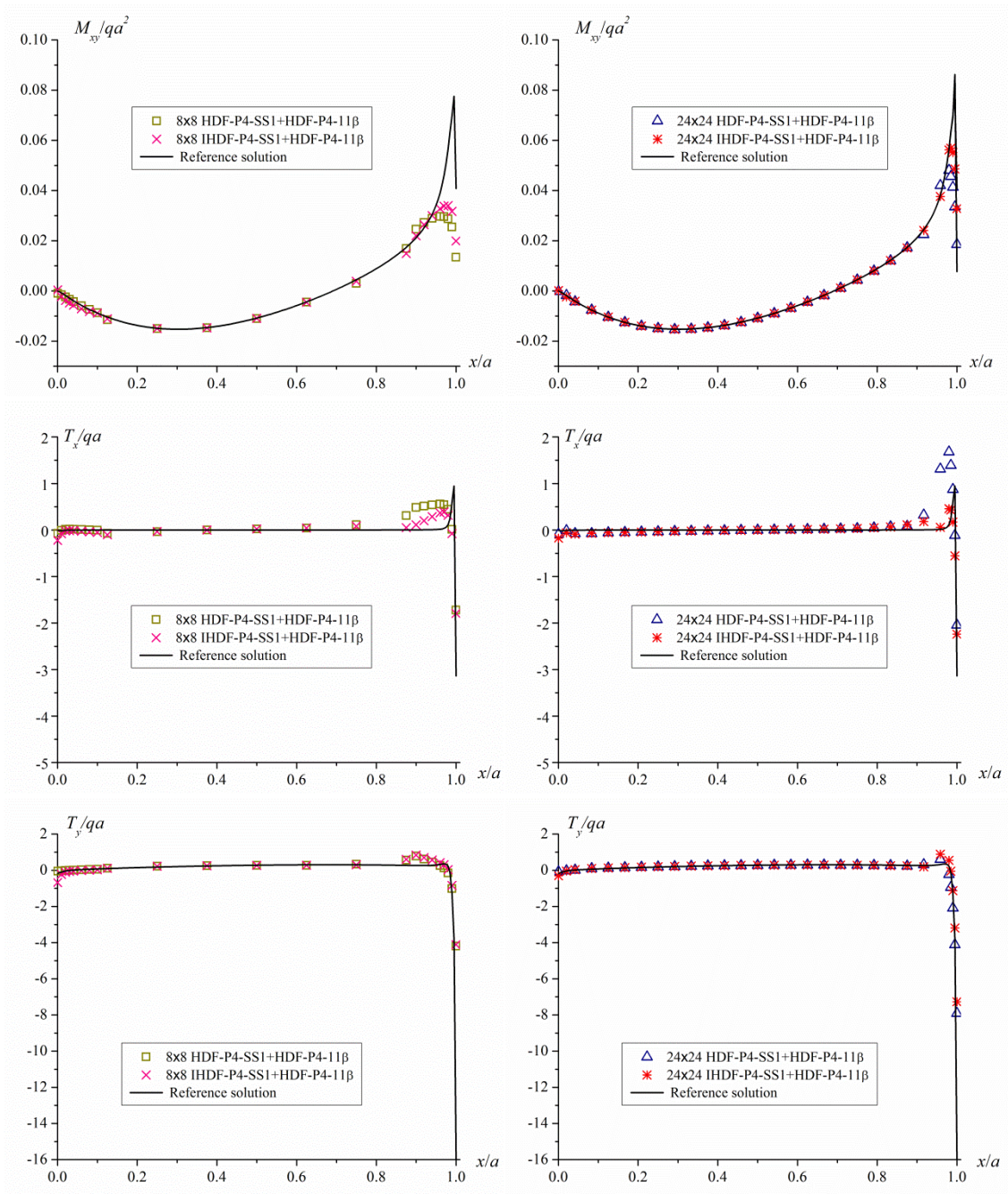
Figure 34. Distributions of twist moment M_{xy}, shear forces T_x and T_y along the path AB of the 60° skew plate in regular mesh (SS*SS* case)
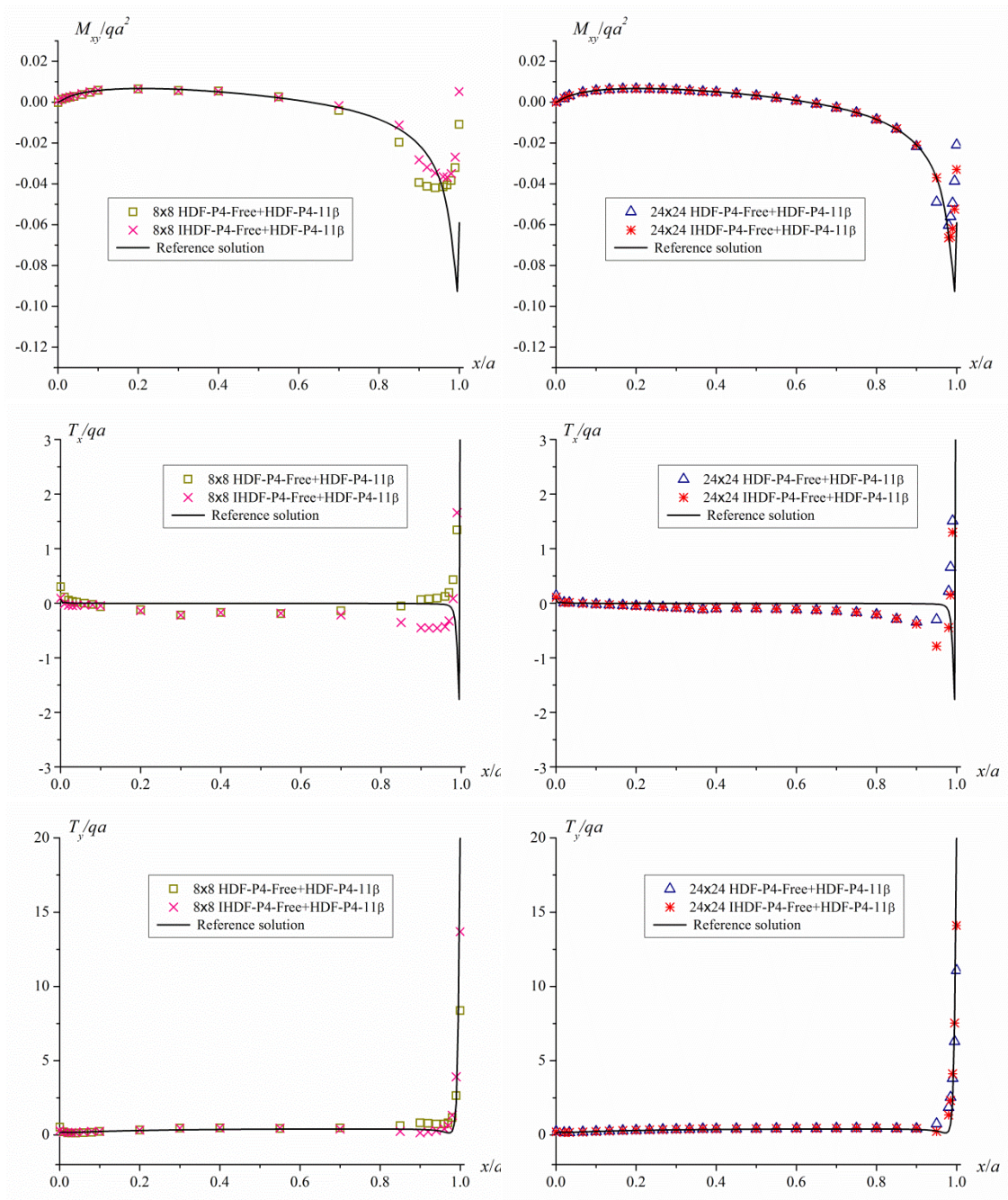
Figure 35. Distributions of twist moment M_{xy}, shear forces T_x and T_y along the path AB of the 60° skew plate in distorted mesh (SFSF case)
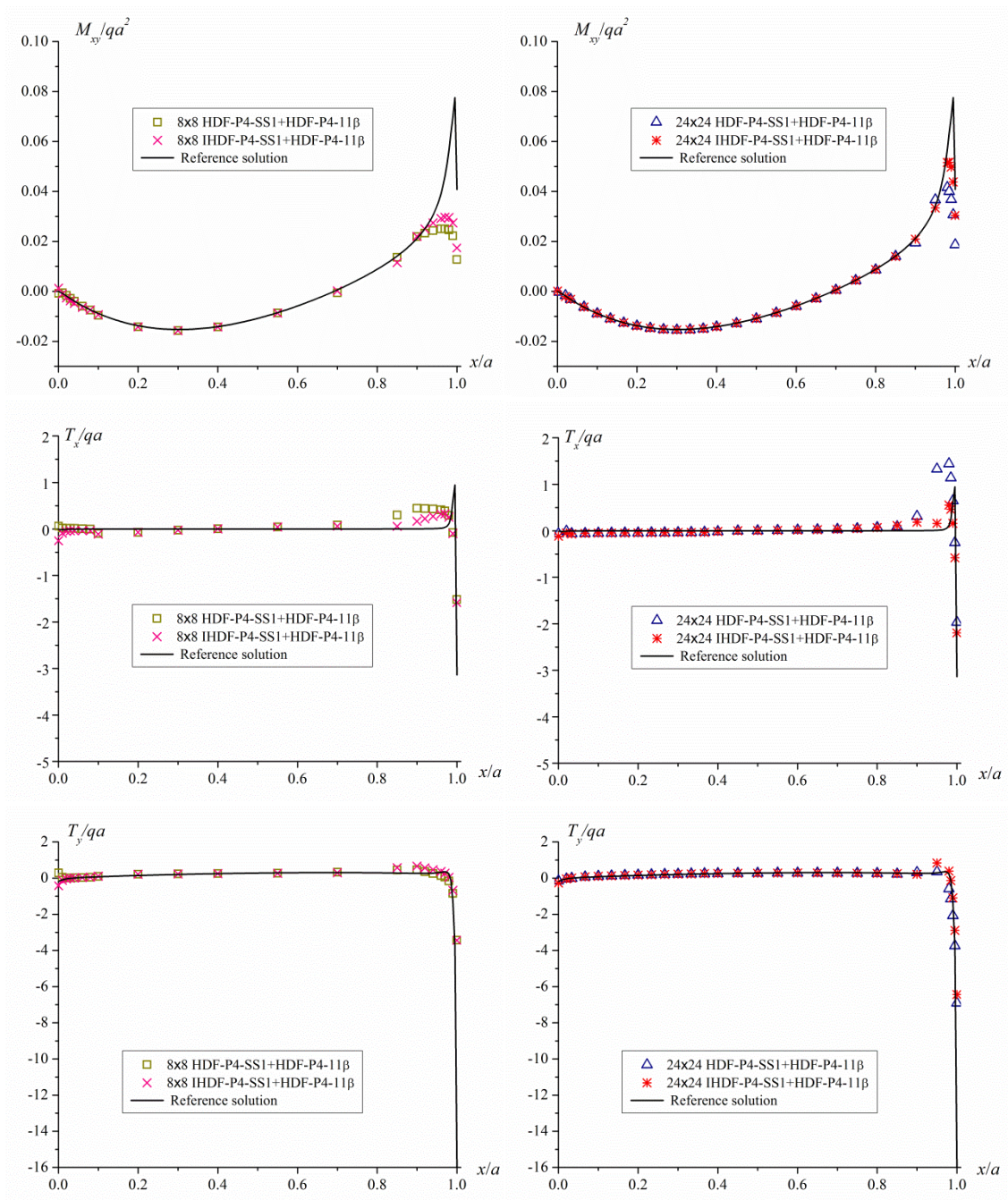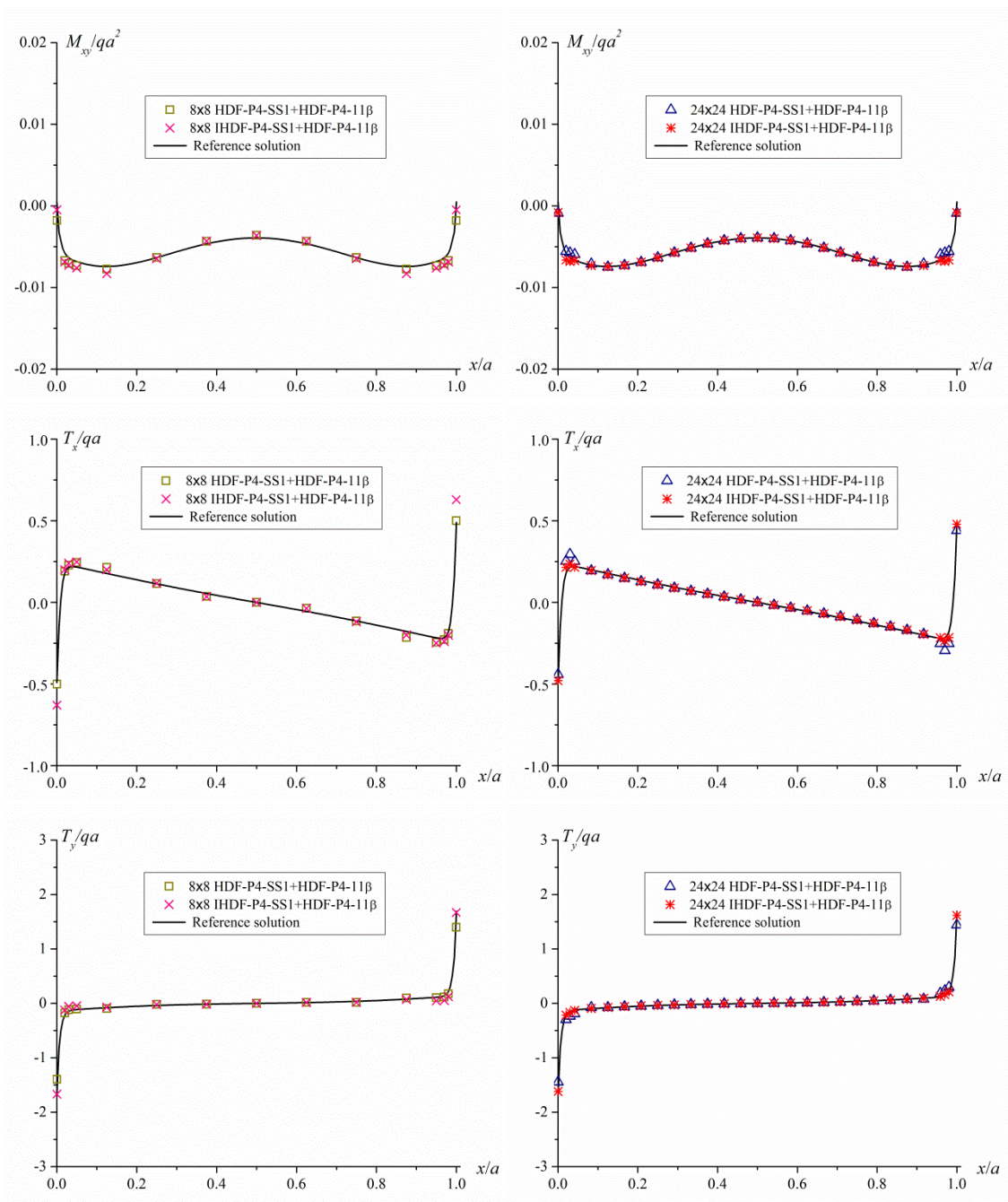
Figure 36. Distributions of twist moment M_{xy}, shear forces T_x and T_y along the path AB of the 60° skew plate in distorted mesh (SS*SS* case)
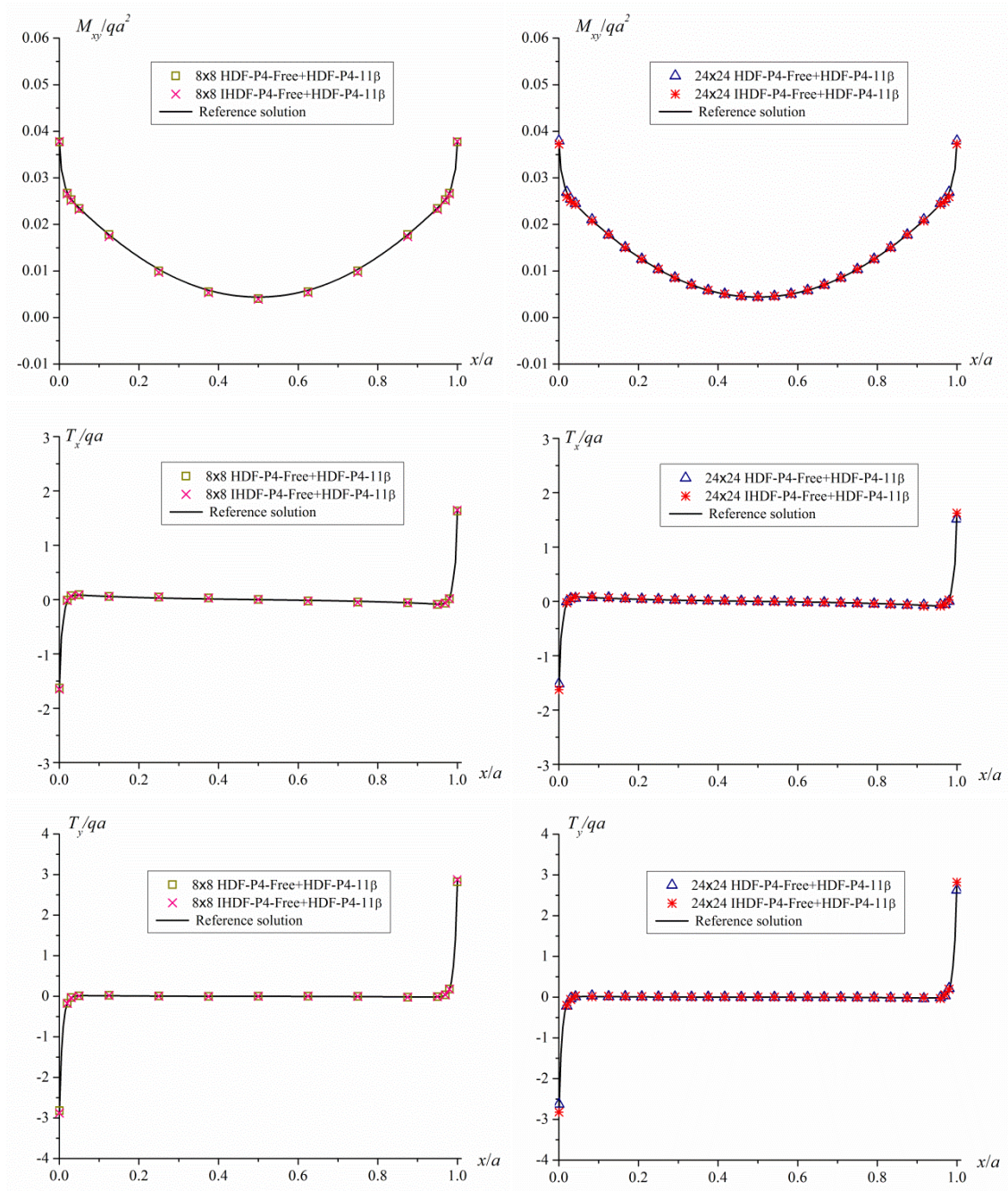
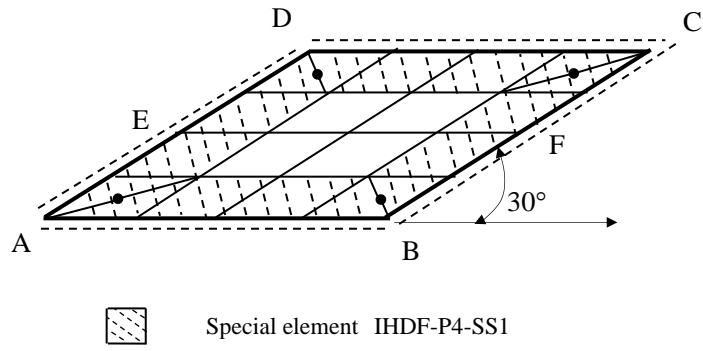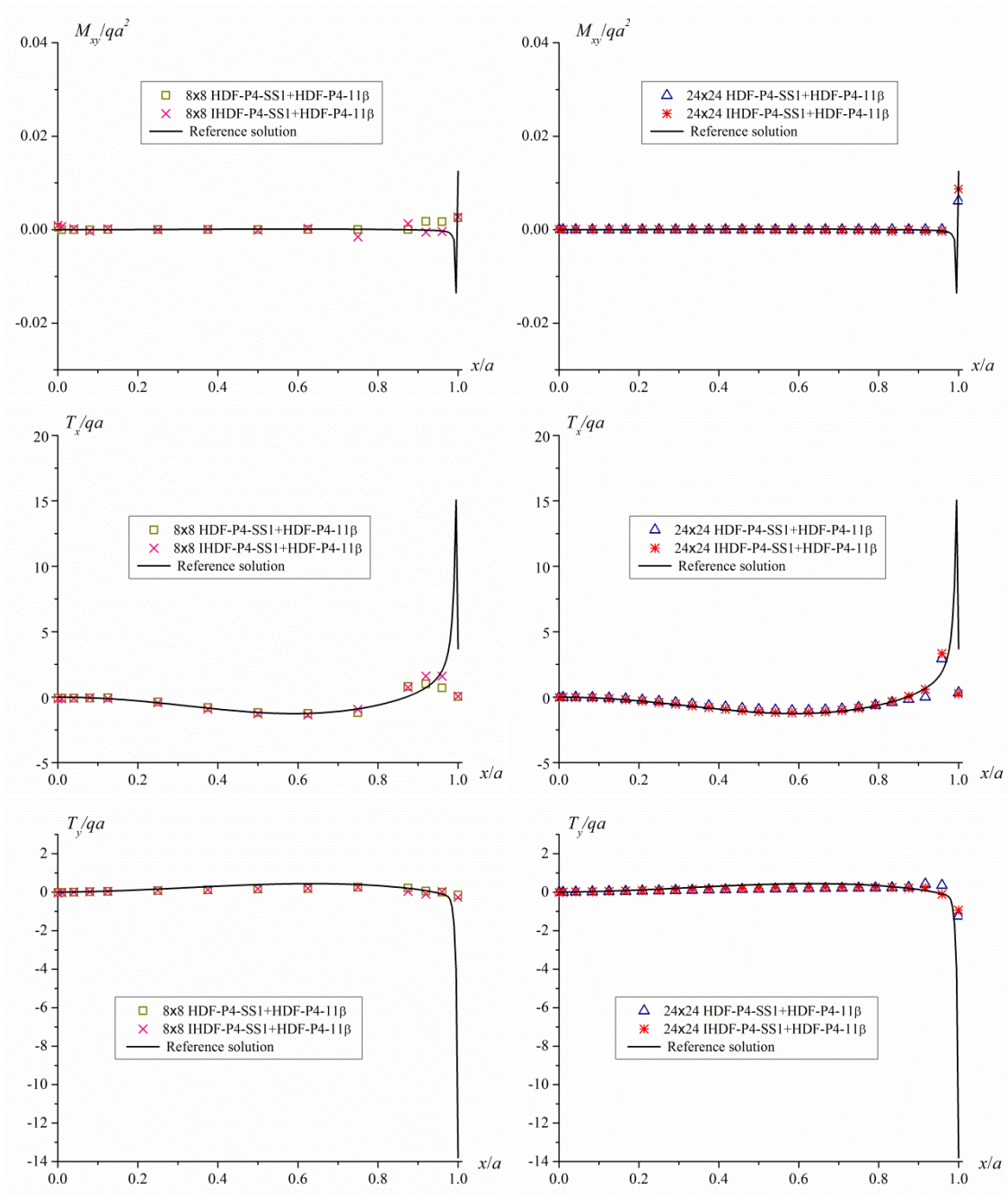Figure 37. Distributions of twist moment M_{xy}, shear forces T_x and T_y along the path EF of the 60° skew plate in regular mesh (SFSF case)
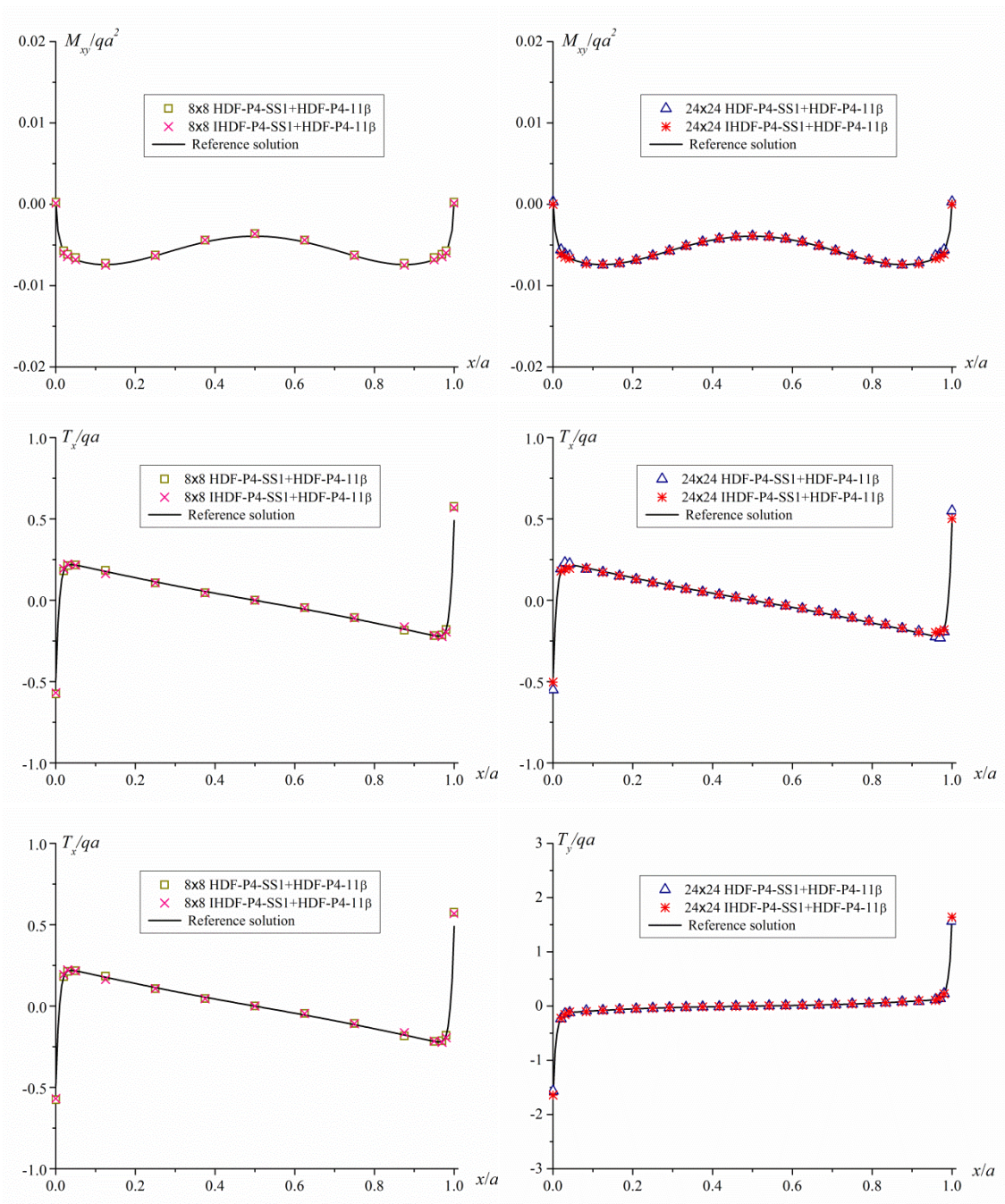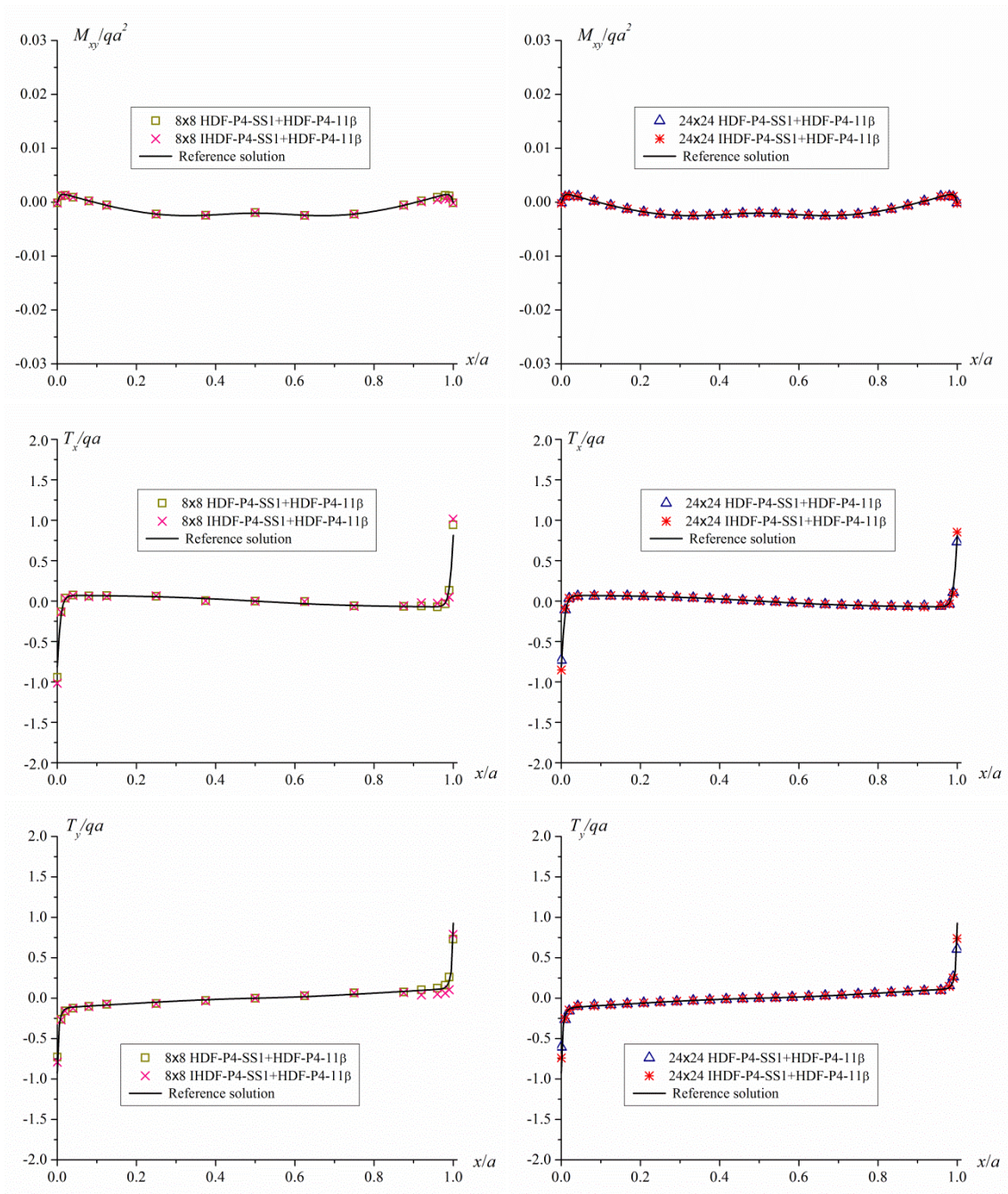
Figure 38. Distributions of twist moment M_{xy}, shear forces T_x and T_y along the path EF of the 60° skew plate in regular mesh (SS*SS* case)

Figure 39. Distributions of twist moment M_{xy}, shear forces T_x and T_y along the path EF of the 60° skew plate in distorted mesh (SFSF case)

Figure 40. Distributions of twist moment M_{xy}, shear forces T_x and T_y along the path EF of the 60° skew plate in distorted mesh (SS*SS* case)

Figure 41. The 30° skew plate with all edges soft simply-supported and the typical mesh

Figure 42. Distributions of twist moment M_{xy}, shear forces T_x and T_y along the path AB of the 30° skew plate

Figure 43. Distributions of twist moment M_{xy}, shear forces T_x and T_y along the path EF of the 30° skew plate
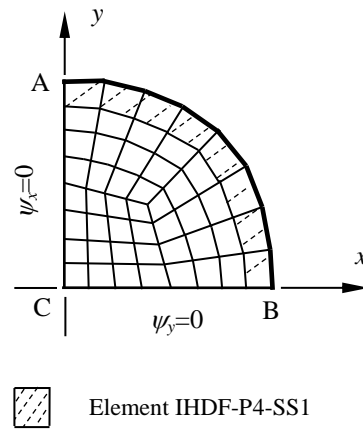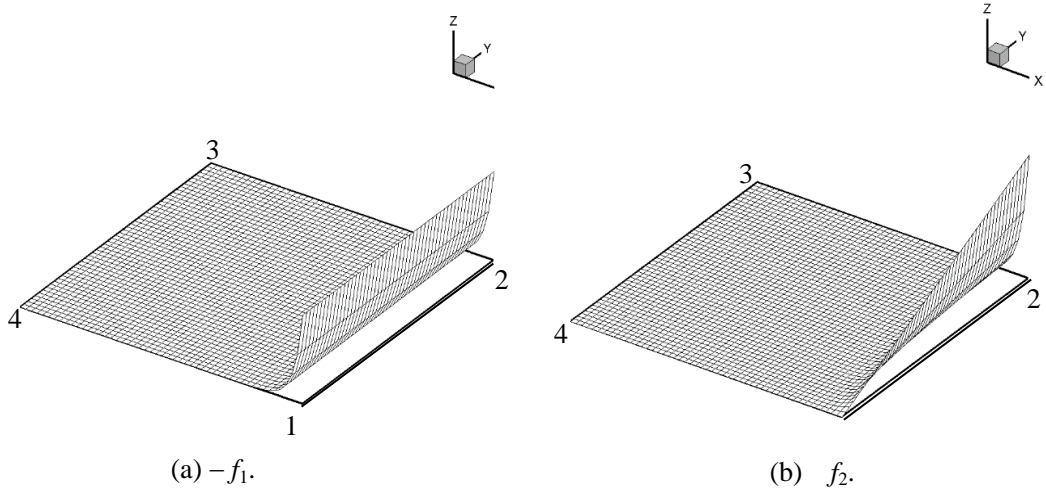
Figure 44. The circular plate with all edges soft simply-supported and the typical mesh

(a) $-f_1$.

(b) f_2.

The edge 12 is free/SS1 edge.
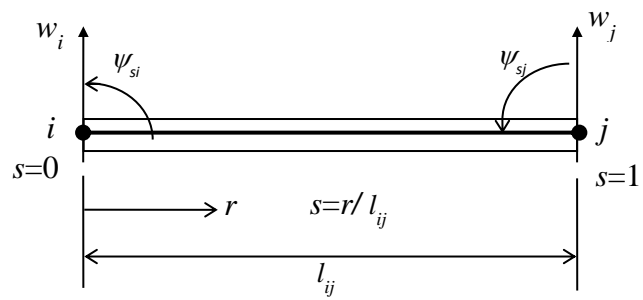
Figure A1. The distributions of f_1 and f_2 over a square domain

Figure B1. Timoshenko's beam element